CRYSTALLIZATION OF CALCIUM PHOSPHATE

ORIENTED BY SELF-ASSEMBLING DIBLOCK COPOLYMERS,

IN SOLUTION AND AT THE AIR-WATER INTERFACE

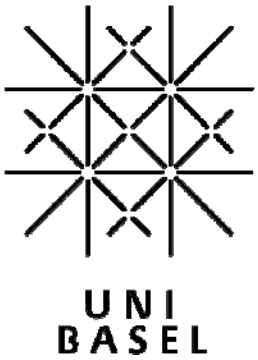

Inauguraldissertation

zur

Erlangung der Würde eines Doktors der Philosophie

vorgelegt der

Philosophisch-Naturwissenschaftlichen Fakultät

Der Universität Basel

Von

Olivier Casse

aus Frankreich,

Basel, 2011

creative commons

Attribution-Noncommercial-No Derivative Works 2.5 Switzerland

---

You are free:

to Share — to copy, distribute and transmit the work

Under the following conditions:

Attribution. You must attribute the work in the manner specified by the author or licensor (but not in any way that suggests that they endorse you or your use of the work).

Noncommercial. You may not use this work for commercial purposes.

No Derivative Works. You may not alter, transform, or build upon this work.

- For any reuse or distribution, you must make clear to others the license terms of this work. The best way to do this is with a link to this web page.
- Any of the above conditions can be waived if you get permission from the copyright holder.
- Nothing in this license impairs or restricts the author's moral rights.

Your fair dealing and other rights are in no way affected by the above.

This is a human-readable summary of the Legal Code (the full license) available in German:
http://creativecommons.org/licenses/by-nc-nd/2.5/ch/legalcode.de

Disclaimer:
The Commons Deed is not a license. It is simply a handy reference for understanding the Legal Code (the full license) — it is a human-readable expression of some of its key terms. Think of it as the user-friendly interface to the Legal Code beneath. This Deed itself has no legal value, and its contents do not appear in the actual license. Creative Commons is not a law firm and does not provide legal services. Distributing of, displaying of, or linking to this Commons Deed does not create an attorney-client relationship.

Quelle: http://creativecommons.org/licenses/by-nc-nd/2.5/ch/deed.en Datum: 3.4.2009

Genehmigt von der Philosophisch-Naturwissenschaftlichen Fakultät auf Antrag von
Prof. Wolfgang Meier,
Dr. Daniel Häussinger

Basel, den 28sten April 2009,

Prof. E. Parlow

Table of contents

I. Summary

Living organisms produce crystalline structures called biogenic crystals or biominerals, of various shapes and properties. Among them, mechanical properties, such as resistance to stress or elasticity, are often far from those of the corresponding species typically crystallized in the laboratory. For example, the fabrication of bones and teeth (calcium phosphate), shells (calcium carbonate), as well as the dissolution of unwanted materials such as kidney stones (calcium oxalate), essentially involves proteins that induce or inhibit nucleation, or favor the growth of crystals following a particular orientation. Compounds affecting crystal growth are gathered under the term "crystallization additives".

Calcium phosphate (CaP) is the main component of mammal bone. The demand for long-lasting, high-quality bone implants makes it interesting to quantitatively understand CaP nucleation, growth and degradation at various interfaces. A tremendous amount of work has already been dedicated to the controlled fabrication of CaP from aqueous and organic solution. Commercially available bone cements are typically viscous mixtures of CaP and water enabling a rapid solidification upon injection into a fracture. It appears that composition control is critical, since subtle differences may profoundly affect the cement behavior in vivo.

We therefore chose to focus on this particular material and test its interactions with synthetic polymers, presenting different template structures and chemical groups to the CaP, thus enabling us to study in a systematic way (pH, concentration, maturation time), interactions pathways that were different in nature or strength, as well as occurring at different steps during the course of the crystallization (nucleation, growth, maturation).

The synthetic polymers were chosen among the diblock copolymers family, because this allowed an interesting tandem where one block is responsible for interacting with the crystals while the other block determines the secondary structure of the polymer phase, its aggregation and possibly the shape of the resulting mineral at the micrometer scale.

This work presents three studies of CaP crystallization control by polymeric additives, under controlled conditions, in aqueous solution or at the air-water interface. In the perspective of medical applications, all chosen blocks are to some extent biocompatible, except the hydrophobic block holding the third polymer at the air-water interface. Three polymers were chosen in order to reflect the diversity of the interaction pathways:

1) poly(ethylene oxide)-*block*-poly(2-methyl-2-oxazoline), a neutral dihydrophilic block copolymer, in solution. We present the first characterization of well-defined self-assembly in presence of a mere difference in hydrophilicity as aggregation driving force instead of hydrophobic

interactions. As far as the mineralization of CaP is concerned, no significant influence was detected and this work may serve as a control study for the polybasic copolymer that has poly(ethylene oxide)-*block*-poly(2-methyl-2-oxazoline) as synthetic precursor, poly(ethylene oxide)-*block*-poly(ethylene imine). The self-assembly study grew well beyond the PhD, implying a wider range of techniques, and is now soon to be published.

2) polyethylene oxide-*block*-polyvalerolactone, a neutral amphiphilic block copolymer, in solution. Here, the PEO block is combined to a biodegradable, rather crystalline, hydrophobic block, at different degrees of polymerization. Despite having no particular affinity to CaP, PVL and its copolymers with PEO have found some interest as nanocontainers for drug delivery. However, again no significant influence was detected. This study suffered from the polymer high crystallinity. In later studies this problem was addressed by preferring the polycaprolatone variant.

3) poly(n-butylacrylate)–*block*–poly(acrylic acid), a charged amphiphilic block copolymer, at the air-water interface. Previously studied in solution, the polymer offers several tuning possibilities and the acrylic acid function is known to interact strongly with CaP. This approach was to our knowledge the first study on CaP mineralization of polymeric Langmuir films. We found that various conditions may be easily simulated in terms of charge surface density, supersaturation or pH, and result in various outcomes ranging from quick nucleation and growth without hierarchy to slow formation of nearly crystalline hexagonal array of uniform particles with identical particle sizes even at very long range (over 30 µm).

The outcome of this study is interesting because it demonstrates that even a rather flexible matrix like our polymer film at the air-water interface leads to uniform particles. Moreover, the film also acts as a tool for the 2D arrangement of the resulting particles in a near-crystalline order. The implication for biomineralization is that even rather flexible scaffolds swollen with water are able to regulate mineralization on the atomic (crystal phase), the nanoscopic (particle size and shape) and the sub-micron to micron scale (2D arrangement) of the precipitate. As a result, the current work could serve as a model for biological mineralization, which is more closely related to nature than films made from e.g. detergents or other low molecular mass compounds.

II. List of abbreviations

[η]	Intrinsic viscosity
2D-NMR	Two-dimension nuclear magnetic resonance spectroscopy
A_2	Second virial coefficient
ABC	Amphiphilic block copolymer
aq.	Aqueous, hydrated
AUC	Analytical ultracentrifugation
cac	Critical aggregation concentration
CaP	Calcium phosphate
cryo-TEM	Cryo-transmission electron microscopy
DHBC	Double-hydrophilic block copolymer
DLS	Dynamic light scattering
DOSY	Diffusion-Ordered SpectroscopY
LS	Light scattering
M_W	Weight-average molecular weight
NMR	Nuclear Magnetic Resonance spectroscopy
NOESY	Nuclear Overhauser Enhancement SpectroscopY
PAA	Poly(acrylic acid)
PEI	Poly(ethylene imine)
PEO	Poly(ethylene oxide)
PEO-PEI	Poly(ethylene oxide)-*block*-poly(ethylene imine)
PEO-PMOXA	Poly(ethylene oxide)-*block*-poly(2-methyl-2-oxazoline)
PEO-PVL	Poly(ethylene oxide)-*block*-poly(valerolactone)
PMOXA	Poly(2-methyl-2-oxazoline)
PnBuA	Poly(n-butylacrylate)
PnBuA-PAA	Poly(n-butylacrylate)–*block*–poly(acrylic acid)
PVL	Poly(valerolactone)
R_G	Radius of gyration
R_H	Hydrodynamic radius
SAXS	Small angle X-ray scattering

SEM	Scanning electron microscopy
SLS	Static light scattering
TEM	Transmission electron microscopy
T_G	Glass transition
XRD	X-ray diffraction
ρ	Sphericity factor R_G/R_H
cc	Concentrated solution

III. Introduction

A. Proteins and homopolymeric crystallization additives

Living organisms produce crystalline structures called biogenic crystals, of various shapes and properties (Figure 1). Among them, the mechanical properties, such as resistance to stress or elasticity, are often far from those of the corresponding species typically crystallized in the laboratory.[1,2] For example, the fabrication of bones and teeth (calcium phosphate), shells (calcium carbonate), as well as the dissolution of unwanted materials such as kidney stones (calcium oxalate), essentially involves proteins that induce or inhibit nucleation, or favor the growth of crystals following a particular orientation (Scheme 1). Compounds affecting crystal growth are gathered under the term "crystallization additives".

A protein adsorbing on a crystal uses a lattice match between one of the crystal surfaces and the ternary structure of its amino-acids sequence. For example, statherin, an acidic protein found in saliva, adsorbs on the surface of teeth, which is made of hydroxyapatite (HAp), the most stable form of CaP in biological conditions. In so doing, the statherin inhibits further crystal growth[3] (Scheme 1). Statherin also binds to free HAp crystals that are found supersaturated in saliva. It is postulated that some of its acidic amino acids form a chelate complex with calcium ions on the HAp surface. Other macromolecular compounds may also control crystallization, and that effect is not limited to biological materials. For example, polyelectrolytes affect the mechanism of crystallization: nucleation, crystal growth or relative growth rates, aggregation, and phase transformation, are directly controlled by the polymer and its concentration. Several effects can be observed here: crystal numbers, sizes and size distribution change, crystal habits are modified, polymer is incorporated in the precipitate, and finally, the crystal phase is also partly selected by the chemistry and presence of the polyelectrolyte. Studies suggest that some "epitaxial-like" interactions between the organic matrix or the additive and the growing crystal are responsible for the observed results.[4,5] This is certainly conceivable, but later studies[6] have also shown that other effects like thermodynamic considerations or charge effects, among others, play a role in mineralization control as well. Understanding and predicting these interactions and effects with *in silico* models is the key to new organic / inorganic hybrid materials with controlled chemical, mechanical or surface properties.

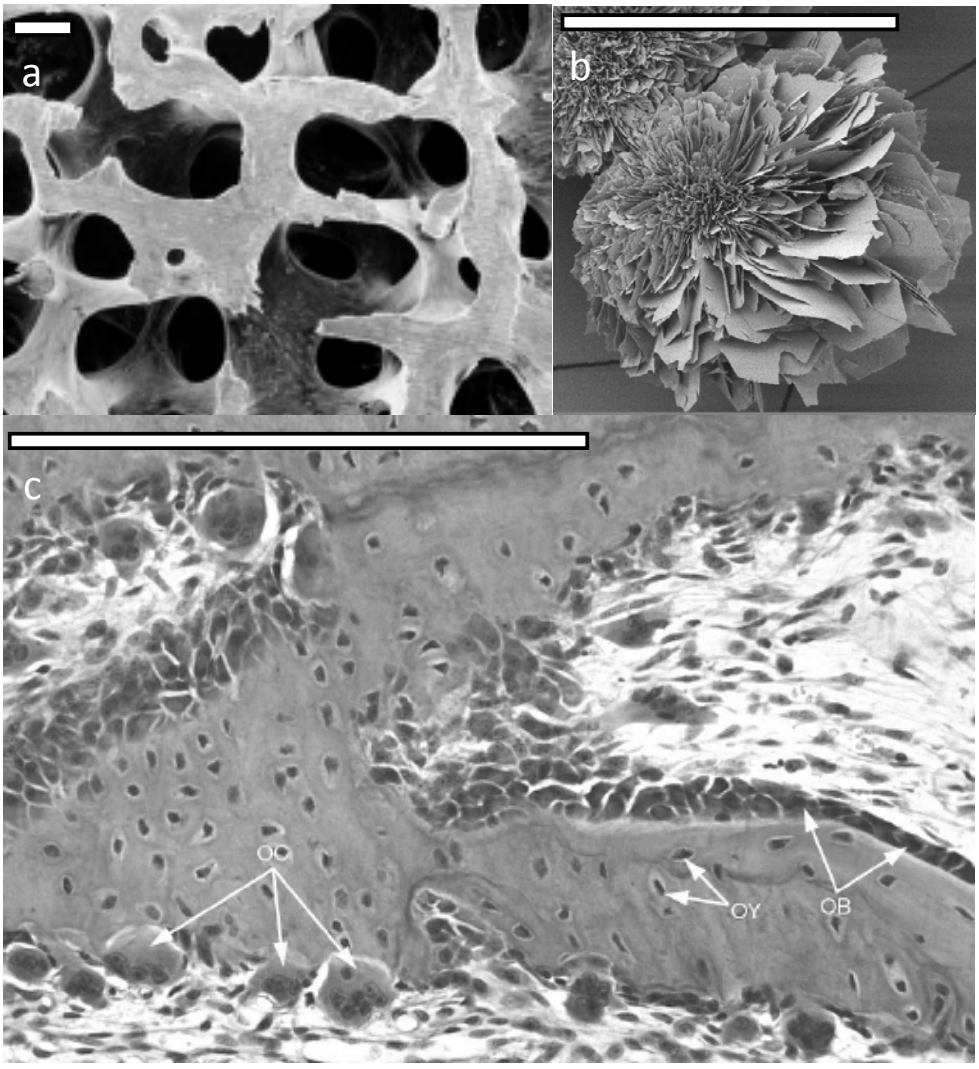

Figure 1. In vitro crystallization and biomineralization of CaP. a) Scanning electron micrograph of a lumbar vertebra after removal of bone cells and soft tissues; b) Optical micrograph of a section of remodeling bone, showing: osteoblasts (OB) forming bone, osteocytes (OY) in bone matrix, osteoclasts (OC) forming resorption pits in the bone surface; c) Scanning electron micrograph, in-vitro crystal habit of octa-calcium phosphate. Scale-bars: 250 µm.[8]

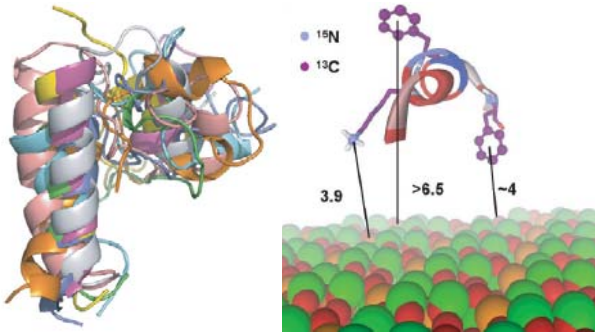

Scheme 1. Model reconstruction of the adsorption of the statherin protein to a CaP surface. The acidic fragment adopts a helical conformation upon binding to HAp.[9]

Calcium phosphate (CaP) is one of the most important biominerals. It is, among others, the main component of mammal bone.[7,8] The ever-growing demand for long-lasting, high-quality implants makes it interesting to quantitatively understand CaP nucleation, growth and degradation at various interfaces. Indeed, a tremendous amount of work has been dedicated to the controlled fabrication of CaP from aqueous and organic solution.[10] Commercially available bone cements are typically viscous mixtures of CaP and water enabling a rapid solidification upon injection into a fracture. Composition control is critical since subtle differences may profoundly affect the cement behavior in vivo.[11,12] We therefore chose to focus on this particular material and test new polymers in a systematic way (pH, concentration, maturation time).

Since additives may interact at any stage of the crystallization, it is necessary to detail the process and infer how each step of it may be altered. A crystal is a compact structure of atoms or molecules characterized by its short-range order (periodicity in three dimensions at the scale of the atoms or molecules). Crystallization typically proceeds in three consecutive stages: nucleation, growth and maturation. During the nucleation step, hydrated (or solvated) ions must assemble into a stable germ by overcoming the surface energy barrier. In order to gain stability, a germ must grow over the critical size below which the energy required to desolvate the ions (proportional to the created surface) remains larger than the energy released through ion binding (stabilization energy, proportional to the created volume). During the growth step, new ions are added in a periodical way, filling the thermodynamically unstable sites first. Consequently the faces bearing the most unstable sites statistically grow faster and disappear, which determines the final morphology of the crystal. During the maturation step, crystals of different sizes exchange material through collisions (Ostwald ripening). The larger crystals, which are the more thermodynamically stable due to their smaller surface energy per volume ratio, will keep growing using material from smaller ones. Maturation towards a more stable crystal phase is possible.

All these steps can potentially be influenced by the physical conditions or the environment: temperature and often pH, ionic strength, but also possibly crystallization additives. By creating solution structures, additives may act as steric templates, leaving their imprint in the mature inorganic material. However, specific interactions offer a wider range of possibilities:

- Nucleation control: Additives able to complex one of the counter-ions in solution may retard or inhibit nucleation, if the complex is too stable, retarding nucleation and favoring large crystals over a large number of smaller ones. Altered relative concentrations of free (solvated) counter-ions may also lead to a different crystalline phase. Additives with multiple complexation sites may help seed formation (heterogeneous nucleation), either by increasing the local concentration of counter-ions (similarly to heterogeneous nucleation, in the course of which ions adsorb on surfaces), or by stabilizing smaller germs via the reduction of energy barrier necessary

to reach the seed critical size (similarly to dust favoring the condensation of water in the atmosphere). Such a mechanism increases the number of germs while leaving the growth kinetics unaffected, thus reducing the overall crystal size.

- Growth and maturation control: Additives able to adsorb selectively on surfaces may modify the final crystal morphology. Such additives may influence the relative availability of the growth sites, thus altering the final morphology (either a different axis final ratio or a completely different morphology), or even freeze a crystal face, kinetically speaking, by inhibiting growth. Ostwald ripening may even be prevented, as small crystals may also be kinetically frozen by a protective layer of adsorbed additive.
- In combination, an additive able to both adsorb specifically on crystal faces and to complex ions may build-up a relatively high ion supersaturation in the vicinity of the face. This is noticeable because it may result not in a freezing of the face which it is adsorbing onto, but in the opposite result, a faster growth rate.

Finally, all additives may be removed after mineralization i.e. by calcination, leaving their negative imprint in the mature inorganic material.

B. Diblock copolymers: self-assembly, properties and applications

In a separate field of research, block copolymers have attracted a tremendous attention due to their wide range of applications. In particular, amphiphilic block copolymers (ABCs) have found applications in the cosmetics, food, medical and waste water treatment industries, to just name a few examples.[13,14]ABCs self-assemble in aqueous solution in order to minimize interactions between the hydrophobic block and water, and yield well-organized aggregates[15,16]which in some cases include bio-functionalities or bio-inspired responsive blocks.[17,21] ABCs containing a (stimuli-responsive) polyelectrolyte block as the hydrophilic part are of particular interest to the scientific and industrial community. This is due to the fact that pH, ionic strength or temperature allow for a tuning of the response of the respective aggregates towards these stimuli.[16,22-24] This will, for example, allow fabricating robust and simple formulations for the food and cosmetics industries.

Beside their behavior in bulk solution, ABCs have been studied at the air–water interface.[25-28] Similarly to small amphiphiles such as lipids, ABCs tend to stay at the water surface (Langmuir film). This offers the possibility to easily replace the air-water interface with a new tunable interface (the hydrophilic block) in order to study, for example, its interaction with species in solution or to deposit it onto a solid substrate (Langmuir-Blodgett transfer). Semi-crystalline hydrophobic blocks will limit or prevent such film formations. When they can form however, polymer monolayers are

characterized by less sharp phase transitions in 2D than films of low molecular weight amphiphiles. This is the result of their large degree of conformational freedom and of a stronger cohesion between the considerably larger chains. This is an advantage, since this means that ABCs tend to form more stable and reversibly compressible monolayers with large lateral compressibilities.[29]

However, a hydrophilic / hydrophobic balanced structure is not necessary for interesting properties to arise. A particular class of water-soluble molecules, so-called double-hydrophilic block copolymers (DHBCs), has also attracted attention. In this case, to a functional hydrophilic block chosen for its chemical properties, another hydrophilic block is covalently attached, except that this one has the sole function of keeping the first block active in solution by ensuring solubility. For that reason, it is usually much longer than the active block. Polyethylene oxide (PEO) is often chosen as the provider of solubility, since it is not only very water-soluble and commercially available, but also absolutely non toxic. For example, it will prevent a polyelectrolyte block from coacervating in high ionic strength conditions. Additionally, the fact that DHBCs are easily removed via washing and centrifugation or via Soxhlet extraction with water might constitute an advantage over amphiphilic copolymers in an industrial process.

C. Crystallization in the presence of self-assembling polymeric additives: a combination for new hybrid organic / inorganic materials

Considering these facts, it seems promising to search for combinations of the two phenomena: diblock copolymers with special abilities as crystallization additives. ABCs do act as growth- and structure-directing additives, and the chemistry, structure, and architecture of the polymer have a dramatic influence on the outcome of the growth of crystals. Indeed, they were used to engineer the size, shape, crystal phase and 1D, 2D and 3D organization of inorganic particles.[30-41] A number of studies with homopolymers have been published.[48,49,51,52,54,57,59,70-78] DHBCs were also studied for their role in (biomimetic) mineralization control of inorganic compounds. They were proved to be efficient growth modifiers for ZnO,[42-45] calcium carbonate[46] as well as calcium phosphate, [30,37,46-69] especially poly(ethylene oxide)-based block copolymers where the second block is a polycarboxylate such as poly(methacrylic acid), poly(acrylic acid), poly(glutamic acid) or poly(aspartic acid). For example, Antonietti, Cölfen, Mann *et al.* demonstrated that poly(ethylene oxide)-block-poly(methacrylic acid)-$C_{12}H_{25}$ forms interactive template micelles thanks to a stabilized corona of charges. However, the vast majority of the published studies focused on the low concentration regime of the polymeric additive, with typical polymer concentrations ranging from a few ppm to approximately 1 g/L.[1] Interestingly, despite being one of the most interesting inorganic

materials in biology, CaP is only now being increasingly studied in the high additive concentration range.

D. The air-water interface approach to biomineralization

Other approaches towards advanced CaP/organic hybrid materials include the mineralization of insoluble scaffolds or the mineralization in hydrogels. Hydrogels and polymer matrix systems were extensively studied by several groups.[79-98] Insoluble scaffolds have also been considered, especially polyester matrices for bone substitutes and other applications.[99,100]

Interestingly, there have been very few studies on the mineralization of block copolymer films at the air–water interface. For example, Xinran *et al.* studied the cooperative regulation of the crystallization of calcium carbonate by a polypeptide and a DHBC beneath the water surface. This is intriguing because there have been a series of studies on the mineralization of low molecular mass compounds and other small molecules with a variety of inorganic materials,[102,109] yet few studies on CaP growth on solid films [53,61,110,111] or in polymer vesicles, or concentrated polymer solution[112] Only the effect of dissolved poly(acrylic acid) on the mineralization of $CaCO_3$ under a Langmuir film and CaP formation under surfactant films have been studied. Furthermore, lipid-like peptide monolayer films have been shown to be strong growth modifiers for calcium carbonate. As a result, it is known that the crystallization of inorganic materials can in many cases be readily controlled by the chemistry and / or the charge of the monolayer. However, reservations remain about the analogy between surfactant monolayers and biological systems, which are often claimed to be an inspiration for monolayer mineralization experiments. For example, biological mineralization scaffolds are polymeric in nature and rarely crystalline, in contrary to many surfactant monolayers. In contrast to what is observed with crystalline monolayers of low molecular mass surfactants, biomineralization is controlled to quite some extent by the interaction of a polymeric, organized yet not rigid, substrate with a growing inorganic species.[2,113-115] This suggests that well-organized but flexible and soft polymeric substrates or interfaces could be prime candidates for studies of both technologically important mineralization processes and biomineralization. It therefore seems straightforward to transfer the concept of Langmuir film mineralization from low molecular mass surfactants to polymeric films.

E. Aim of the work and chosen systems

This work presents three studies of CaP crystallization control by polymeric additives, under controlled conditions (pH, maturation time, in aqueous solution or at the air-water interface). Three polymers were chosen in order to reflect the diversity of the interaction pathways: a neutral DHBC in solution, a neutral ABC self-assembling in solution, and a charged ABC at the air-water interface. In the perspective of medical applications, all chosen blocks are to some extent biocompatible, except the hydrophobic block holding the ABC at the air-water interface.

First, the neutral DHBC in solution is poly(ethylene oxide)-*block*-poly(2-methyl-2-oxazoline) (PEO-PMOXA). Generally, it is necessary to understand the underlying structure formation principles of the pure polymers before studying their effects on nucleation and growth of inorganic crystals. In this particular case, a thorough characterization of the pure PEO-PMOXA in aqueous solution yields results about the self-assembling properties of neutral DHBCs that interestingly complement work previously achieved in our group.[112] We have earlier shown that PEO-PMOXA forms unique water-in-water (W/W) mesophases at high concentration in aqueous salt solution, and that these W/W mesophases seem to template porous CaP. However, to our knowledge, double-hydrophilic block copolymers were not reported to self-assemble in the 'intermediate' concentration range of 1 to 60 g/L. For example, Thünemann and General have shown that poly(ethylene oxide)-*block*-poly(ethylene imine) (PEO-PEI) form well defined aggregates in aqueous solutions, but only if the PEI block complexes with a fatty acid. The fatty acids make the polymer amphiphilic, which leads to the observed behavior.[116] This thesis presents the first characterization of well-defined self-assembly even though the polymer is not modified with hydrophobic groups, with a mere difference in hydrophilicity as aggregation driving force instead of hydrophobic interactions. As far as the mineralization of CaP is concerned, this work may serve as a control study for the polybasic copolymer that has PEO-PMOXA as synthetic precursor, PEO-PEI(H^+).

Second, the neutral amphiphilic copolymer used here is polyethylene oxide-*block*-polyvalerolactone (PEO-PVL) because it is a promising candidate to integrate scaffolds for bone substitutes. Here, the PEO block is combined to a biodegradable, rather crystalline, hydrophobic block, at different degrees of polymerization. Despite having no particular affinity to CaP, PVL and its copolymers with PEO have found some interest for medical applications, in particular as nanocontainers for drug delivery.[117-125] It is interesting for these and related applications because of its slow degradation rate and high stiffness, yet good processability.

Finally, the polymer spread at the air-water interface is poly(n-butylacrylate)–*block*–poly(acrylic acid) (PnBuA-PAA), because it has already been studied in solution and offers several tuning possibilities (depositing the polymer as single chains or as micelles, modifying the relative

block lengths, or adjusting the protonation degree by pH). Colombani et al. have shown that PnBuA-PAA block copolymers spontaneously self-assemble into monodisperse spherical aggregates when dispersed in aqueous solution.[126-128] The presence of the PAA block enables the variation of the size of the aggregates by changing the salt concentration. However, no significant pH dependence was observed, which was explained by the fact that the aggregates are kinetically frozen (out of equilibrium) in spite of the very low glass transition of the PnBuA block (T_G = -55°C). This approach is to our knowledge the first study on CaP mineralization of polymeric Langmuir films.

IV.Results

A. Self-assembly and mineralization of poly(ethylene oxide)-*block*-poly(2-methyl-2-oxazoline)

PEO-PMOXA (Scheme 2) is a DHBC typically synthesized by cationic ring-opening polymerization of 2-methyl-2-oxazoline from a monomethoxy poly(ethylene oxide) macroinitiator.[129]

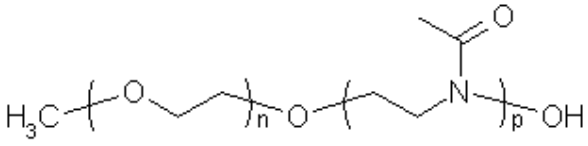

Scheme 2. Chemical formula of PEO-PMOXA.

The fabrication of the first lyotropic mesophase separation without hydrophobic domains and the formation of CaP with a new and potentially useful morphology were already studied at high concentration (more than 50% w/w).[112] We now extend the concentration range below the mesophase domain, down to the intermediate range of 1 to 60 g/L. The system is qualitatively different dynamically speaking and a large number a new techniques were summoned. First, we present evidence of polymer aggregation despite the absence of hydrophobic interactions, and suggest a model for this self-assembling. Second, we study the formation of DHBC-CaP hybrid particles.

1. Self-assembly in aqueous solution

Figure 2,Figure 3 and Figure 4 show representative dynamic and static light scattering of PEO_{113}-$PMOXA_{60}$ in water.

DLS autocorrelation functions fitted by regularized inverse Laplace transform (CONTIN algorithm, Figure 2) reveal two distinct decay times, which differ by two orders of magnitude. After more accurate fitting by non-linear lag-time analysis (Figure 3),[130] the respective diffusion coefficients D_1 and D_2 were calculated by extrapolation to zero momentum transfer and zero concentration, then converted to hydrodynamic radii (R_H) (Annex: Equation 9, Equation 10). As a result, the population at high diffusion coefficients {$D_1 = (9.1 \pm 1.2)\cdot10^{-11}$ m²/s, $R_{H,1} = 2.4 \pm 1.4$ nm} is relatively monodisperse and have sizes that are characteristic for very small aggregates or single polymer chains. The large relative error on D_1 is due to the small relative intensity scattered by this population (approximately 10%). The population at low diffusion coefficients {$D_2 = (2.1 \pm 0.7)\cdot10^{-12}$ m²/s, $R_{H,2} = 100 \pm 30$ nm} corresponds to larger aggregates. In this case the large relative error on D_2 is due to the large

dispersity of the aggregates. Additionally, these larger features are dominant in intensity (approximately 90%), which indicates that SLS measurements will characterize them with a maximum error of 10% due to the background noise from the smaller population.

SLS (Figure 4) also indicates the presence of large aggregates in aqueous solution with an average radius of gyration R_G of 72 ± 2 nm, using the random coil model.[130-133] The second virial coefficient (A_2) is zero within the experimental error (-0.5 ± 3)·10^{-6} mol·cm^3/g^2 (typical significant values range from ± 10^{-5} to ± 10^{-3} mol·cm^3/g^2 ; for a PEO homopolymer of 10000 g/mol at 25°C,[134] A_2 was measured at 6·10^{-3} mol·cm^3/g^2). This indicates that the particle-solvent and particle-particle interactions are comparable, which is important because it means that the observed particles have a stable structure within the studied concentration range (for example, no loss of aggregate material to the solvent upon dilution). The apparent weight-average molecular weight of the aggregates is M_w^{app} = (260 ± 10)·10^3 g/mol. Using the weight-average molecular weight of the block copolymer of 10.1 kg/mol, the average aggregate is found to consist of only about 25 ± 1 polymer chains, which is surprising because far too small to be physically relevant. Even very water-swollen aggregates with a polymer density of 0.01 with an R_G of 70 nm should have a mass exceeding 10^9 g/mol. Multiple measurements and calibrations have yielded the same low order of magnitude for M_W. Since further experiments give evidence for the weakness of the forces driving the aggregation (see DOSY, viscosimetry), it might be that the heating of the solution by the laser partially disrupts the aggregates. More probably, the low contrast between polymer and water (refractive index increment dn/dC = 0.16 mL/g) makes the evaluation difficult. As far as the molar mass is concerned, we can only conclude that the particle density is very close to that of water. However, the calculation of the radius is not affected by the molar mass in the Zimm plot, because the radius is a part of the form factor, and is thus calculated as a relative factor (see Annex, Equation 18). Finally, the scattered intensity at concentrations approaching 1 g/L reaches the solvent level. This suggests that there is a phase transition, but it cannot be measured at this point.

Combining the radii from DLS and SLS yields a ratio $\rho = R_G/R_H$ of roughly 0.7. A ρ factor of 1 would be characteristic for vesicular structures and 0.78 for compact spheres.[130] Hence, light scattering data indicate the presence of spherical aggregates in solution.

As a control experiment, we measured SLS of pure PEO homopolymers (M_w = 5000 g/mol, Figure 5). PEO does show some aggregation above 30 g/L (R_G = 80 nm), despite the even lower contrast factor. However, the second virial coefficient is three orders of magnitude higher than that of the DHBC (A_2 = 3·10^{-3} mol·cm^3/g^2), which significantly illustrates the high water solubility of PEO aggregates compared to the PEO-PMOXA aggregates. Moreover, the scattered intensity reaches the solvent level already below 20 to 30 g/L. This is visible on the Zimm plot via the wide and random

scattering of the points in the two low-concentration series. Comparatively, PEO-PMOXA maintains a stable (A_2 = 0) aggregation down to concentrations 10 times lower.

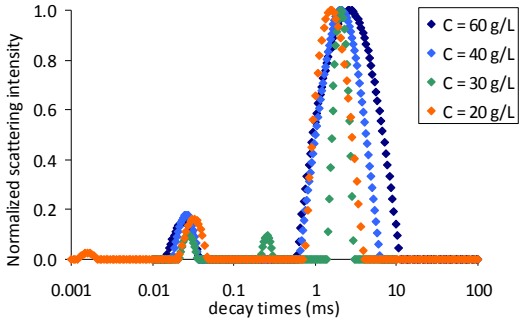

Figure 2. DLS (regularized inverse Laplace transform, CONTIN algorithm) of PEO_{113}-b-$PMOXA_{60}$ in aqueous solution. Qualitative distribution of Brownian motions decay times

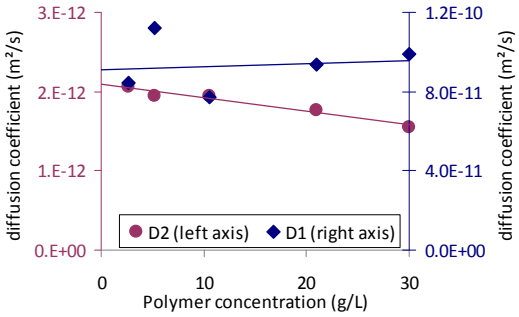

Figure 3. DLS (non-linear lag-time analysis) of PEO_{113}-b-$PMOXA_{60}$ in aqueous solution. Average diffusion coefficients of the two populations.

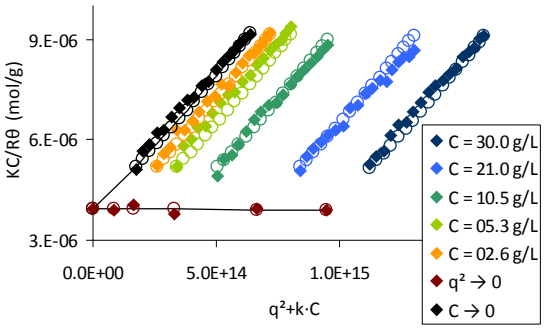

Figure 4. Zimm plot (SLS) of PEO_{113}-b-$PMOXA_{60}$ in aqueous solution ($k = 10^{13.5}$, circles are simulated data).

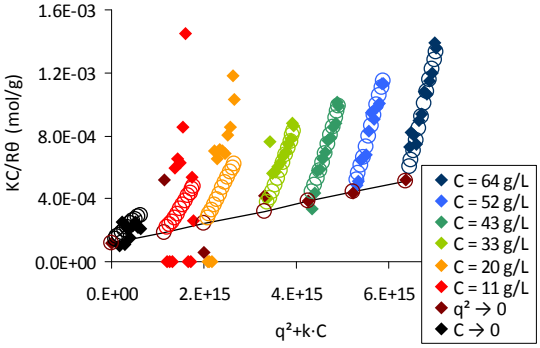

Figure 5. Zimm plot of PEO_{113} ($k = 10^{14}$).

TEM performed on dried samples further confirms the presence of roughly spherical aggregates. Figure 6 shows representative TEM micrographs of PEO_{113}-$PMOXA_{118}$ aggregates after negative staining, therefore polymer-rich regions will appear in white. Figure 6a reveals that the aggregates are roughly spherical in shape and have a size of ca. 50 to 200 nm. This is consistent with light scattering if some shrinking of the aggregates, due to the high vacuum conditions and the high water content in the aggregates, are taken into account. Figure 6b also shows that the aggregates are probably not very stable, as the negatively stained samples also show features in the background, mostly thin lines. These lines could be smaller polymer filaments responsible for the high diffusion coefficients in DLS, but a clear assignment was not possible. Furthermore, TEM occasionally also shows stripe patterns (Figure 6c-d), which were interpreted as arising from a (poorly ordered) layered mesophase, similar to the W/W mesophases postulated earlier for these polymers.[S89]

Interestingly, cryo-transmission electron microscopy (cryo-TEM) does not reveal the presence of structure, which is presumably due to a very low contrast between the aggregates and water. This suggests, in agreement with light scattering, that the structures have a density close to water. As a result, TEM and light scattering suggest that the particles are low-density water-swollen gel-like particles rather than regular core-shell micellar aggregates.

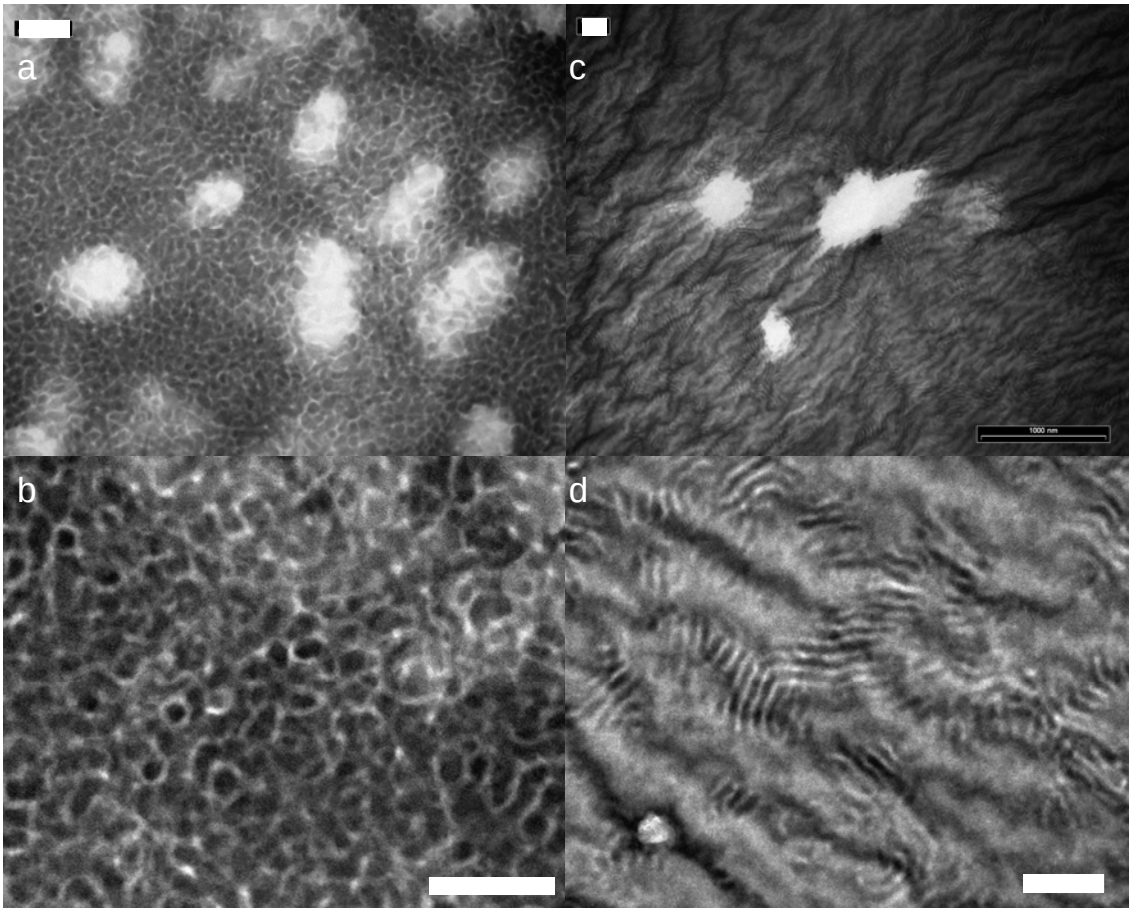

Figure 6. TEM micrograph (negative staining with uranyl acetate) of a dried PEO_{113}-$PMOXA_{118}$ 20 g/L solution. Scale-bars: 200 nm. (a) and (b): typical features; (c) and (d): occasional features. Scale-bars: 200 nm.

A SAXS pattern of a solution of 20g/L of PEO_{113}-$PMOXA_{118}$ (Figure 7) offers a reasonable match with rod-like entities with a length of 6.7 nm and a radius of 0.84 nm (this method is sensitive to the number average, therefore large aggregates are not visible). SAXS therefore suggests that besides the spherical overall shape of the aggregate, there is a further nanoscale structure within these aggregates in agreement with the filaments observed with TEM.

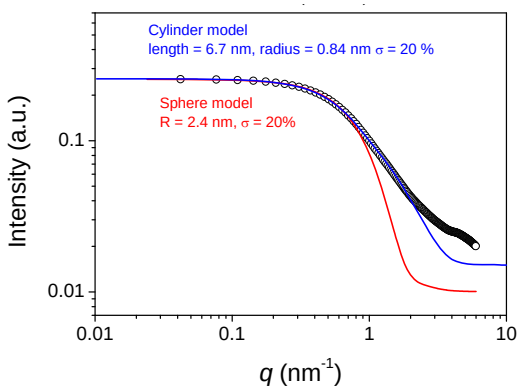

Figure 7. SAXS pattern of a 20 g/L solution of PEO_{113}-$PMOXA_{118}$.

Below concentrations of 1 g/L, signal levels are too low for LS or SAXS analysis. The transition to low concentration regime was therefore studied with AUC, surface tension measurements and viscosimetry.

Figure 8 represents the sedimentation coefficient distributions *c(s)* of aqueous solutions of PEO_{113}-$PMOXA_{118}$ at different concentrations. The sedimentation coefficient *s* is the ratio between the particle momentum (*mass x velocity*) and the buoyant force ($-m \cdot \omega^2 \cdot r$), and represents the effective molecular weight corrected for the effect of buoyancy. It is usually expressed in Svedberg (1 S = 10^{-13} s). The figure therefore shows that at concentrations above 10 g/L, AUC reveals broad sedimentation coefficient distributions of the samples and a shifting of the sedimentation coefficient (s_{max}) with concentration. This indicates the existence of aggregates. Below 5 g/L, the only detected species are individual polymer chains with a narrow distribution and a molar mass of M_w ~ 15 kg/mol. The critical aggregation concentration should therefore be in the range of 5 to 10 g/L. This is supported by surface tension measurements of PEO_{113}-$PMOXA_{118}$ (Figure 9). Three independent series of dilutions enabled to detect a transition at log(C) = 0.8, which means a *cac* of 2.2 g/L.

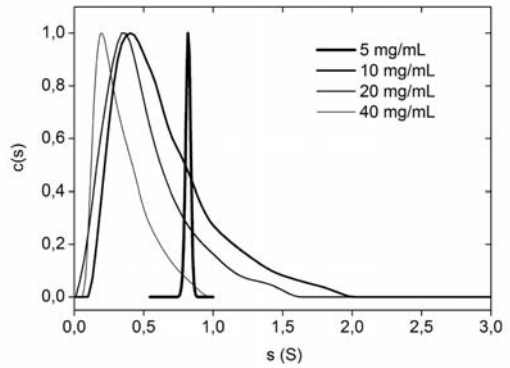

Figure 8. Sedimentation coefficient distributions of aqueous solutions of PEO_{113}-$PMOXA_{118}$ at different concentrations.

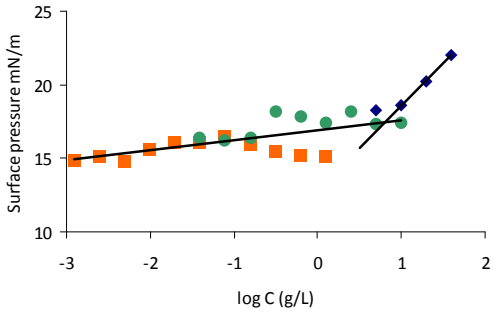

Figure 9. Surface pressure of solutions of PEO_{113}-$PMOXA_{118}$ (three series of dilutions).

The viscosity of PEO_{113}-$PMOXA_{60}$ and PEO_{113}-$PMOXA_{118}$ solutions above 5 g/L follows a linear trend without transition, which suggests stable particles (Figure 10), in agreement with SLS. The apparent transition between 3 and 5 g/L with the subsequent increase in viscosity below 3 g/L is a logarithm artifact often appearing when viscosity decreases below 10% of that of the solvent. Factors contributing to this artifact include a small error on concentration or apparatus calibration, or polymer adsorption on the glass capillary,[135] which is likely with hydrophilic macromolecules (and reduces the effective concentration). Leaving out the points below 3 g/L, by extrapolation to zero concentration we calculate respective intrinsic viscosities ($[\eta]$) of $(1.9 \pm 0.1).10^{-2}$ L/g and $(2.4 \pm 0.1).10^{-2}$ L/g. These two values are reported on Figure 11 and compared to PEO homopolymers of the same molar masses.[136] The intrinsic viscosities of both diblocks are very close to that of PEO. Viscosimetry therefore suggests single polymer chains, which is in contradiction with LS and TEM data. Our hypothesis is that the shear stress of laminar flow through the capillary may disrupt the fragile aggregates.

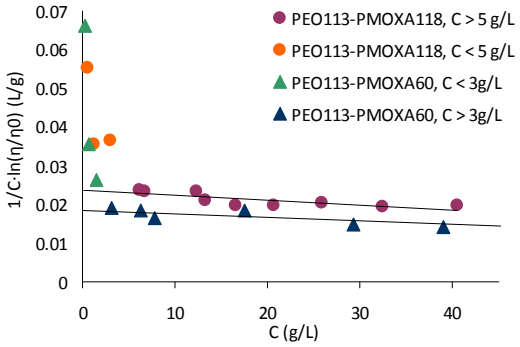

Figure 10. Viscosimetric data of PEO-PMOXA; Lines: Extrapolation to intrinsic viscosities.

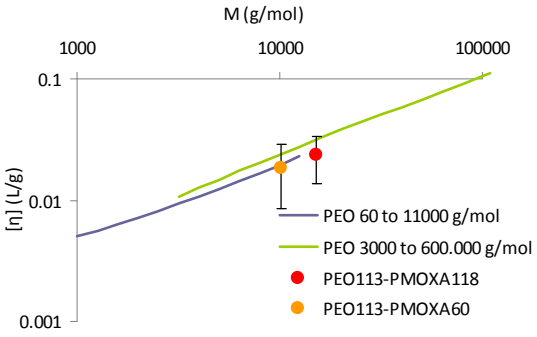

Figure 11. Intrinsic viscosities of PEO-PMOXA compared with PEO homopolymers.

To further investigate the nature of the interaction driving the self-assembly and to study the aggregate dynamics, ^{1}H-NMR spectroscopy experiments in D_2O was performed. Figure 12 shows a 2D NOESY NMR spectrum from the polymer aggregates in D_2O. Only one set of signals was observed at a polymer concentration of 60 g/L at 298K, indicating that the exchange between monomeric and self-assembled chains is rapid on the millisecond time scale. NOESY experiments revealed only contacts within the backbone (-C_2H_4-) of the PMOXA block as well as between the backbone and the branch (N-(CO)-CH_3). The inter- or intra-molecular nature of these contacts cannot be unambiguously identified because they are acquired as one signal. In contrast, NOESY clearly shows that no interactions between the PEO and the PMOXA blocks can be observed by NMR. Therefore, we measured in parallel diffusion coefficients of chemical groups detectable by NMR (DOSY, Table 1). It clearly appears that beside the quickly-diffusing signals of water and traces of tosyl groups from the synthesis, all hydrogen atoms from the polymer appear to diffuse at the same speed, which is

comparable to the diffusion of single chains. Here again, it is possible that aggregates are disrupted by the high speed of rotation of the NMR tube, or since NMR is sensitive to the number average, it might only detect the dominant signal of single chains.

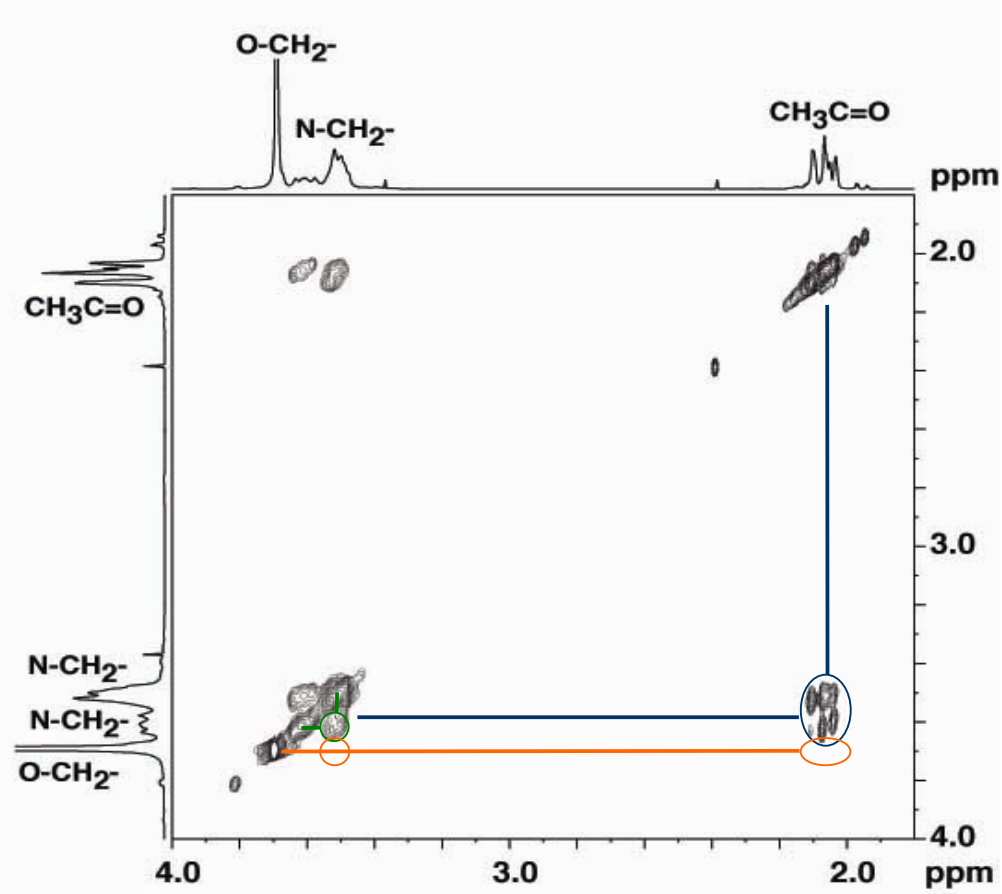

Figure 12. Spatial spin coupling: 2D-NMR NOESY of PEO_{113}-b-$PMOXA_{118}$ in D_2O at 60 g/L. Green: PMOXA / PMOXA backbones; Blue: PMOXA backbone / PMOXA amide branch; Orange: no coupling with PEO.

Table 1. H^1DOSY diffusion coefficients and apparent hydrodynamic radii, assuming hard spheres. Orange: signals from the polymer; Green: traces of impurities from the synthesis; Blue: water.

δ (ppm)	assignment	diffusion coefficient (m^2/s)	Apparent R_H (nm)
3.671	O-CH_2-CH_2-O	7.26E-11	1.10
3.665	N-CH_2-CH_2-N	7.411E-11	1.08
3.348	PEO-CH_3	7.993E-11	1.00
2.011	NCO-CH_3	8.819E-11	0.91
2.075	NCO-CH_3	9.106E-11	0.88
3.497	N-CH_2-CH_2-N	9.901E-11	0.81
7.343	Tos-OH	6.561E-10	0.12
2.363	Tos-CH_3	6.693E-10	0.12
4.775	H_2O	2.11E-09	0.04

In order to determine which block is likely to create the core of the aggregates and which one tends to form the corona, we have performed water uptake experiments with PEO_{113} and $PMOXA_{118}$ homopolymers in a controlled atmosphere of 85% humidity at different temperatures. Figure 13 shows that PMOXA takes up roughly ten times more water than PEO at 18°C. Both polymers show an increased water uptake at 25°C, but still the PEO is much less prone to water uptake. As a result, the water uptake measurements suggest that the PMOXA block is more hydrophilic, therefore more easily hydrated, and thus forms the outer part of the aggregate, whereas the PEO block forms the core.

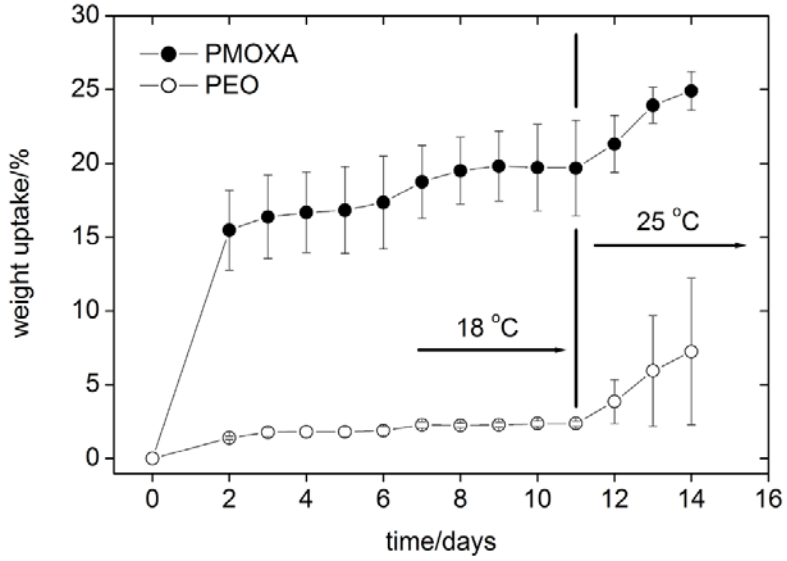

Figure 13. **Degree of swelling of PEG_{113} and $PMOXA_{118}$ homopolymers.**

Results are summarized in Table 2. Using LS, TEM, surface tension measurements and AUC, we showed that poly(ethylene oxide)-*block*-poly(2-methyl-2-oxazoline) diblock copolymers self-assemble in aqueous solution. Moreover, SAXS indicates that the number-dominant structures are rod-like entities, which, according to TEM, are also at the core of the aggregates. Water uptake measurements show that PMOXA is considerably more hydrophilic and can bind more water molecules than PEO. This in turn suggests that the PMOXA block has a larger hydrodynamic volume than PEO block at comparable block length (secondary structure), and tends to form a corona while the PEO block tends to form the core of the aggregates (tertiary structure). Finally, NMR shows that there is no interaction between the two blocks, which suggests that the core and the corona of the aggregates are well-separated.

While from polymer thermodynamics it can be expected that the different blocks of the polymer do not mix upon aggregation, the main question is why there is an aggregation process at all. In principle, as both blocks are hydrophilic, aggregation cannot necessarily be expected. Our data suggest that differences in hydrophilicity, as found in the water uptake experiments, may contribute

to the formation of well-defined aggregates in aqueous solution. This finding raises the question of entropic contributions. Typically, aggregation of amphiphilic molecules is driven by an entropy gain upon aggregation, which is, to a first approximation, caused by the release of water molecules bound via the hydrophobic effect from the hydrophobic parts of the amphiphile. In the current case however, we showed that even PEO, which is in the core of our aggregates, takes up a significant amount of water. This suggests that the effect is more likely hydrophilic in nature rather than hydrophobic. As dynamic light scattering gives evidence for two populations above the *cac*, our data suggest that the entropic barrier between aggregation and single chains in solution may be very low, because there is no entropy gain by aggregation.

Aggregation could therefore be initiated by favorable intermolecular PMOXA / PMOXA interactions, increasing the local polymer concentration. In a second step, the gradient of hydrophilicity could drive a local (PEO in water) / (PMOXA in water) mesophase separation, similarly to the segregation previously studied at high concentration. The less hydrophilic PEO block, with a slightly smaller hydrodynamic volume, is then constrained at the core of the aggregates. Both mesophases are stabilized by hydrogen-bond bridges from water molecules.

From these results we suggest a model for the ternary structure. We believe that these structures coil into a quaternary structure, into approximately spherical, water-swollen gel particles with a hydrodynamic radius of about 100 nm (Scheme 3). The rod shape must come from the relative similarity of the blocks respective hydrodynamic volumes. It would be interesting to test if higher PMOXA / PEO size ratios favor the formation of bis-hydrophilic micelles, and if smaller ratios favor so-called 'Janus micelles' i.e. micelles without a core but split into two segregated hemispheres.

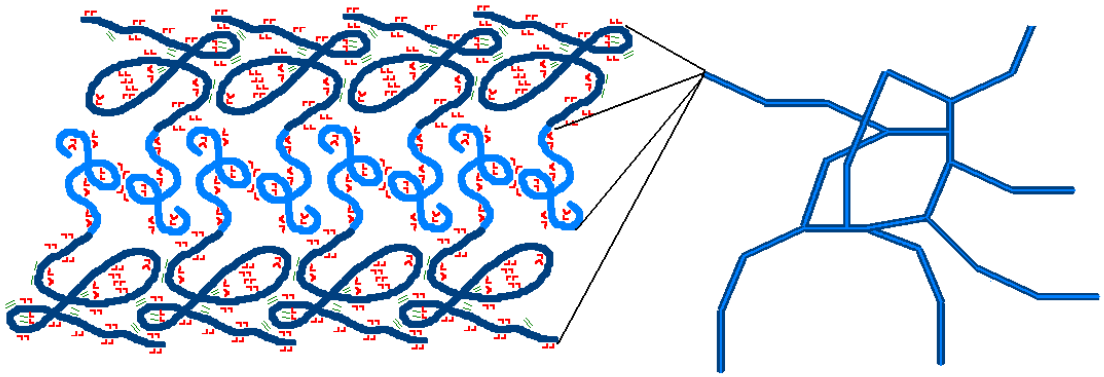

Scheme 3. Suggested ternary and quaternary structures: rod-like filaments and water-swollen gel. Light blue: PEO block; dark blue: PMOXA block; green: PMOXA / PMOXA spatial interactions; red: polymer-bound, bridge-binding water molecules.

Table 2. Summary of results.

Technique	Result	Interpretation
Existence and characterization of the aggregates		
TEM (20 g/L)	Spheres R = 100-200 nm (circular areas of higher filament density) Filaments (thickness 4 nm)	Filaments and loose hydrated aggregates
DLS, SLS (2 - 60 g/L)	$R_{H,1}$ = 2 nm (monodisperse) $R_{H,2}$ = 100 nm (broad distribution) R_G = 70 nm (polydisperse colloid, random coil model) $R_G/R_{H,2}$ = 0.7 : hard spheres M_W = 200000 g/mol Little contrast (*dn/dC* = 0.16 mL/g) No significant intensity below 1 g/L	DLS detects Brownian motion of both filaments and aggregates. Polydisperse hard spheres
SAXS (20 g/L)	Rod-like entities of length 6.7 nm and radius 0.9 nm	Rod-like filaments are the number-dominant species. 6.7 nm is a measure of the persistence length. No large aggregate measured as an effect of the number-average.
Surface tension (0 - 40 g/L)	*cac* = 2 g/L	Existence of a phase transition in solution.
AUC (5 - 40 g/L)	5 < *cac* < 10 g/L C < 10 g/L: short sedimentation time, narrow distribution of sizes C > 10 g/L: long sedimentation time, broad distribution of sizes	Polydisperse aggregates are detected above 5 - 10 g/L
Inconclusive methods		
Viscosimetry	Intrinsic viscosity of PEO-PMOXA comparable to that of PEO	Single chains: aggregates may be disrupted by shear stress
2DNMR-DOSY (60 g/L)	R_H = 0.9 nm	Single chains: aggregates may be disrupted by shear stress from the tube rotation, and/or effect of the number-averaged signal.
Qualitative measurements of driving forces		
2DNMR-NOESY (60 g/L)	PMOXA / PMOXA spatial spin coupling, either intra or intermolecular	Intermolecular self-affinity potentially one driving force at the molecular scale
Swelling	PMOXA takes up roughly ten times more water than PEO	The gradient of hydrophilicity is a potential driving force for the block segregation; PEO will tend to form a core and PMOXA a corona.

2. Mineralization of calcium phosphate in presence of DHBC

In order to use these polymeric structures as templates for CaP, a controlled quantity of PEO_{113}-$PMOXA_{118}$ was added to a 120 mM solution of K_2HPO_4 and a separate 240 mM solution of $CaCl_2$. The Ca/P ratio of 2 was chosen because it favors the formation of hydroxyapatite (HAp), the biologically most relevant crystal phase and the most stable at basic pH. The two solutions were adjusted to pH 9 with a concentrated KOH aqueous solution, and then mixed. The final concentration of polymer ranged from 1% to 80% w/w of the polymer-water mixture. Stirring was not used during the maturation time of 2 days in order to prevent disrupting the polymer aggregation. Samples were then centrifuged and rinsed with ethanol twice, then freeze-dried.

The presence of polymer at various concentrations in the crystallizing solution does neither modify the crystal phase nor the crystal morphology. All SEM micrographs (Figure 14) show monodisperse beads of 40 to 50 nm in diameter, as well as in the control (polymer free) samples. The bead shape is characteristic of the initial formation of amorphous CaP (ACP), the hydrated $Ca_3(PO_4)_{2,aq}$ precipitate which may mature according to the pH into several crystal phases. The beads are the site within which crystal nucleation occurs. There is no sign of templating by the polymer aggregates. The beads are clearly made of HAp according to XRD (Figure 15), since there is a good match between the experimental spectra and the theoretical diffraction peaks of HAp. Therefore, the nucleation of HAp did happen, but despite the high water content of the DHBC, the ACP bead formation prevented nucleation from happening in the presence of polymer aggregates, possibly because these aggregates do not resist any mechanical stress. Obviously, PEO-PMOXA copolymers do not interfere with the crystallization of HAp.

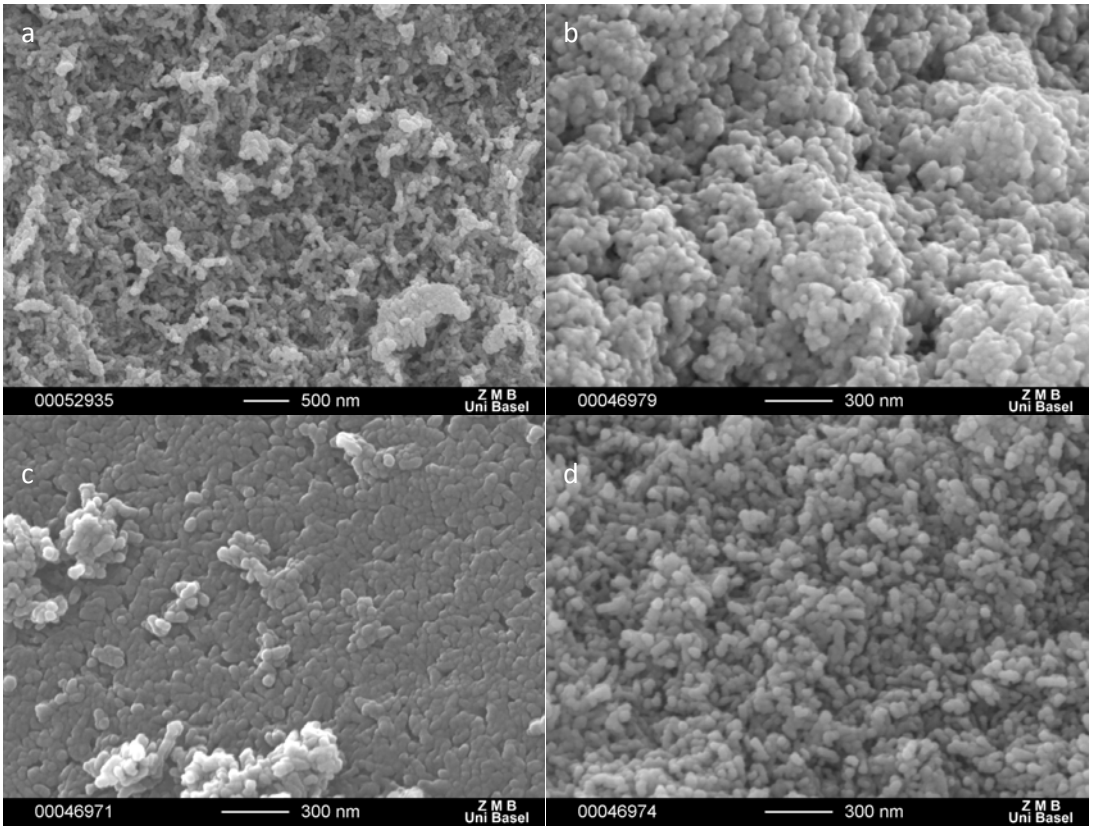

Figure 14. SEM micrographs of CaP mineralized with PEO_{113}-$PMOXA_{118}$ at polymer concentrations a) control; b) 10%; c) 50%; d) 80%.

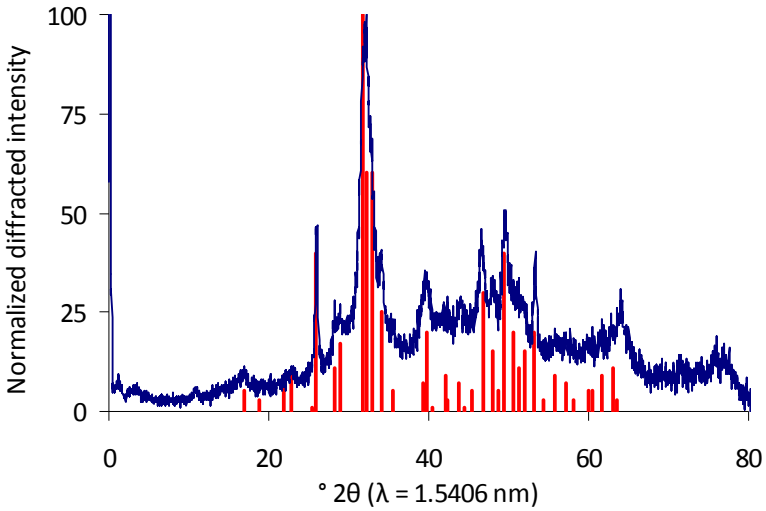

Figure 15. Powder-XRD spectrum of CaP mineralized in presence of PEO_{113}-$PMOXA_{118}$. Blue: experimental spectrum; Red: HAp main theoretical diffraction peaks.

B. Amphiphilic poly(ethylene oxide)-block-poly(valerolactone) diblock copolymers as template for calcium phosphate mineralization

Similarly to the study of the DHBC, the aim of this study is to evaluate the potential of PEO-b-poly(valerolactone) (PEO-PVL) ABCs as an engineering platform for the fabrication of CaP-polymer scaffolds. The ester bonds make this ABC degradable in strongly acidic and basic pH and a candidate for biodegradable implant materials. The crystallization of CaP in presence of PEO-PVL is presented after the self-assembly properties of the pure polymer in aqueous solution.

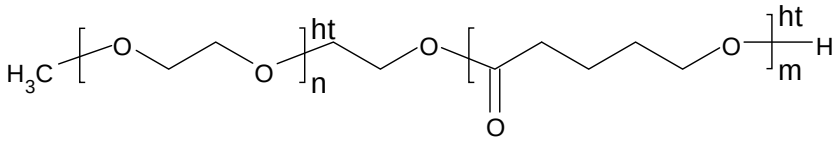

Scheme 4. Chemical formula of poly(ethylene oxide)-*block* -poly(valerolactone)

1. Self-assembly in aqueous solution

Light scattering confirms that the size of the aggregates depend strongly on the dissolution procedure. The solubility is essentially given by the length and crystallinity of the hydrophobic poly(valerolactone) block. It makes the polymer poorly soluble since, after extended heating at 60°C with sonication, only turbid suspensions were obtained. All PEO-PVLs form a mixture of micelles and much larger particles (incomplete solubilization). DLS of PEO_{113}-PVL_{20} (Figure 16) shows that micelles have a hydrodynamic radius of about 10 nm. This peak cannot be fitted more accurately because the scattered intensity is dominated by the particles larger than 100 nm. However, repetitions of the experiment however confirm the presence of the peak. Furthermore, representative cryo-TEM micrographs on the same samples also indicate that the polymers form polydisperse aggregates of diameter ranging from 15 to 40 nm (Figure 18).

The second peak can be studied in SLS. A typical Zimm analysis (Figure 17) indicates an average radius of 310 nm and a molar mass corresponding to an aggregation number of more than 15000 polymer chains.

In conclusion, the polymers self-assemble into kinetically frozen micelles of diameters ranging from 15 to 40 nm as dominant population. It would probably be interesting to test other formulations, such as using ethanol as co-solvent (yielding monodisperse micelles of radius 15nm).

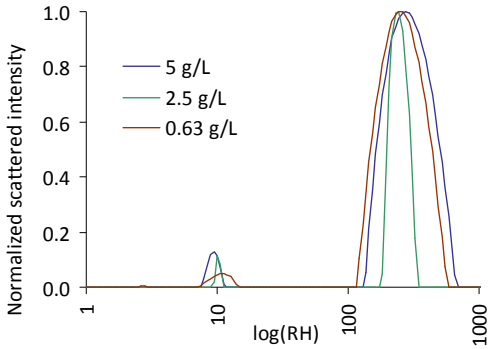

Figure 16. DLS data of PEO-PVL$_{20}$ block copolymers in aqueous solution.

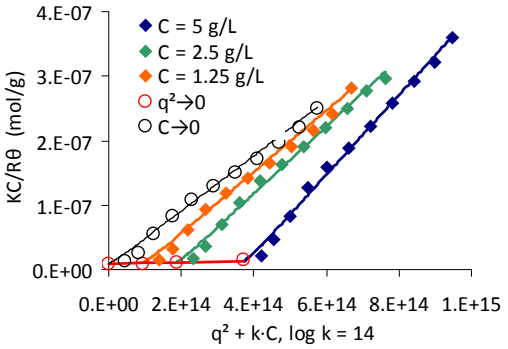

Figure 17. SLS data of PEO-PVL$_{20}$ block copolymers in aqueous solution (Lines are simulated data).

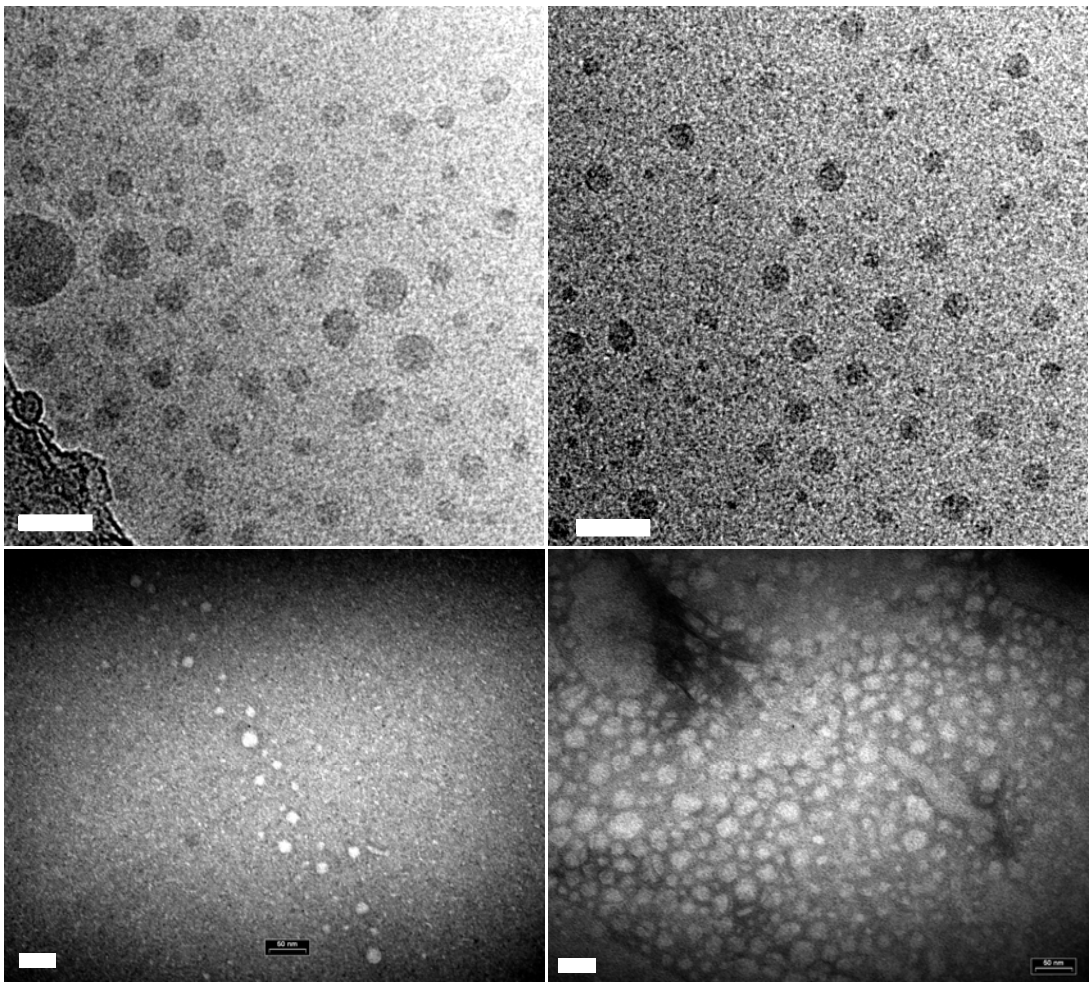

Figure 18. Micelles formed by (left) PEO$_{113}$-PVL$_{20}$ and (right) PEO$_{113}$-PVL$_{45}$. Up: Cryo-TEM; Down: TEM micrographs. Scale-bar: 50 nm.

2. Crystallization of calcium phosphate in presence of neutral micelles

In order to compare results with the mineralization of CaP in presence of DHBC, we used the same mixing procedure as for the DHBC: two aqueous polymer solutions containing either the

phosphate or the calcium source are prepared separately, then mixed. The same concentrations of calcium and phosphate sources were used i.e. respectively 240 mM and 120 mM. However, crystallizations proceeded under stirring to enable a quicker maturation, and several pH systems were studied. They are summarized in Table 3 and described below. In all cases the source of calcium cations was calcium nitrate dihydrate $Ca(NO_3)_2$, 2 H_2O.

Crystallizations of CaP typically proceed as follow. Upon mixing, the two calcium and phosphate sources instantly precipitate into amorphous calcium phosphate (ACP). This precipitate is a gel of amorphous beads of diameters up to 50 nm (Figure 19a, obtained after 1 day of maturation without stirring). If the phosphate source contains hydrogenophosphate anions (e.g. $K_2H(PO_4)$), the protons are released upon precipitation, which decreases the pH. In the absence of pH control, this first step strongly influences the solution pH (Equation 1). This is the reason for the quick initial pH drop in system (1), from 9 to 6 in 1 hour. As a second step, the crystal nucleation and maturation occur inside the ACP beads depending on the pH. In the case of a mildly basic pH, the subsequent maturation into HAp involves the uptake of hydroxide ions (Equation 2), which further decreases the pH. This explains the slight drop from 9 to 8 or from 8 to 6 in systems (2) and (3) respectively, pH 6 being the stability limit of HAp. Below pH 6, DCPD is the dominant crystal phase. Three methods allow keeping the pH high during maturation in order to crystallize HAp. First (as a first step towards the constant-composition method), this drop can be compensated for by progressive pH readjustment during the first hours of the crystallization (system (2)). Caution must be given that the pH does not approach 10 because this triggers the unwanted precipitation of calcium hydroxide. A second method involves a buffer, often an organic molecule such as the TRIS buffer (of chemical formula $H_2N\text{-}(OH)_3$ in the basic form ; its pKa of 8.06 is ideal to maintain a mildly basic pH). Since buffers are by definition introduced in high concentration, they are susceptible to interact with the crystals or the polymer. This method was therefore avoided. Third, the drop to acidic pH can also be prevented by using pH-neutral counter-ions $K_3(PO_4)$ (system (3)). The advantage of this method lies in not increasing the ionic strength with pH control species.

$3\ Ca^{2+} + 2\ HPO_4^- \rightarrow Ca_3(PO_4)_{2,\ aq.} + 2\ H^+$

Equation 1. pH decrease during precipitation of amorphous CaP.

$5\ [Ca_3(PO_4)_2] + 2\ OH^- + H_2O \rightarrow 3\ [Ca_5(PO_4)_3OH] + HPO_4^{2-}$

Equation 2. ACP to HAp transition

In summary, three crystallization systems were studied, which differ mostly in the pH at which the maturation occurs: strongly acidic in system (1), slightly basic in system (2) and close to neutral in system (3).

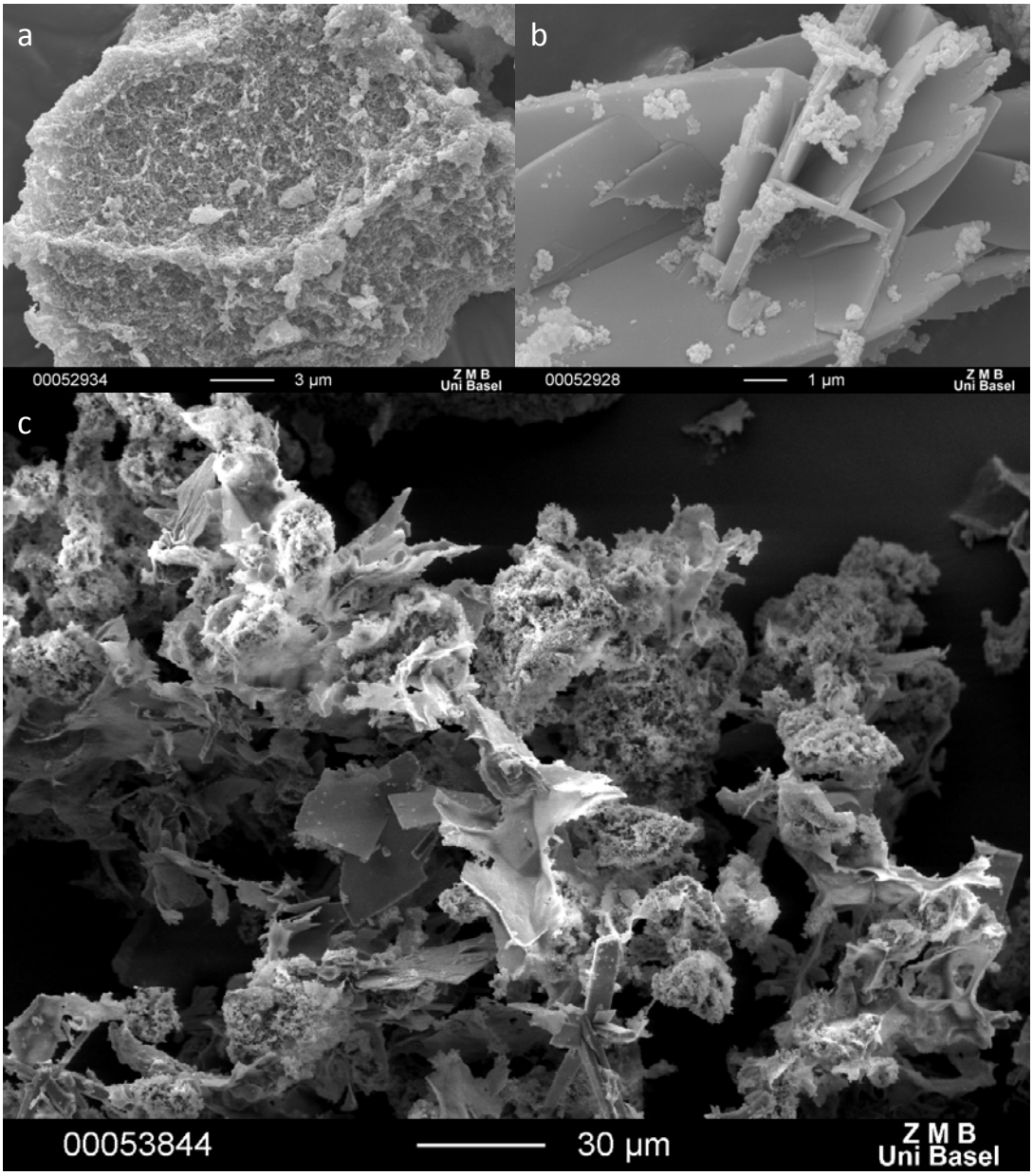

Figure 19. Control experiments. SEM captures of the ACP to DCPD maturation at acidic pH (system (1)). a) Initial ACP precipitate; b) Mature DCPD crystals with poorly crystalline traces; c) Transition.

Table 3. Mineralization parameters.

	Phosphate source	pH adjustment of initial solutions	pH control during maturation	pH after 1 h / final pH	Maturation time
(1)	(NH4)2H(PO4)	pH 9 (NH4OH)	Without pH control	6 / 5.5	12 hours, 1-7 days
(2)	(NH4)2H(PO4) or K2H(PO4)	pH 9 (NH4OHcc or KOHcc)	pH readjusted to 9 (KOHcc), progressively until stabilization (1 h)	9 / 8	1-3 hours, 7 days
(3)	K3(PO4)	pH 9 (NH4OH)	Without pH control	8 / 6	3 hours

Figure 20 and Figure 23 gather typical XRD patterns of CaP crystallized respectively at low and high pH. At high pH, the patterns match with the theoretical diffraction peaks of DCPD. Sometimes, traces of OCP appear, but there is no difference between the samples containing polymer and the control (polymer-free) samples. The crystal phase of the resulting mineral is therefore entirely determined by the pH and not by the presence or concentration of polymer. Additionally, XRD shows no difference between the sampled quenched after 24h and those after seven days. This indicates that the crystallization is essentially terminated within 24 hours, which in general is interesting for further experimentations, not only with PEO-PVL. From the morphological point of view, samples observed in SEM typically consist in a mixture of large thin plates of 10 to 200 µm (DCPD crystal habit) and a porous material. On Figure 21 are gathered several relevant captures. The DCPD plates are the ultra-dominant species (possibly 99% in mass as a rough estimation on whole sample plates), while the porous material is present as traces. These porous materials exhibit various morphologies: the foam on Figure 22 (24 hours of maturation) seems to mature into the porous material shown on Figure 21 (seven days of maturation), which is probably OCP. Again, however, all patterns are identical in the presence or in the absence of polymer; therefore the variations in porosities must be due to other parameters such as sample handling.

Upon mineralization at high pH, hydroxyapatite (HAp), the most stable CaP crystal phase, forms. Similarly, the patterns of CaP crystallized at basic pH in presence of polymer are identical to the control experiments, in that they exhibit spherical particles with a diameter of ca. 50 nm, which aggregate into more or less porous structures (Figure 24). The porosity is not controlled by parameters such as the maturation time and is probably due to sedimentation during centrifugation.

Finally, samples crystallized close-to-neutral pH (Figure 25) did not yield significantly different results. SEM samples seem to exhibit a combination of the morphologies and phases previously observed i.e. HAp, but still without polymer effect.

In conclusion, replacing the poly(methyl oxazoline) block with a biodegradable hydrophobic poly(valerolactone) (PVL) with different degrees of polymerization proves insufficient to create an interaction with the crystallization of CaP, in the conditions that we tested.

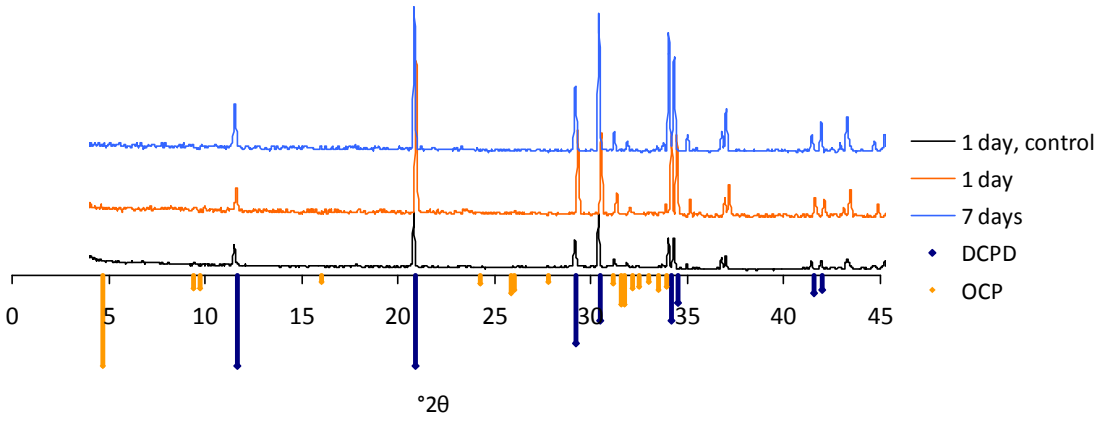

Figure 20. XRD spectra of CaP crystallized in a 50 g/L solution of PEO-PVL$_{20}$ at pH 5.5; DCPD and OCP theoretical patterns.

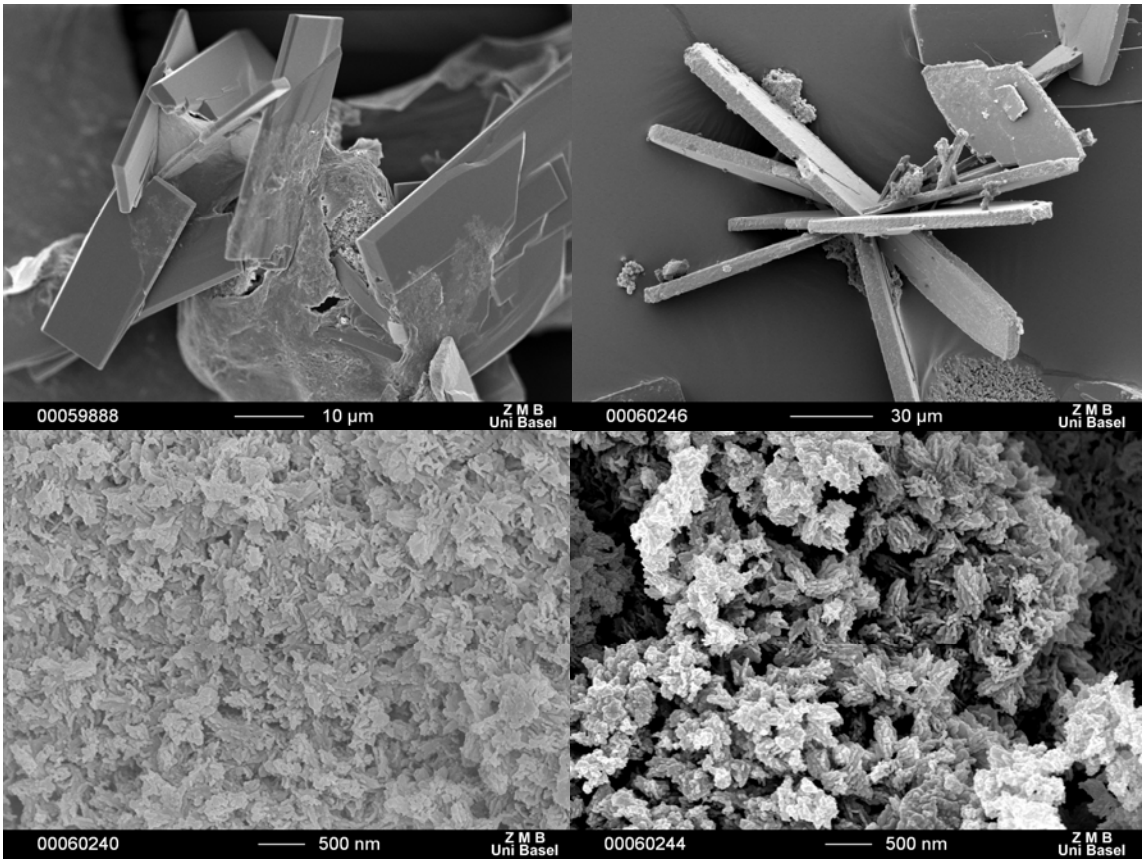

Figure 21. SEM of CaP mineralized at pH 5.5 after seven days of maturation. Up: DCPD dominant fraction; Down: traces (probably OCP); Left: control; Right: in a 50 g/L aqueous solution of PEO-PVL$_{45}$.

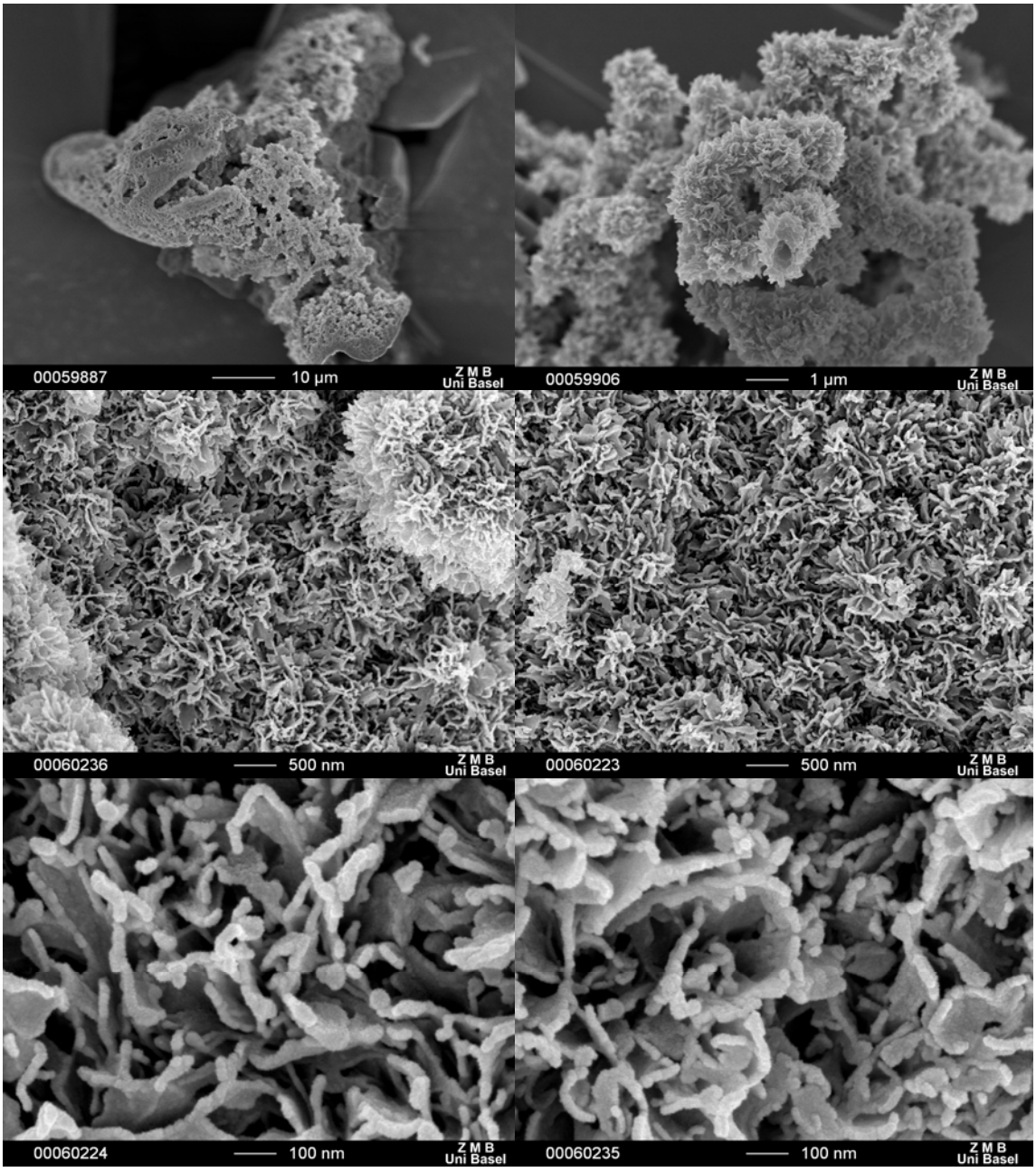

Figure 22. SEM of CaP mineralized at pH 5.5 after 24 hours: ACP traces. Left: control; Right: in a 50 g/L aqueous solution of PEO-PVL$_{45}$.

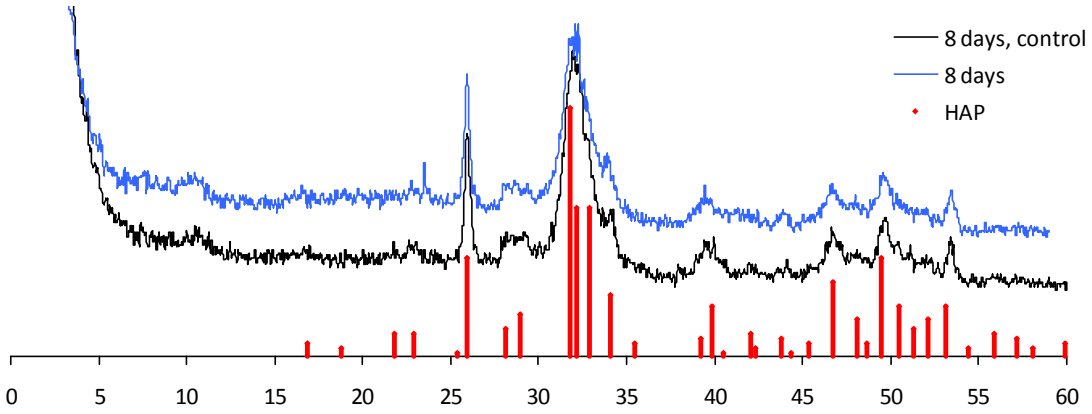

Figure 23. XRD data of CaP mineralized at basic pH; HAp theoretical pattern.

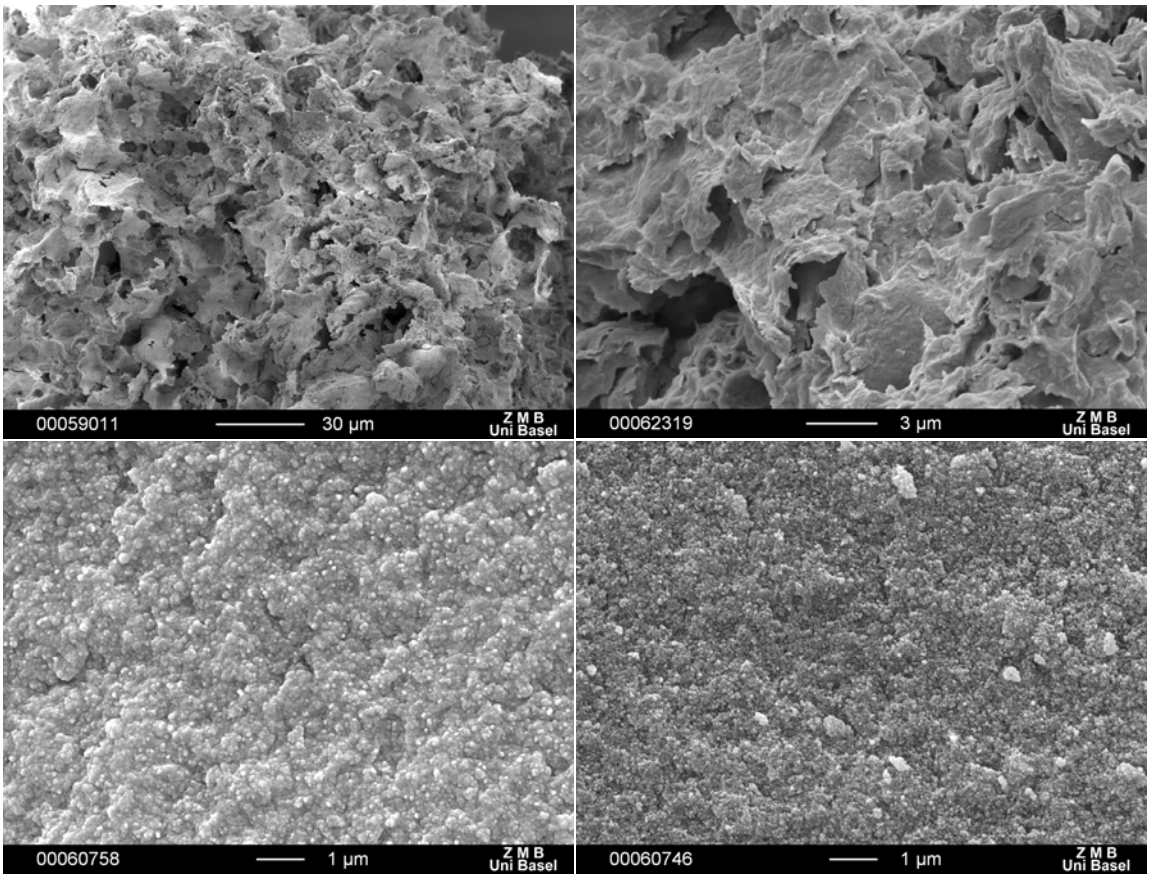

Figure 24. SEM of CaP mineralized at high pH. Top: 1 day; bottom: 8 days; Left: control; Right: in presence of PEO-PVL$_{20}$ (50g/L).

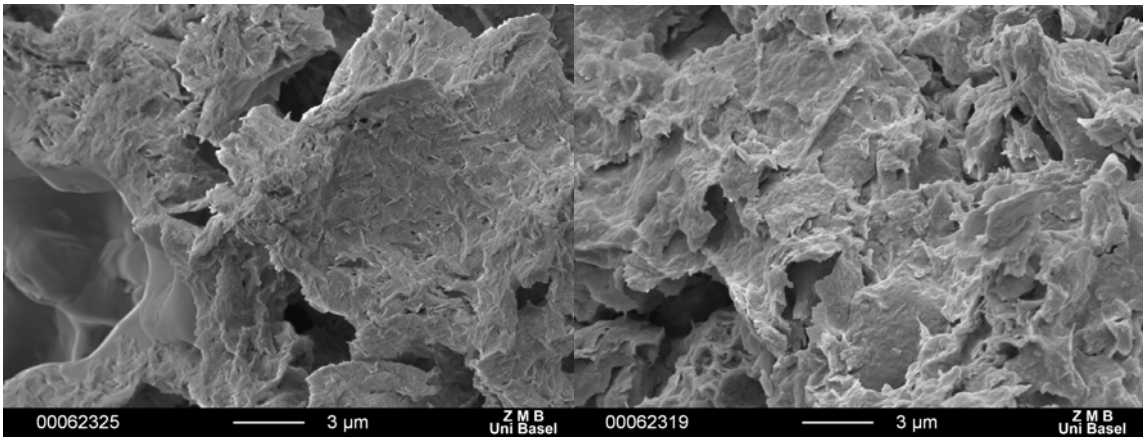

Figure 25. SEM of CaP crystallized at neutral pH in presence of a) PEO-PVL_{20} b) PEO-PVL_{45}.

C. poly(n-butylacrylate)–block–poly(acrylic acid) templating calcium phosphate monolayers at the air-water interface

This chapter is constituted by the following publication : CaP mineralization beneath monolayers of poly(n-butylacrylate)–block–poly(acrylic acid) block copolymers, Olivier Casse, Olivier Colombani, Katarzyna Kita-Tokarczyk, Axel H. E. Müller, Wolfgang Meier and Andreas Taubert

Calcium phosphate mineralization beneath monolayers of poly(*n*-butylacrylate)–block–poly(acrylic acid) block copolymers

Olivier Casse,[a] Olivier Colombani,†[b] Katarzyna Kita-Tokarczyk,[a] Axel H. E. Müller,[b] Wolfgang Meier*[a] and Andreas Taubert*[ac]

Received 24th October 2007, Accepted 14th December 2007
First published as an Advance Article on the web ?????
DOI: 10.1039/b716353c

Amphiphilic poly(acrylic acid)–block–poly(*n*-butylacrylate) block copolymer films at the air–water interface have been mineralized with calcium phosphate. The polymers form stable monolayers at the free surface. Their stability is virtually independent of ion strength or pH changes in the subphase. The outcome of calcium phosphate crystallization depends on the calcium and phosphate concentrations, the stirring rate of the subphase, and the subphase pH. At low calcium and phosphate concentrations (2 mM), uniform polymer–calcium phosphate hybrid films form. Higher calcium and phosphate concentrations yield less ordered films, which often contain large blocks of material beneath the polymer monolayer. Occasionally, also filaments similar to samples described by Peytcheva *et al.* (*Colloid Polym. Sci.*, 2002, **280**, 218) are observed. Films mineralized at pH values below *ca.* 6 contain particles that are a few nanometers apart and the resulting films retain some flexibility. Films grown above pH 6 have a higher degree of mineralization. They are stiff and tend to break upon mechanical stress. Overall, the paper illustrates that low calcium phosphate supersaturation in the subphase and a well-defined (but not crystalline) interface are crucial for controlling calcium phosphate mineralization. As a result, the current study could serve as a model for biological mineralization which is more closely related to Nature than films made from *e.g.* detergents or low molecular mass compounds.

Introduction

Block copolymers have attracted a tremendous amount of attention due to their wide range of applications. In particular, amphiphilic block copolymers have found applications in the cosmetics, food, medical and waste water treatment industries, to just name a few examples.[1,2] Amphiphilic block copolymers self-assemble in aqueous solution in order to minimize contacts between the hydrophobic block and water,

[a]*Department of Chemistry, University of Basel, Klingelbergstr. 80, CH-4056 Basel, Switzerland. E-mail: wolfgang.meier@unibas.ch; Tel: +41 (0)61 267 38 02*
[b]*Department of Chemistry, University of Bayreuth, D-95440 Bayreuth, Germany*
[c]*Institute of Chemistry, University of Potsdam and Max-Planck-Institute of Colloids and Interfaces, 24–25, Building 26, D-14476 Golm, Germany. E-mail: ataubert@uni-potsdam.de; Tel: +49 (0)331 977 57 73*

† Present address: Laboratoire Polymères, Colloïdes et Interfaces, UMR 6120, Université du Maine, 1, Avenue Olivier Messiaen, 72085 Le Mans Cédex 9, France.

and yield well-organized aggregates [1,3,4] which in some cases include bio-functionalities or bio-inspired responsive blocks, see *e.g.* ref. 5–9

Amphiphilic block copolymers containing a (stimulus-responsive) polyelectrolyte block as the hydrophilic part are of particular interest to the scientific and industrial community. This is due to the fact that pH, ionic strength or temperature allow for a tuning of the behavior of the respective aggregates[4,10–12] which will, for example, allow for the fabrication of robust and simple formulations for the food and cosmetics industries.

We have recently shown that poly(*n*-butylacrylate)–block–poly(acrylic acid) (P*n*BA-PAA) block copolymers spontaneously self-assemble into monodisperse spherical aggregates when dispersed in aqueous solution.[13–15] The presence of the PAA block enables the variation of the size of the aggregates by changing the salt concentration.[13] However, no significant pH dependence was observed, which was explained by the fact that the aggregates are kinetically frozen—that is, out of equilibrium—in spite of the very low glass transition of the P*n*BA block ($T_g = -55$ °C).

Beside their behavior in bulk solution, block copolymers have also been studied at the air–water interface.[16–19] In general, polymer monolayers are characterized by less-sharp phase transitions in 2D than films of low molecular weight amphiphiles. This is the result of a stronger cohesion between the considerably larger hydrophobic chains in polymers. A further parameter affecting polymer organization at the surface is the space limitation imposed on the system by the hydrophilic blocks. As a result, amphiphilic block copolymers tend to form more stable and reversibly compressible monolayers. Additionally, conformational changes play an important role. As the polymer is compressed from a random coil to a brush conformation, wide plateaus in the compression isotherms are observed, for example in poly(2-methyl-2-oxazoline)–block–poly(dimethylsiloxane)–block–poly(2-methyl-2-oxazoline) (PMOXA–PDMS–PMOXA)[20] or poly(ethylethylene)–block–poly(ethylene oxide) (PEE-PEO)[17] copolymers. Due to their molecular structure, block copolymer films are also characterized by large lateral compressibilities.[21]

Finally, amphiphilic block copolymers, but also so-called bis-hydrophilic block copolymers, have been used to engineer the sizes, shapes, crystal phases and 1D, 2D and 3D organization of inorganic particles. Here, the block copolymers act as growth- and structure-directing additives, where the chemistry, structure, and architecture of the polymer has a dramatic influence on the outcome of the growth of the inorganic.[22–35] Interestingly, however, there have been no studies on the mineralization of block copolymer films at the air–water interface.

This is intriguing because there have been a series of studies on the mineralization of low molecular mass compounds and other small molecules with a variety of inorganics.[34,36–43] Furthermore, lipid-like peptide monolayer films have been shown to be strong growth modifiers for calcium carbonate.[43] As a result, it is known that the crystallization of inorganics can in many cases be readily controlled by the chemistry or the charge of the monolayer. However, reservations about the analogy between surfactant monolayers and biological systems (which are often claimed to be an inspiration for monolayer mineralization experiments) remain. For example, biological mineralization scaffolds are polymeric in nature and rarely crystalline (which many of the surfactant monolayers are). In contrast to what is observed with crystalline monolayers of low molecular mass surfactants, biomineralization is controlled to quite some extent by the interaction of a polymeric, more or less well-organized, substrate (interface) with a growing inorganic.[44–47] This suggests that well-organized but flexible and soft polymeric substrates or interfaces could be prime candidates for studies into both technologically important mineralization processes and biomineralization. It therefore seems straightforward to transfer the concept of Langmuir film mineralization from low molecular mass surfactants to polymeric films.

One of the most important biominerals is calcium phosphate (CaP) which is, among others, the main component of mammal bone.[44,46] For the above reasons

and because of the ever-growing demand for long-lasting, high-quality implants, it is interesting to quantitatively understand CaP nucleation, growth and also its degradation at various interfaces.

Indeed, a tremendous amount of work has been dedicated to the controlled fabrication of CaP from aqueous and organic solution.[34,48,49] Surprisingly, however, apart from one study on CaP formation under a low molecular mass surfactant film,[50] a few studies on CaP growth on solid films[51–54] and a few studies on CaP growth in polymer vesicles and concentrated polymer solution,[5,55] there are no reports on the effect of polymeric surfaces or interfaces on CaP growth. As a result, this report is to our knowledge the first study on CaP mineralization of polymeric Langmuir films, even though the effect of dissolved poly(acrylic acid) on the mineralization of $CaCO_3$ under a Langmiur film and CaP formation under surfactant films have been studied.[39,50]

Results and discussion

1. Polymers at the air–water interface

Amphiphilic poly(*n*-butylacrylate)–block–poly(acrylic acid) (P*n*BA-PAA) diblock copolymers were prepared by atom transfer radical polymerization (ATRP) of *n*-butylacrylate and *tert*-butylacrylate (*t*BA), followed by selective acidolysis of the P*t*BA block into PAA using a previously reported procedure.[14] Table 1 summarizes the properties of the polymers used in the current study.

Polymer monolayers were prepared by spreading an aliquot of polymer solution in chloroform–ethanol (90 : 10 v/v) at the air–water interface. The subphase pH was adjusted to 2.6 or 11.4 by HCl or NaOH respectively. To account for charge screening and charge density effects, measurements were done on various salt-containing subphases at three different pH values. Out of the polymers available (Table 1), we have focused on polymer OC31 ($PnBA_{90}$-PAA_{300}, $M = 33\,000$ g mol^{-1}, obtained after acidolysis of $PnBA_{90}$-$PtBA_{300}$). $PnBA_{90}$-PAA_{300} contains the longest acrylic acid block of all polymers used in this study. This feature is advantageous for behavior tuning by pH variation and salt addition at the air–water interface because stronger responses can be expected with a longer block.

Fig. 1 clearly shows that $PnBA_{90}$-PAA_{300} produces monomolecular films at the air–solution interface by compression on a Langmuir trough. Depending on the experimental conditions, the lift-off areas range from *ca.* 35 to 40 nm^2. Considering the molecular mass and dimensions of the macromolecules, those values are realistic and indicate a condensed liquid state packing of $PnBA_{90}$-PAA_{300}. Importantly, we do not observe material loss into the subphase even at high pH, where the PAA block is fully deprotonated (pK_a *ca.* 4.5). This shows that hydrophobic interactions stabilize the film enough to prevent desorption into the aqueous bulk. This finding is consistent with the fact that the P*n*BA-PAA diblock copolymers form kinetically frozen aggregates in aqueous solution, where the exchange of unimers between the aggregates and the aqueous phase is very slow.[13]

The characteristic, small surface pressure "plateau" region (*ca.* 5 mN m^{-1}) corresponding to molecular areas larger than 38 nm^2 is attributed to the transition between an expanded liquid phase and a liquid (organized) film. Such a feature has been previously observed in Langmuir films from block copolymers.[17] It has been interpreted as the contribution to the film formation from the dehydration of the water-soluble block. In the gas phase, at 0 mN m^{-1}, the hydrophilic blocks expand freely in the aqueous phase, and occupy an area considerably larger than the coiled hydrophobic blocks exposed to the air. Once the film is compressed, the hydrophobic blocks initially do not have to adopt another conformation because they occupy less space than the hydrophilic blocks. However, upon compression, the water-soluble blocks have to undergo some reorganization, during which water is expelled from the hydrophilic part of the film. At the same time the chains start

Table 1 Molecular characteristics of the different P*n*BA-P*t*BA precursor block copolymers. The molar percentage of PAA (obtained after acidolysis) was determined by ^{1}H-NMR in MeOD or THF as well as by potentiometry after hydrolysis of the diblocks. Values obtained by potentiometry are probably underestimated because of a few percent of adsorbed water in the polymer[14]

	Mn/10^3 g mol^{-1}			PDI[c]	*t*BA (mol%)		PAA (mol%)	
	Theoretical	MALDI TOF MS[a]	SEC[b]	SEC[b]	Theoretical	^{1}H-NMR	^{1}H-NMR	Potentiometry
P*n*BA90	11.7	12.9	12.7	1.09				
P*n*BA100	12.3	12.5	15.3	1.07				
P*n*BA90-P*t*BA33	15.9	16.8	17.7	1.05	0.27	0.29	0.27	
P*n*BA90-P*t*BA100	24.3	24.7	25.6	1.07	0.52	0.54	0.50	0.47
P*n*BA100-P*t*BA150	32.0		33.7	1.04	0.60		0.56	0.57
P*n*BA90-P*t*BA300	50.4	51.4	47.2	1.07	0.77	0.78	0.78	0.71

[a] Matrix-assisted laser desorption/ionisation time-of-flight mass spectrometry. [b] Size-exclusion chromatography. [c] Polydispersity index.

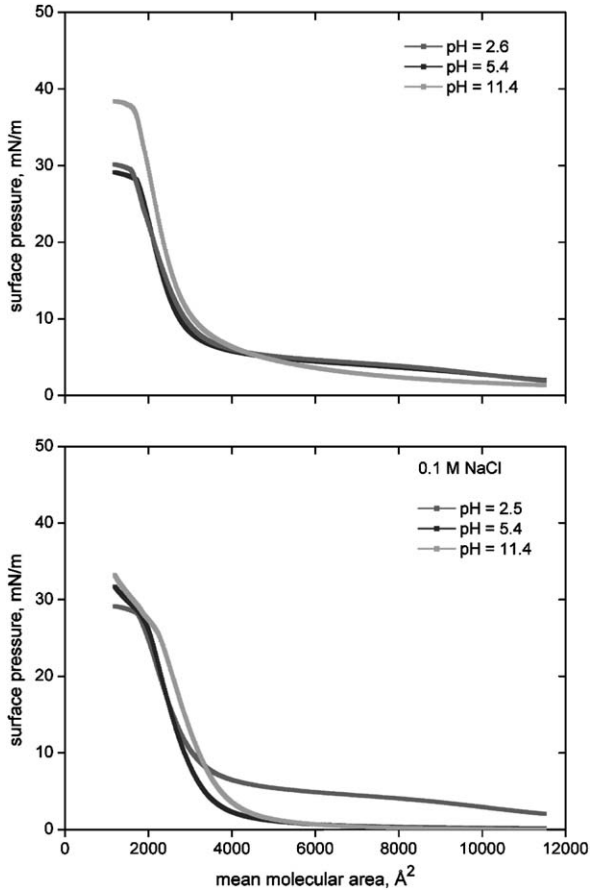

Fig. 1 Surface pressure–area isotherms of the Langmuir films from P*n*BA$_{90}$-PAA$_{300}$. Effect of pH and ionic strength: (top) without salt, (bottom) with added salt.

experiencing hydrophobic interactions, which is reflected by the small surface pressure. The lift-off area, in turn, corresponds to the packing of hydrophobic chains.

Fig. 1 also shows that the pH only has a minor effect on the film behavior. The only deviation is observed for films at high pH values (11.4) on the subphase without added salt, for which the collapse pressure is at *ca.* 37 mN m^{-1}. This is considerably higher than the 27 to 30 mN m^{-1} observed for the films studied at lower pH. Only at pH 11.4 is the PAA block fully deprotonated. In the absence of added salt, strong electrostatic interactions between the ionized acrylate and Na^+ are expected. Such interactions were in fact observed before by SANS (small-angle neutron scattering) and dynamic light scattering experiments.[13] Similarly to small water-insoluble amphiphiles such as fatty acids[56,57] this effect should lead to Langmuir film stabilization and increased values for collapse pressure, as discussed below. Since only monovalent cations are present in the subphase no metal ion coordination is expected and therefore no changes in the mean molecular area are observed.

The presence of salt (NaCl) hardly influences the film behavior. The lift-off areas and collapse pressures remain comparable to the curves obtained on salt-free subphases. The only difference is the lower collapse pressure at pH 11.4, where the PAA units are fully ionized, and the decrease of surface pressure at large molecular areas. NaCl present in the subphase has a charge screening effect, which explains the lower collapse pressure at high pH. Again, in SANS and DLS, the screening of

charges is clearly observed.[13] In the Langmuir film, it would indeed be expected that the salt addition decreases the electrostatic repulsion between the PAA chains and causes the pressure to drop.

We need to stress here that the curves at pH 5.4 with and without salt are not directly comparable. The degree of ionization of the acrylic acid monomer units is strongly affected by the ionic strength. Because of this, the PAA chains are not ionized to the same degree at the same pH—their degree of ionization is higher at a higher ionic strength. Salt addition triggers two opposite phenomena: the amount of ionized acrylic acid monomer units increases and the repulsive interactions decrease; the latter should be the prevailing effect.

If these effects are considered, the surface pressure decrease in the presence of salt at high pH can be explained. Assuming high ionization degrees and charge screening at the same time, the energy needed to organize the PAA blocks is considerably smaller. In this case there is no need to rearrange or break hydrogen bonds between PAA units and water molecules or between two or more PAA units and the repulsion between the ionized PAA blocks does not prohibit the packing any more. The energetic contribution from water removal from that part of the film is also smaller due to the presence of the salt. Altogether, less force is required to produce the same self-assembled architecture at high pH and in the presence of salt than without salt and/or at low pH.

Fig. 2 shows that polymers with shorter hydrophilic blocks and the same size of the hydrophobic part were also analyzed in terms of their film-forming properties. Overall, their behavior is identical to P*n*BA$_{90}$-PAA$_{300}$. In particular, the film behavior is controlled by the size of the hydrophobic block, and film stability and collapse pressure are essentially the same.

Polymer monolayers spread on calcium containing subphases behave essentially as they do on pure water subphases. The only difference is a shift in the lift-off areas to smaller values (2500 Å^2). This is typical for carboxylate monolayers on subphases containing divalent cations and results from complex formation between the carboxylates and the cations. Also, the monolayer rigidity is higher but still within the fluid regime.

Monolayer visualization was performed with Brewster angle microscopy (BAM, image size 220 × 274 μm), Fig. 3. For pure subphases (both pure water and the

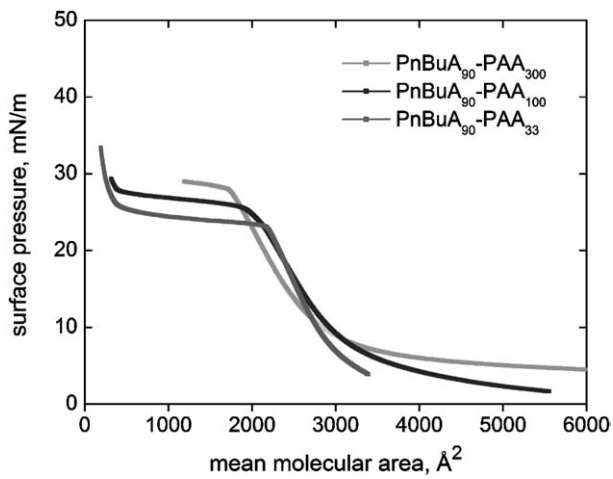

Fig. 2 Surface pressure–area isotherms of P*n*BA-PAA block copolymers at the air–water interface. The isotherms were corrected for the number of hydrophobic units. We observe that the molecular area does not depend on the size of the PAA chain, but is controlled by the P*n*BA (hydrophobic) block.

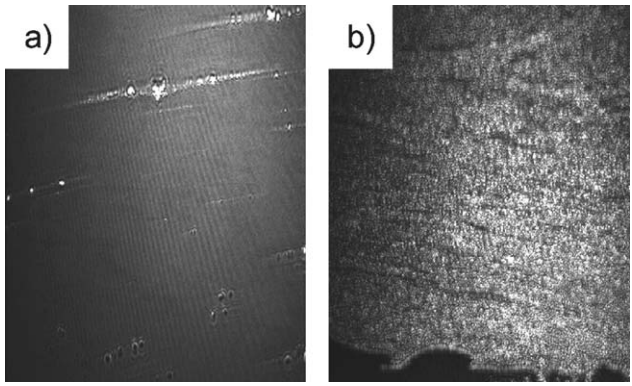

Fig. 3 BAM images of (a) the P*n*BA$_{90}$-PAA$_{300}$ monolayer at 22 mN m^{-1} on a Ca-containing subphase and (b) the polymer film after 12 h of mineralization on a subphase with pH 7 buffered with TRIS buffer, 2 mM of calcium nitrate and phosphate solution, and a surface pressure of 22 mN m^{-1}. Image size is 220 × 274 μm. Bright streaks in panel (a) are from impurities.

Ca-containing solution) as well as for the polymer monolayer on those subphases we do not observe any features. The polymer film is homogeneous throughout the compression, similar to other block copolymer monolayers studied before.[20] Right after phosphate addition to the calcium-containing subphase, no changes are observed. After *ca.* 12 h, the monolayer texture changes and bright speckles appear and form larger patches with higher reflectivity. We are not able to resolve individual CaP particles with the BAM, as the microscope's resolution is *ca.* 1 μm. However, we can see thickness fluctuations as demonstrated by the images becoming more "rough" compared to the subphase or the non-mineralized polymer film.

2. Mineralization with calcium phosphate

For mineralization, polymer films were prepared on a Langmuir–Blodgett (LB) trough and maintained at a constant surface pressure of 22 and 33 mN m^{-1}. Several mineralization procedures were employed for film mineralization: (i) the film was spread on supersaturated solutions of calcium nitrate and monobasic potassium hydrogenphosphate, similar to a procedure used by DiMasi and colleagues.[39] (ii) The film was spread on a 10 mM calcium nitrate subphase. After spreading and compression of the pure polymer film to the desired surface pressure, 5 mL of a 0.5 M potassium hydrogenphosphate solution was injected using a Hamilton syringe. This gave a final concentration of 10 mM of both calcium and phosphate in the subphase. (iii) Mineralization was performed as described in (ii), but at a final calcium and phosphate concentration of 2 mM instead of 10 mM. Finally, (iv) we have also studied the effect of pH on mineralization using procedure (ii). Here, subphases with a final concentration of 2 mM were studied at pH 5, 6, 7, 8, 9, 10 and 11. Of these procedures, approach (i) gives a complex and not always reproducible mixture of mineralized films that could not be analyzed. These experiments will therefore not be discussed further.

Mineralization with procedure (iii) (2 mM) at different pH values. The first evidence for mineralization of the polymer film is an increasing white shade appearing at the surface after *ca.* 12 h of mineralization at a subphase pH of 5, 6 and 7. At pH 9 and higher, the films have already turned white after *ca.* one hour. Attempts to compress the films during or after mineralization by moving the barriers of the LB trough show qualitative differences between the different pH values. Films mineralized at pH 5 become stiffer than the original polymer film but do retain some elasticity.

That is, they can be (very slightly) reversibly expanded and compressed even after mineralization. Mineralization at pH 7 results in a similar behavior. Mineralization at pH 9, however, results in stiff films that cannot be compressed or expanded without breaking the film and forming macroscopic cracks. In all cases, the Wilhelmy plate of the LB trough gives no significant data upon mineralization, as it is also (at least partially) immobilized in the mineralized polymer film.

Films mineralized at low pH are still somewhat transparent with macroscopic white streaks and patches. They are also macroscopically still somewhat flexible and tend to roll up on picking them up from the air–water interface. In contrast, the films mineralized at pH 9 are strongly opaque to bright white films, which tend to break during pickup from the trough.

Fig. 4 shows an optical microscopy image of a sample grown at pH 9. Optical microscopy clearly shows that a rigid material, which breaks into millimeter-sized pieces, forms once the mineralization process has proceeded to a certain level. The sample is characterized by features inherent to solid-state (rigid with cracks) rather than viscoelastic behavior, which would be indicative of a purely polymeric film. Polarization microscopy does not detect any birefringence (other than from a few particles picked up from the subphase). We therefore conclude that the CaP in the film is either amorphous CaP or that the particles are so small that no birefringence can be observed.

Fig. 5 shows further evidence for mineralization of the polymer monolayers. Energy-dispersive X-ray spectroscopy (EDXS) and infrared (IR) spectroscopy confirm the presence of CaP in the films. EDXS detects intense Ca and P signals. The estimated atomic ratio of Ca to P is 1.8. This could indicate that amorphous CaP (ACP) and an excess of Ca^{2+}, which is coordinated to the polymer, coexist in the films. Alternatively, the Ca : P ratio is close to 1.67, which is the ratio found in hydroxyapatite (HAP).[44] EDXS could therefore also suggest the presence of HAP.

IR spectra of the pure polymer show a broad band between *ca.* 2800 and 3500 cm^{-1}, which is assigned to the carboxylic acid moieties and some residual water in the polymers. A further strong band at 1700 cm^{-1} is indicative of carboxylic acid dimers, which is consistent with the absence of metal ions in the polymer.[58,59] IR spectroscopy of mineralized films detects a much weaker band at 1700 cm^{-1}. However, there is no band at 1750 cm^{-1}, which would be indicative of calcium coordinated to the acid groups of the polymer.[60] Furthermore, IR of the mineralized films shows a strong band at 1000 cm^{-1} that is assigned to the P–O vibration of the phosphate

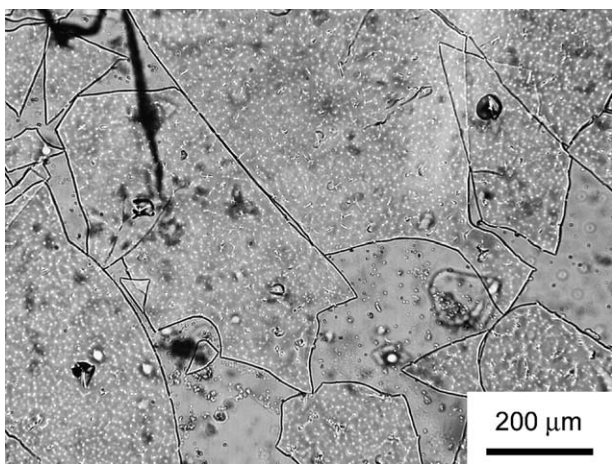

Fig. 4 Optical micrograph (bright field) of a film mineralized at pH 9 and 2 mM of calcium and phosphate after 12 h of mineralization.

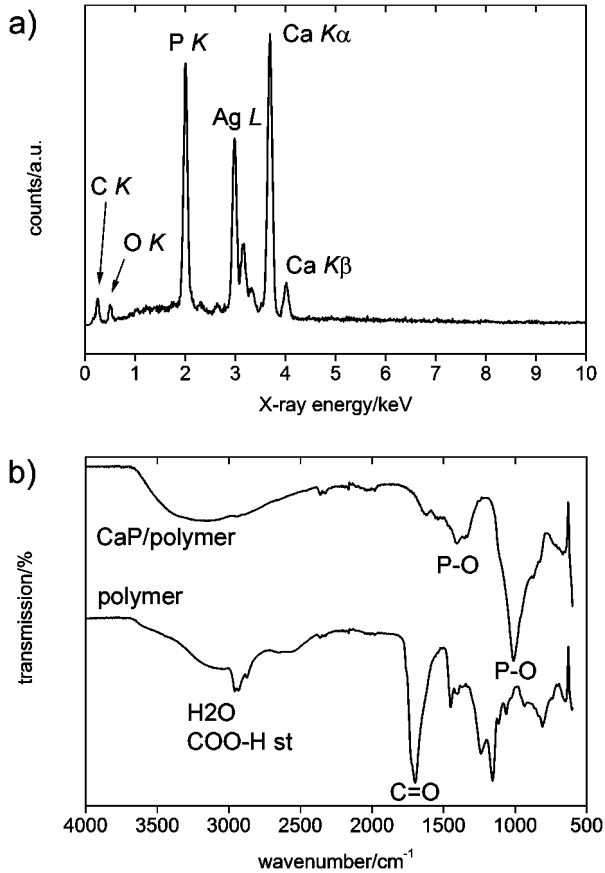

Fig. 5 (a) EDXS spectrum of a film obtained at pH 8 from a 2 mM solution. The three Ag L signals are Ag Lα1, Ag Lα2, and Lβ1 peaks. (b) ATR-IR (attenuated total reflectance infrared spectroscopy) spectrum of the pure polymer and a film mineralized at pH 8 from a 2 mM solution after 12 h.

anion. A further band at 1300 cm^{-1} can also be assigned to the phosphate anion. The fact that the IR spectra of the mineralized films still show the signals from the polymer, although weaker, clearly shows that the films studied here are composite polymer–inorganic films that could indeed be regarded as models for biomineral films.

Overall, IR and EDXS provide evidence for the formation of calcium phosphate, most likely HAP, beneath the polymer monolayers. X-Ray diffraction and electron diffraction are not possible due to the low amount of material obtained per experiment and the electron beam sensitivity of the hybrid films respectively. As a result, a further conclusion with regard to the crystal phase of the precipitate cannot be drawn at the moment. It is, however, realistic that after 12 h the film consists of HAP particles, similar to an earlier example where HAP spheres have been obtained in the presence of double-hydrophilic block copolymers.[55] In particular the absence of a Ca–COO band at 1750 cm^{-1} in IR and a Ca : P ratio close to that of HAP support this interpretation.

Fig. 6 shows representative electron microscopy images of the mineralized films. Scanning (SEM) and transmission (TEM) electron microscopy reveal that the pH of the subphase has a dramatic influence on the morphology of the mineralized films. Mineralization from 2 mM calcium and phosphate solutions at pH 5 yields films containing spherical particles with diameters of 7 ± 2 nm. The particles are not in

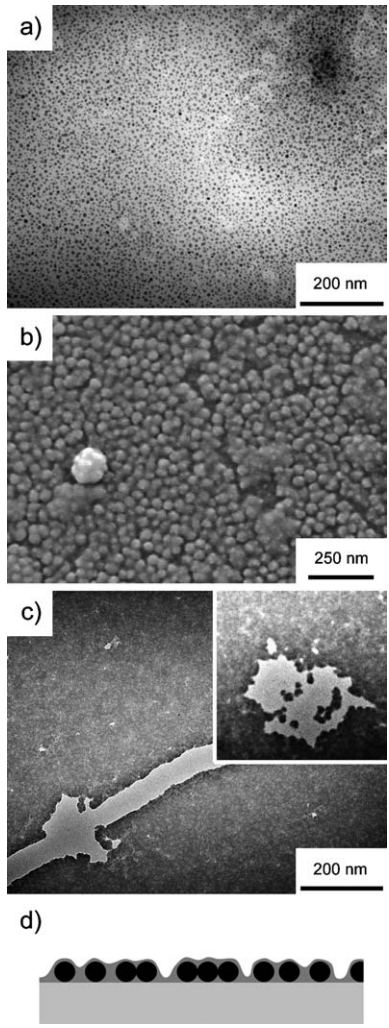

Fig. 6 TEM (a, c) and SEM (b) images of films mineralized from 2 mM solutions of calcium and phosphate after 12 h. (a) pH 5, (b) pH 7, (c) pH 9. Inset in panel (c) is a higher magnification image of the same sample. Panel (d) illustrates the "blanket on particles" morphology. Light gray—TEM or SEM substrate; dark gray—polymer film; black—CaP particles.

close contact. On the contrary, there are gaps between individual particles, although some particles aggregate into poorly-ordered 2D hexagonal lattices.

Similarly to the films grown at pH 5, films grown from 2 mM solutions at pH 7 also consist of spherical particles with a diameter of 34 $\pm$ 2 nm (from TEM) or 41 $\pm$ 1 nm (from SEM). SEM shows that the particles are arranged either in a close-contact monolayer or are bound in "raspberry-like", slightly larger aggregates. TEM shows that the particles are not in close contact. We explain the difference of the particle sizes determined from SEM and TEM, and the smaller particle-to-particle distances observed in the SEM, with a "blanket-on-particles" structure. The CaP particles have a diameter of *ca.* 34 nm. However, they are covered by a *ca.* 4.5 nm thick, soft and flexible polymer film. Upon transfer of the film to a solid substrate, the polymer film follows the contours of the CaP particles on the substrate. Therefore, the particles observed in the SEM appear larger and in closer contact than the particles seen in the TEM.

Films grown from 2 mM solutions of calcium nitrate and potassium phosphate at pH 9 are, in contrast to the films grown at lower pH, dense and only exhibit a few macroscopic cracks. Higher-magnification TEM shows that the films are composed of small particles with a diameter of 44 ± 6 nm.

SEM and TEM therefore provide an explanation for the residual elasticity of the hybrid films fabricated at low pH. At low pH, the polymer films are being mineralized but there is enough space (that is, polymer) between individual particles or smaller domains that some regions can still move when the films are compressed or expanded. On the other hand, a film like the one shown in Fig. 5c is too stiff to respond to an external mechanical stimulus other than by breaking or cracking.

As a result, Fig. 6 clearly shows that the pH of a solution has a dramatic influence on the structure (and thus the physical properties) of a polymer–inorganic hybrid film. As the solution pH also controls the crystal-phase selection during mineralization,[34,44] it would be interesting to determine the crystal structure of the CaP obtained under these different conditions. Unfortunately, such small amounts are not amenable to regular X-ray analysis, and IR spectroscopy (see above) only gives qualitative results.

Fig. 7 shows the development of the diameter of the particles grown under the polymer monolayers. At low pH, rather small particles form after 12 h. The largest particle diameter is observed at pH 8. At higher pH values, the diameters decrease again to *ca.* 35 nm. The particles have a relatively uniform diameter, which suggests that their nucleation and growth is a well-controlled process.

Samples grown at pH 6 also contain small fibers similar to CaP fibers observed by Peytcheva *et al.*[61] These fibers have a uniform diameter of *ca.* 12 nm, but the coexistence of both particles and fibers suggests that not in all cases is a single morphology energetically favored. For example, it has been suggested that the fibers observed by Peytcheva *et al.* are kinetic intermediates.[61] It is thus possible that here at pH 6 there is a transition from one regime (*e.g.* one crystal phase) to another and the fibers are part of this transition. That is, it is conceivable that at low pH one crystal phase, *e.g.* brushite, forms and at higher pH HAP is the favored crystal phase. At pH 6, both crystal phases could be present and their different solubilities, stabilities and growth processes could lead to (possibly metastable) fiber morphologies.

Fig. 8 shows that under certain conditions (pH 10, 2 mM, slow stirring) films with an almost crystalline order form. The individual particles have a narrow size

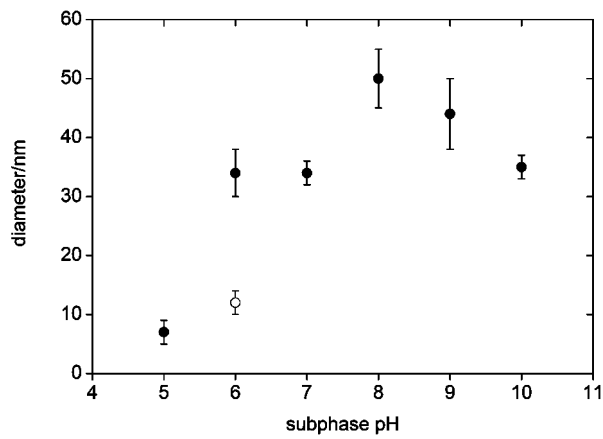

Fig. 7 Mean diameter of the spherical CaP particles *vs.* the subphase pH. Below pH 5 no precipitation is observed and above pH 10 calcium hydroxide precipitates along with CaP, which makes an analysis difficult. Solid symbols are diameters of the spherical particles. Open symbol is the diameter of the fibers observed at pH 6.

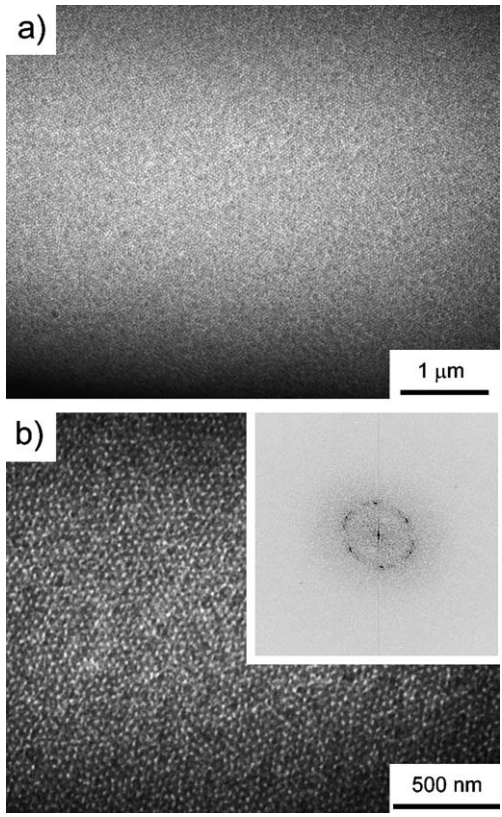

Fig. 8 TEM bright-field images of a film mineralized at pH 10 and 2 mM. (a) Low magnification and (b) high magnification image. Inset in (b) is the corresponding Fourier transform.

distribution and are arranged in a distorted hexagonal lattice, as can be seen from the corresponding Fourier transform. This is interesting, because it demonstrates that even a rather flexible matrix like a polymer film at the air–water interface does not only lead to uniform particles with identical particle sizes. The film also acts as a tool for the 2D arrangement of the resulting particles in a near-crystalline order. The implication for biomineralization is that even rather flexible scaffolds swollen with water are able to regulate mineralization on the atomic (crystal phase), the nanoscopic (particle size and shape), and the sub-micron to micron (2D arrangement) level of the precipitate.

Fig. 9 shows atomic force microscopy (AFM) data on mineralized films. AFM confirms TEM in that it shows that the films are smooth and do not exhibit large thickness variations. The largest particles are observed at pH 8; at higher and lower pH values of the subphase the particles are smaller. These sizes are consistent with sizes extracted from TEM images and confirm the formation of uniformly mineralized CaP/polymer hybrid films. AFM also reveals that there is no incorporation of large crystals. This finding supports the notation of a homogeneous nucleation and growth process over the whole film and during the entire growth process.

Time-resolved mineralization of the films. Fig. 10 shows representative TEM images of a film grown from a 2 mM solution at pH 9 at different reaction times. TEM clearly shows that film formation is a rather complex process where, initially, small spherical particles appear to form under the film. These particles then undergo further growth into larger, uniform patches, and finally a dense film is obtained. The

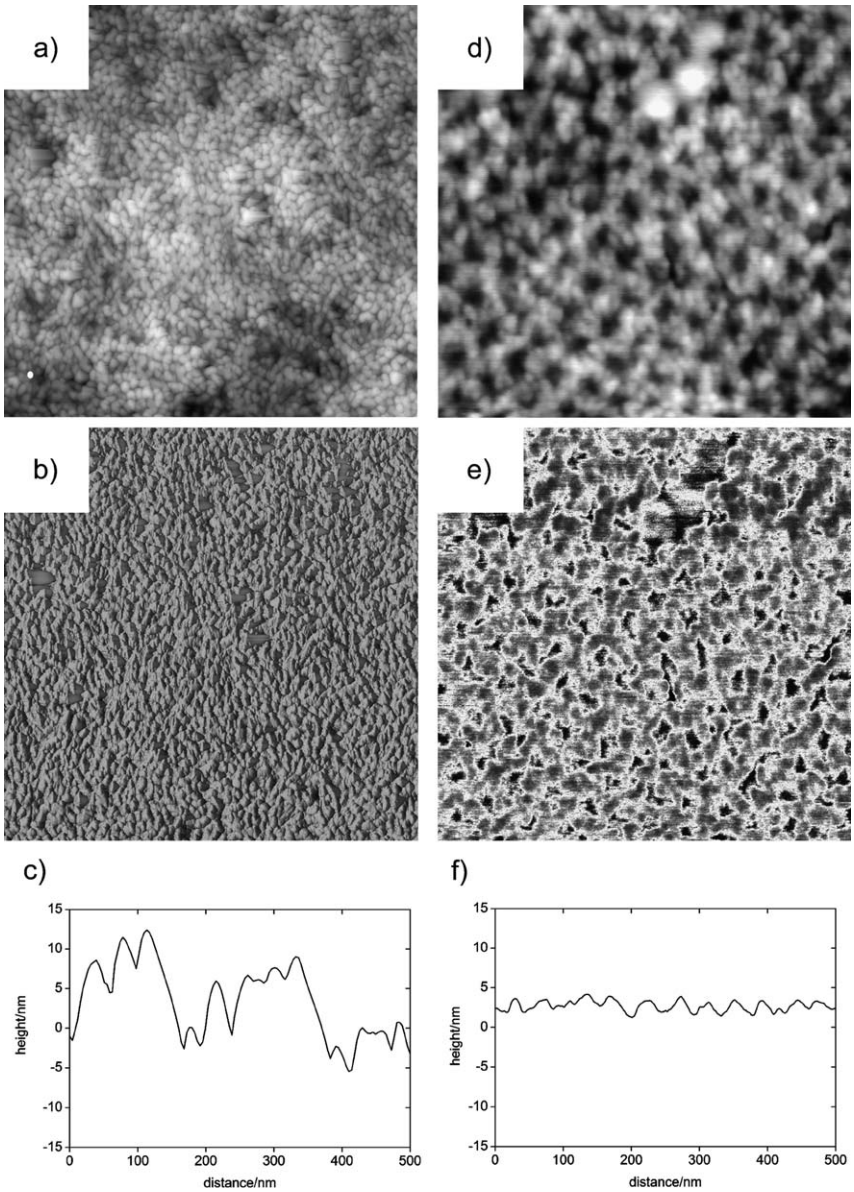

Fig. 9 AFM data of mineralized films. (a, b, c) Film mineralized at pH 8. (a) Topography, (b) phase image, and (c) representative height profile. (d, e, f) Film mineralized at pH 10. (d) Topography, (e) phase image, (f) representative height profile. Panels (c, f) are on the same scale and clearly show that the films obtained at pH 10 are smoother than films obtained at pH 8.

resulting film only has a few defects (very small holes) along with large cracks that are due to the mechanical stress from either drying or transfer onto the TEM grid.

Effect of stirring. Fig. 11 shows that not only the pH of the subphase, but also agitation of the solution (stirring) is a crucial parameter for mineralization control. All samples shown so far were grown from subphases with gentle stirring. Fig. 11 shows that films mineralized from subphases without stirring are much less homogeneous

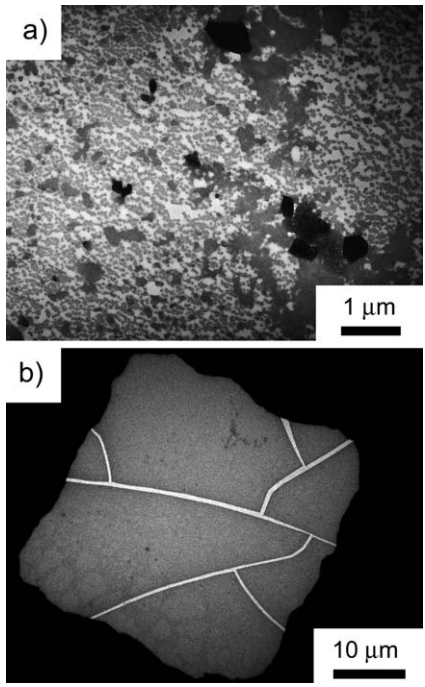

Fig. 10 TEM images of films mineralized at 2 mM. (a) Film obtained after 1 h. (b) Film obtained after 12 h. A higher magnification image of the same film is shown in Fig. 5c.

and contain large crystals, small spherical features and micrometer-long fibers that are only a few nanometers in diameter.

The fibers resemble the CaP fibers reported earlier by Peytcheva *et al.*[61] These authors have shown that another poly(carboxylate), poly(aspartate), is an efficient growth modifier for CaP from bulk solution. The fibers were reported to form extended structures, where individual fibers connect areas with higher mineral density through areas where less inorganic material is located. Overall the respective samples have a "fluffy" morphology and are composed of many CaP (possibly CaP–polymer) wires with a diameter of a few nanometers. More precisely, the fiber structure was identified as elongated hydroxyapatite (HAP) with a favored growth direction along the HAP *c*-axis. The formation of these unique wires was explained by adsorption of poly(aspartic acid) on all but the (001) faces, which are the only ones not exhibiting calcium ions at the surface. At the time, the fibers were assigned to kinetic intermediates. A similar mechanism can be postulated here, but will have to be confirmed by more detailed kinetic and structural analysis.

The large crystals that are also observed under films grown without stirring could have grown in solution and then have been attached to the film at some point during the mineralization process. However, Volkmer and coworkers have shown that the charge of a Langmuir film has a strong influence on the mineralization of calcium carbonate beneath the film.[42] This suggests that large crystals could also grow directly from the film in the current case. This assumption is further supported by the observation that one end of the large crystal shown in Fig. 10a has rather well-developed edges, whereas the other end appears to be "cut" and sitting in the film. This is again similar to the observations by Volkmer and Fricke, who have shown that Langmuir films are able to select certain crystal orientations of particles growing from the film.[62] They have shown that specific crystal overgrowth does not require geometrical and stereochemical complementarity with the templating agent.

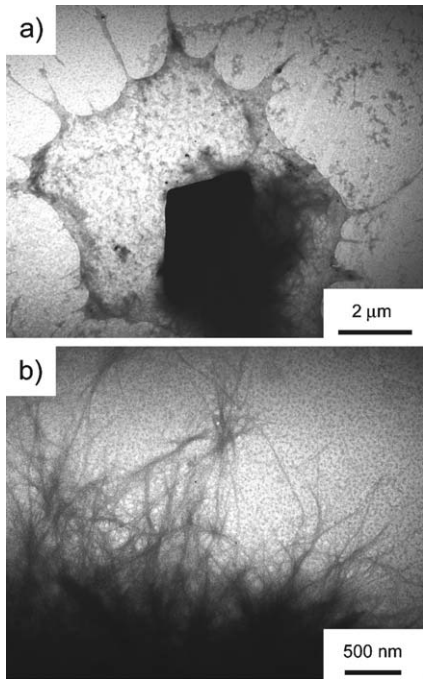

Fig. 11 TEM images of a film mineralized at pH 5 from 2 mM solution without stirring the subphase. (a) Low-magnification image showing a large crystal and the surrounding material. (b) Higher-magnification image showing the small particles and thin fibers.

For example, in calcium carbonate non-directional electrostatics such as the average charge density or the mean dipole moment are sufficient to generate an oriented growth. In the current case, lattice matching of the polymer with calcium phosphate would require specific molecules with a defined and probably rather stiff architecture. However, as in the present system the polymer chains are relatively highly charged and flexible, lattice matching (that is, epitaxial or quasi-epitaxial interactions between the monolayer and the CaP) are rather unlikely. This therefore indicates that charges and the flexibility of the polymer chain are the main reasons for the formation of the resulting spherical primary particles.

Mineralization at higher concentrations (procedure (ii), 10 mM). Fig. 12 shows representative TEM images of films grown at higher calcium and phosphate concentrations. TEM clearly demonstrates that the concentration of the precursor salts in the subphase is a further parameter to control the properties of the final film. We have shown above that at pH 9 and a calcium and phosphate concentration of 2 mM, uniform thin and almost defect-free films are obtained after 12 hours of mineralization. Fig. 12 shows that higher calcium and phosphate concentrations (10 mM) accelerate growth under the films.

With 10 mM subphases, the films are densely mineralized already after one hour. They have a uniform thickness, which can be deduced from the uniform gray level of the TEM images. They appear to be less dense than the films obtained after 12 h at 2 mM and pH 9 (Fig. 6, 8, 9 and 10) because there are light spots surrounded by dark "wires", which make up the film. This suggests that a higher concentration of the precursor salts in the subphase (i) accelerates the growth of the inorganic film, but (ii) also leads to somewhat different film morphologies, where tiny pores appear to be present.

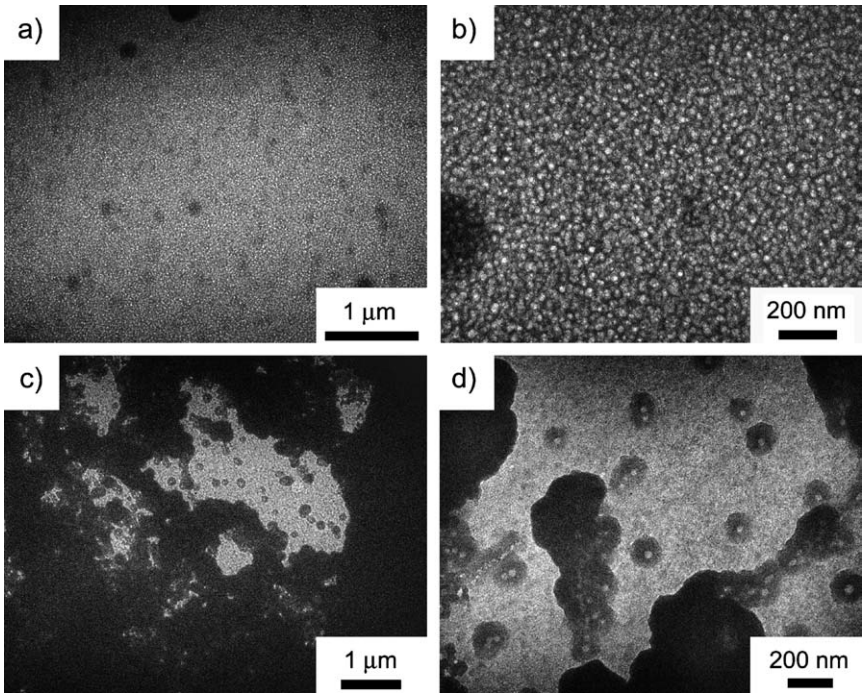

Fig. 12 TEM images films mineralized at pH 9 with 10 mM calcium and phosphate solutions. (a, b) Film obtained after 1 h. (c, d) Film obtained after 12 h.

Unlike films grown at lower concentrations, films grown at 10 mM of calcium and phosphate, adopt rather uncontrolled and rough morphologies after extended growth times. Films obtained after 12 h contain regions with thick and thin crystal layers along with large, approximately spherical features that appear to have a region of lower density in the center. We assign this less uniform structure to further growth *via* heterogeneous nucleation on the existing film. These data therefore clearly show that low concentrations or short reaction times are the key parameters for the growth of films with a uniform morphology and thickness.

This finding is interesting from a biological or biomimetic point of view because in Nature one of the key problems for the fabrication of complex biogenic hybrid materials is the spatial and temporal organization of the individual building blocks.[46,47,63–67] That is, all ions needed for growing a specific inorganic must be available in sufficient amounts at a given time and given location of an organism. Then the interfacial energies and the relative concentrations of the building blocks must be such that only the desired materials form. The current paper shows that low salt concentrations can be favorable if longer crystallization times, as they are typical for biological processes, are considered.

Conclusion

Amphiphilic poly(acrylic acid)–block–poly(*n*-butylacrylate) block copolymers form stable films at the free water surface. The films do not significantly change with pH or ionic strength. As the films are stable at different degrees of ionization and can be mineralized with calcium phosphate, they are a useful model for mimicking biological mineralization. Mineralization is best controlled at low supersaturation and at high pH values. Even a long-range order with a distorted hexagonal symmetry is

observed in some cases. The current experiments also clearly illustrate that a well-defined (but not crystalline) interface is crucial for controlling calcium phosphate mineralization.

The outcome of this study is interesting because it demonstrates that even a rather flexible matrix like our polymer film at the air–water interface leads to uniform particles with identical particle sizes. Moreover, the film also acts as a tool for the 2D arrangement of the resulting particles in a near-crystalline order. The implication for biomineralization is that even rather flexible scaffolds swollen with water are able to regulate mineralization on the atomic (crystal phase), the nanoscopic (particle size and shape) and the sub-micron to micron scale (2D arrangement) of the precipitate. As a result, the current study could serve as a model for biological mineralization, which is more closely related to nature than films made from *e.g.* detergents or other low molecular mass compounds.

Experimental

Langmuir monolayers and Brewster angle microscopy

Aliquots of 50 to 200 μL of block copolymer solution (1 mg mL^{-1}) in $CHCl_3$–EtOH (90 : 10 v/v), spectroscopy grade solvents, were spread by a Hamilton syringe on bi-distilled water or aqueous 0.1 M NaCl of pH 2.5, 5.4 and 11.4 (adjusted by HCl or NaOH respectively), held in a mini Langmuir–Blodgett trough (total area 242 cm^2) from KSV, Finland, placed on an anti-vibration table in a dust-free room. After spreading, 5 min were allowed for the solvent to evaporate, followed by compression of the film at 10 mm per min. The surface pressure of the monolayers was measured to $\pm$ 0.1 mN m^{-1} with a Wilhelmy plate (chromatography paper, ashless Whatman Chr 1) connected to an electrobalance. Monolayers were compressed at 20 °C.

Monolayer morphology was visualized with a BAM2plus Brewster angle microscope (Nanofilm, Germany), with a 50 mW laser at the wavelength of 532 nm. With a 20 × Nikon long-distance objective lens, the microscope has a resolution of 1 μm; recorded images correspond to 220 μm in width.

Mineralization

After the polymer monolayer was spread on Ca-containing subphase (pH 11.4) up to a desired surface pressure, phosphate solution was added to the bulk and *ca.* 12 h were allowed for the film to mineralize. The solutions were buffered with acetic acid (pK_a 4.8, pH 5), piperazine (pK_a 5.7, pH 6), ADA (pK_a 6.6, pH 7), TRIS (pK_a 6.6, pH 8) and boric acid (pK_a 9.24, pH 9 and 10). Calcium nitrate was added to the buffer solutions, which were then adjusted to the target pH using the necessary amount of potassium hydroxide or nitric acid. Throughout the mineralization process, the subphase was continuously stirred. For further analysis, the mineralized films were directly transferred onto TEM grids from different regions as single layers. Transfers were performed by the Langmuir–Blodgett procedure at 2 mm per min at an angle of *ca.* 60°. After deposition, TEM grids were stored in a desiccator for drying.

Microscopy

Optical microscopy was done on a Leica DM-RP microscope with magnifications between 5× and 40×. Films were picked up after mineralization with microscopy tweezers and directly transferred to microscopy slides. SEM was done on a Philips XL30 FEG ESEM operated at 10 kV. Samples were sputtered with Au or Pt prior to imaging. EDXS experiments were made with an EDAX spectrometer from 0 to 10 keV. TEM images were taken on a FEI Morgani 268D operated at 80 kV. Samples were deposited on carbon-coated copper grids and directly imaged after drying in air. AFM was done on a Molecular Imaging PicoLE System equipped with

a multi-purpose scanner. The samples were prepared by applying approximately 5 μl of sample solution onto a 2 × 2 cm glass cover slip and letting it air-dry in the dark. Images were acquired using a silicon cantilever (type-NCHR pointprobe-plus, force constant 42 N m^{-1} as given by the manufacturer for non-contact mode images or type-FM point probes, force constant ~1.2–3.5 N m^{-1} as given by the manufacturer for contact mode images; both from NanoAndMore GmbH, Wetzlar, Germany). Samples were imaged directly after drying and after various irradiation times using both contact and non-contact modes.

IR spectroscopy

Infrared spectra were obtained from the neat samples on a Shimadzu FTIR 8300 with a Golden Gate ATR unit. Spectra were recorded from 300 to 4500 cm^{-1} with a resolution of 4 cm^{-1}.

Acknowledgements

We thank R. Grüter and S. Erni (University of Basel) for help with the mineralization experiments, the Swiss National Science Foundation, the NCCR Nanosciences, the EU-RTN PolyAmphi, the MPI of Colloids and Interfaces and the University of Potsdam for financial support. A. T. thanks the Holcim Stiftung Wissen for a Habilitation Fellowship.

References

1 I. W. Hamley, *The Physics of Block Copolymers*, Oxford University Press, Oxford, 1998.
2 J. M. G. Cowie and V. Arrighi, *Polymers: Chemistry and Physics of Modern Materials*, CRC Press, 2007.
3 G. Riess, *Prog. Polym. Sci.*, 2003, **28**, 1107.
4 S. Förster, V. Abetz and A. H. E. Müller, *Adv. Polym. Sci.*, 2004, **166**, 173.
5 M. Sauer, T. Haefele, A. Graff, C. Nardin and W. Meier, *Chem. Commun.*, 2001, 2452.
6 C. Nardin and W. Meier, *Rev. Mol. Biotechnol.*, 2002, **90**, 17.
7 A. Graff, M. Sauer, P. Van Gelder and W. Meier, *Proc. Natl. Acad. Sci. U. S. A.*, 2002, **99**, 5064.
8 R. Stoenescu and W. Meier, *Mol. Cryst. Liq. Cryst.*, 2004, **417**, 185.
9 E. G. Bellomo, M. D. Wyrsta, L. Pakstis, D. Pochan and T. J. Deming, *Nat. Mater.*, 2004, **3**, 244.
10 H. Schlaad, H. Kukula, J. Rudloff and I. Below, *Macromolecules*, 2001, **34**, 4302.
11 H. Kukula, H. Schlaad, M. Antonietti and S. Förster, *J. Am. Chem. Soc.*, 2002, **124**, 1658.
12 F. Checot, S. Lecommandoux, Y. Gnanou and H. A. Klok, *Angew. Chem., Int. Ed.*, 2002, **41**, 1339.
13 O. Colombani, M. Ruppel, M. Burkhardt, M. Drechsler, M. Schumacher, M. Gradzielski, R. Schweins and A. H. E. Mueller, *Macromolecules*, 2007, **30**, 4351.
14 O. Colombani, M. Ruppel, F. Schubert, H. Zettl, D. V. Pergushov and A. H. E. Mueller, *Macromolecules*, 2007, **40**, 4338.
15 E. Eghbali, O. Colombani, M. Drechsler, A. H. E. Mueller and H. Hoffmann, *Langmuir*, 2006, **22**, 4766.
16 B. Rippner, K. Boschkova, P. M. Claesson and T. Arnebrant, *Langmuir*, 2002, **18**, 5213.
17 A. Wesemann, H. Ahrens, R. Steitz, S. Foerster and C. A. Helm, *Langmuir*, 2003, **19**, 709.
18 R. B. Cheyne and M. G. Moffitt, *Langmuir*, 2006, **22**, 8387.
19 T. J. Joncheray, K. M. Denoncourt, M. A. R. Meier, U. S. Schubert and R. S. Duran, *Langmuir*, 2007, **23**, 2423.
20 T. Haefele, K. Kita-Tokarczyk and W. Meier, *Langmuir*, 2006, **22**, 1164.
21 G. L. Gaines Jr, *Langmuir*, 1991, **7**, 834.
22 M. Oner, J. Norwig, W. H. Meyer and G. Wegner, *Chem. Mater.*, 1998, **10**, 460.
23 H. Colfen and M. Antonietti, *Langmuir*, 1998, **14**, 582.
24 H. Colfen and L. Qi, *Chem.–Eur. J.*, 2000, **7**, 106–116.
25 M. Sedlak and H. Cölfen, *Macromol. Chem. Phys.*, 2001, **202**, 587.
26 H. Colfen, *Macromol. Rapid Commun.*, 2001, **22**, 587.
27 A. N. Kulak, P. Iddon, Y. Li, S. P. Armes, H. Colfen, O. Paris, R. O. Wilson and F. C. Meldrum, *J. Am. Chem. Soc.*, 2007, **129**, 3736.

28 G. Wegner, P. Baum, M. Muller, J. Norwig and K. Landfester, *Macromol. Symp.*, 2001, **175**, 349.
29 K. Gorna, R. Munoz-Espi, F. Grohn and G. Wegner, *Macromol. Biosci.*, 2007, **7**, 163.
30 A. Taubert, C. Kübel and D. C. Martin, *J. Phys. Chem. B*, 2003, **107**, 2660.
31 A. Taubert and G. Wegner, *J. Mater. Chem.*, 2002, **12**, 805.
32 A. Taubert, D. Palms, O. Weiss, M.-T. Piccini and D. N. Batchelder, *Chem. Mater.*, 2002, **14**, 2594.
33 A. Taubert, D. Palms and G. Glasser, *Langmuir*, 2002, **18**, 4488.
34 S. Schweizer and A. Taubert, *Macromol. Biosci.*, 2007, **7**, 1085.
35 S.-H. Yu and H. Colfen, *J. Mater. Chem.*, 2004, **14**, 2124.
36 J. H. Fendler, *Supramol. Chem.*, 1995, **6**, 209.
37 J. H. Fendler, *Curr. Opin. Solid State Mater. Sci.*, 1997, **2**, 365.
38 F. C. Meldrum, N. A. Kotov and J. H. Fendler, *Chem. Mater.*, 1995, **7**, 1112.
39 E. DiMasi, V. M. Patel, M. Sivakumar, M. J. Olszta, Y. P. Yang and L. B. Gower, *Langmuir*, 2002, **18**, 8902.
40 D. Volkmer, M. Fricke, T. Huber and N. Sewald, *Chem. Commun.*, 2004, 1872.
41 D. Volkmer, M. Harms, L. Gower and A. Ziegler, *Angew. Chem., Int. Ed.*, 2005, **44**, 639.
42 D. Volkmer, M. Fricke, C. Agena and J. Mattay, *J. Mater. Chem.*, 2004, **14**, 2249.
43 S. Cavalli, D. C. Popescu, E. E. Tellers, M. R. J. Vos, B. Pichon, M. Overhand, H. Rappaport, N. A. J. Sommerdijk and A. Kros, *Angew. Chem., Int. Ed.*, 2006, **45**, 739.
44 *Calcium Phosphates in Biological and Industrial Systems*, Kluwer Academic Publishers, Norwell-Dordrecht, 1998.
45 S. Mann, J. Webb and R. J. P. Williams, *Biomineralization: Chemical and Biochemical Perspectives*, VCH Publishers, Weinheim, 1989.
46 E. Bauerlein, *Biomineralization—Progress in Biology, Molecular Biology and Application*, Wiley-VCH, Weinheim, 2004.
47 S. Mann, *Biomineralization: principles and concepts in bioinorganic materials chemistry*, Oxford University Press, Oxford–New York, 2001.
48 M. Bohner, U. Gbureck and J. E. Barralet, *Biomaterials*, 2005, **26**, 6423.
49 M. Bohner, *Injury*, 2000, **31**, 37.
50 L.-J. Zhang, H.-G. Liu, X.-S. Feng, R.-J. Zhang, L. Zhang, Y.-D. Mu, J.-C. Hao, D.-J. Qian and Y.-F. Lou, *Langmuir*, 2004, **20**, 2243.
51 E. D. Spoerke and S. I. Stupp, *Biomaterials*, 2005, **26**, 5120.
52 P. A. Ngankam, P. Lavalle, J. C. Voegel, L. Szyk, G. Decher, P. Schaaf and F. J. G. Cuisinier, *J. Am. Chem. Soc.*, 2000, **122**, 8998.
53 V. Ball, M. Michel, F. Boulmedais, J. Hemmerle, Y. Haikel, P. Schaaf and J. C. Voegel, *Cryst. Growth Des.*, 2006, **6**, 327.
54 M. Michel, Y. Arntz, G. Fleith, J. Toquant, Y. Haikel, J.-C. Voegel, P. Schaaf and V. Ball, *Langmuir*, 2006, **22**, 2358.
55 A. Taubert, E. Furrer and W. Meier, *Chem. Commun.*, 2004, 2170.
56 L. V. N. Avila, S. M. Saraiva and J. F. Oliveira, *Colloids Surf., A*, 1999, **154**, 209.
57 R. Johann, D. Vollhardt and H. Mohwald, *Langmuir*, 2001, **17**, 4569.
58 B. A. Brozoski, P. C. Painter and M. M. Coleman, *Macromolecules*, 1984, **17**, 1591.
59 M. M. Coleman, J.-Y. Lee and P. C. Painter, *Macromolecules*, 1990, **23**, 2339.
60 R. M. Walters, K. E. Sohn, K. I. Winey and R. J. Composto, *J. Polym. Sci., Part B: Polym. Phys.*, 2002, **41**, 2833.
61 A. Peytcheva, H. Cölfen, H. Schnablegger and M. Antonietti, *Colloid Polym. Sci.*, 2002, **280**, 218.
62 M. Fricke and D. Volkmer, *Top. Curr. Chem.*, 2007, **270**, 1.
63 L. Addadi and S. Weiner, *Nature*, 2001, **411**, 753.
64 L. Addadi and S. Weiner, *Angew. Chem., Int. Ed. Engl.*, 1992, **31**, 153.
65 L. Addadi, S. Weiner and S. Raz, *Adv. Mater.*, 2003, **15**, 959.
66 K. Simkiss and K. M. Wilbur, *Biomineralization—cell biology and mineral deposition*, Academic, San Diego, 1989.
67 R. Tang, M. Darragh, C. A. Orme, X. Guan, J. R. Hoyer and G. H. Nancollas, *Angew. Chem., Int. Ed.*, 2005, **44**, 3698.

V. Summary, conclusion and perspectives

We explored several ways of modifying the crystallization of CaP in order to generate new organic-inorganic hybrid materials.

We first demonstrate that poly(ethylene oxide)-*block*-poly(2-methyl-2-oxazoline) diblock copolymers in dilute aqueous solution can self-assemble into large aggregates despite the fact that both block segments are hydrophilic. The *cac* ranges between 1 and 5 g/L, as indicated by DLS, AUC and surface tension measurements. The aggregates observed above the *cac* are roughly spherical in shape (SLS, DLS) and exhibit an internal structure of rod-like elements or filaments (TEM). In the absence of hydrophobic interactions, aggregation of polymer chains seems to be driven by a combination of two effects. First, there is evidence for attractive interactions between PMOXA units, but neither between the PEO and PMOXA blocks, nor between PEO units (NOESY, spatial coupling). Second, a differential hydrophilic effect, as PMOXA is considerably more hydrophilic and can bind more water molecules than PEO (differential swelling). However, these structures appear to be very dynamic in nature, as they are easily disrupted by shear stress. This is probably due to the weakness of the interactions riving the assembly. For this reason, measurements on the aggregation number (SLS, viscosimetry, DOSY) were inconclusive.

However, in the conditions that we studied, this polymer lacks specific interactions or the aggregates lack mechanical resistance in order to modify the crystallization of CaP.

This makes the controlled self-assembly of double-hydrophilic block copolymers all the more fascinating and potentially useful. Temperature sensitivity triggers easy release of load when aggregates dissolve.

Now that suitable tools have been identified, it would be very interesting to vary the relative block lengths and search more stable aggregates. In particular, resistance to mechanical stress might increase gradually with the size of the PMOXA block. In parallel, PEO-PVL forms various stable structures in a controlled way: more monodisperse micelles or vesicles may be obtained through formulations involving cosolvents such as ethanol. However, this does not solve the problem caused by the neutrality of the polymer and the lack of interactions with CaP.

However, both copolymers have no effect on mineralization when compared to the control samples. The crystal phase and the shape of the primary particles are largely controlled by diffusion and pH. At basic pH, ca. 50 nm spherical HAp particles with traces of OCP form, which self-assemble into more or less porous structures. At acidic pH, ca. 100 nm flakes of DCPD and OCP form under stirring, i.e. outside the diffusion-controlled regime. They self-assemble into large porous structures, however, analysis of several samples shows that this porosity is mostly due to slight differences in

the sample mechanical history. In both cases the lack of specific interactions with either calcium or phosphate ions, amorphous CaP or HAp, is a probable explanation. Moreover, the structures built by the DHBC are too dynamic and lack the time stability to imprint any steric effect, although this difficulty can probably be overcome.

As a conclusion on the mineralization studies in solution, self-assembled structures, either stable or dynamic, coupled with high functional block polarity only, are insufficient to template crystallization, which requires a specific interaction with the crystal building blocks or crystal faces.

These results point toward using a functional block interacting more strongly i.e. adsorbing specifically on crystal faces like proteins, or simply a polyelectrolyte. In that respect, PEI is a much stronger polybase than PMOXA, therefore the polycationic PEO-PEI should constitute a more suitable polymer (even though it is no longer bis-hydrophilic in the basic neutral form, which limits its use to neutral or acidic pH). Indeed, mineralizations in presence of PEO-PEI yielded ACP-HAp beads of upper diameter 14nm,[ref Potsdam] much smaller than those obtained in control experiment without polymer or in presence of PEO-PMOXA (30-50nm). A possible mechanism for this reduced growth is the slight local lowering of pH away from the stability of HAp or simple steric reduction of diffusion around ACP germs.

In a different approach, when constraining ABCs to 2D interfaces, various conditions may be easily simulated in terms of charge surface density, supersaturation or pH, and result in various outcomes ranging from quick nucleation and growth without hierarchy to slow formation of nearly crystalline hexagonal array of uniform particles with identical particle sizes even at very long range (over 30 µm).

In more detail, amphiphilic poly(acrylic acid)–block–poly(n-butylacrylate) block copolymers form stable films at the free water surface. The films do not significantly change with pH or ionic strength. As the films are stable at different degrees of ionization and can be mineralized with CaP, they are a useful model for mimicking biological mineralization. Moreover, mineralization is best controlled at low supersaturation and at high pH values, where even a near-crystalline long-range order hexagonal symmetry is observed in some cases: the film also acts as a tool for the 2D arrangement of the resulting particles. The implication for biomineralization is that, even though even a well-defined (but not crystalline) interface is crucial for controlling CaP mineralization, rather flexible scaffolds swollen with water are able to regulate mineralization on the atomic (crystal phase), the nanoscopic (particle size and shape) and the sub-micron to micron scales (2D arrangement). As a result, the current study could serve as a model for biological mineralization, which is more closely related to nature than films made from e.g. detergents or other low molecular mass compounds. Finally, varying separately PnBuA and PAA blocks lengths could be expected to control respectively periodicity and thickness of inorganic layer and offer an interesting tool for the

tuning of surface and mechanical properties. After such tuning, a Langmuir-Blodgett transfer of the monolayer to a solid surface could offer a wide range of substrates for cell culture.

VI.Annex

A. Calcium phosphate: crystal phases

Like many other compounds, CaP crystallizes in various crystal structures with different mechanical, thermal, and chemical stabilities[10]. The most important phase in the context of bioinspired mineralization are (i) amorphous CaP (ACP), (ii) brushite (dicalcium phosphate dihydrate, DCPD, $CaHPO_4$, 2 H_2O), (iii) β-tricalcium phosphate (β-TCP, calcium orthophosphate or tribasic calcium phosphate, $Ca_3(PO_4)_2$), (iv) octacalcium phosphate (OCP, $Ca_8H_2(PO_4)_6$, 5 H_2O), and (v) hydroxyapatite (HAp, $Ca_5(PO_4)_3OH$).

In Nature, however, CaPs – especially HAp – are rarely found as neat compounds because CaPs can easily exchange PO_4^{3-}, OH^-, or Ca^{2+} for other ions. For example, Sr^{2+}, Ba^{2+}, or Pb^{2+} can replace Ca^{2+}. In addition, ions like VO_4^{3-}, AsO_4^{3-}, F^-, Cl^-, and Br^- can substitute for PO_4^{3-} and OH^- respectively. Other examples are Na^+, K^+, and CO_3^{2-}. Incorporation of the latter into HAp results in carbonated apatite (CAP), which is the main constituent of human bone. As a result, substituted apatites come in a large variety of compositions and properties, which are controlled by the chemical environment within which they were grown.

Table 5 introduces the main CaP crystal phases. Each crystal phase is characterized by its X-ray diffraction spectrum. The American Society for Testing Materials (ASTM) maintains a large database of diffraction patterns for most of the known crystalline substances. By comparison with this database it is possible to identify the CaP minerals (Table 4, Figure 26).

Table 4. ASTM references of the biologically relevant CaP crystal phases.

Phase	ASTM card
HAp	9-432
CAP	19-272
DCPD	9-77
OCP	26-1056
beta-TCP	9-169

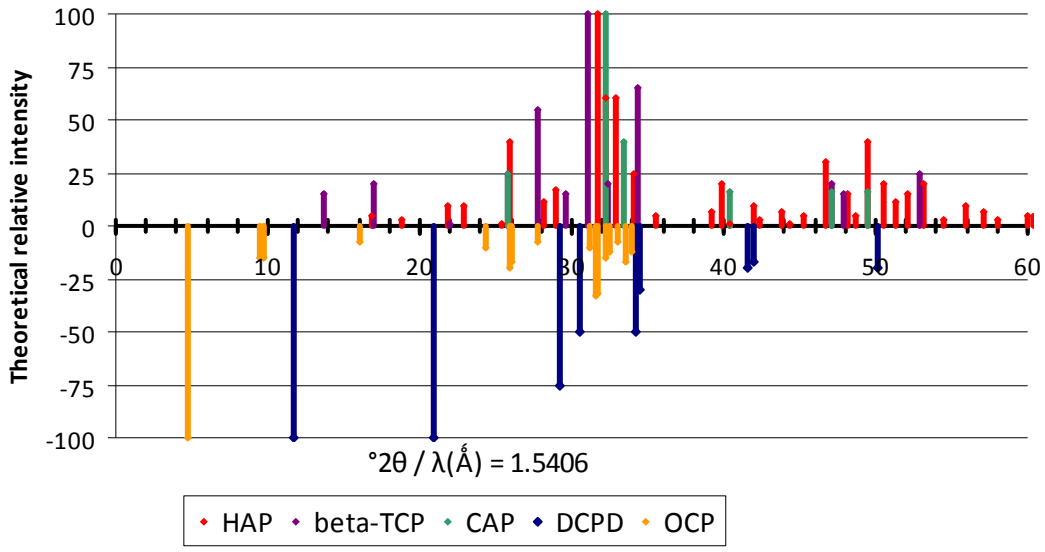

Figure 26. Theoretical spectra of biologically relevant CaP crystal phases (ASTM database). Phases formed at basic pH (up) and acidic pH (down).

Table 5 supplementary information :

[a] ACP: amorphous calcium phosphate ;
DCPD: dicalcium phosphate dihydrate;
DCPA: dicalcium phosphate anhydrous;
TCP: tricalcium phosphate;
OCP: octacalcium phosphate;
HAp: hydroxyapatite;
ClAp: Chloroapatite;
FAp: Fluoroapatite;
TTCP: tetracalcium phosphate;
OXAp: oxyapatite;
MCP: monocalcium phosphate;
MCPM: monocalcium phosphate monohydrate.

[b] Synthesis from aqueous solution at ambient conditions
[c] Large crystal face is 010.
[d] Widely used as bone substitute.
[e] Stabilized by magnesium ions.
[f] Layered structure (apatitic and hydrated layers).
[g] Major inorganic component in bone and teeth.
[h] Highly stable in acid, favored over HAp at pH < 6.
[i] Decomposition product of HAp, water-soluble.
[j] Highly water-soluble.
[k] Water-Soluble.
[l] Biological form.
[m] More stable than the biological form.
[n] High temperature synthesis.
[o] High temperature synthesis (> 500 ºC)

Table 5. Calcium phosphate crystal phases.

Common name	Chemical Formula Crystal system	RT/H2O-synthesis[b]	pH of formation	Precursor for	Typical shape	Solubility product	Ca/P ratio
ACP[a]	$Ca_3(PO_4)_2$,n H_2O (N/a)	Yes	All	All crystalline phases	Beads		1.5
DCPD[c] Brushite	$CaHPO_4$, 2 H_2O Monoclinic, C2/c	Yes	Acidic (<4-5)	HAp Monetite	Large Plates	$1.87*10^{-7}$ $(mol/l)^2$	1
DCPA Monetite	$CaHPO_4$ Triclinic, P1	Yes	Acidic (<4-5)	brushite apatite	Plates	$9.2*10^{-7}$ $(mol/l)^2$	1
α-TCP[d] Whitlockite	$Ca_3(PO_4)_2$	No[n]	Basic				1.5
β-TCP[e]	$Ca_3(PO_4)_2$	No[n]	Basic			$2.8*10^{-29}$ $(mol/l)^5$	1.5
OCP[f]	$Ca_8H_2(PO_4)_6$, $5H_2O$ Triclinic, P1	Yes	Acidic (<5-6)	HAp		$2.5*10^{-99}$ $(mol/l)^8$	1.33
HAp[g] Hydroxyapatite	$Ca_5(OH)(PO_4)_3$ Hexagonal, P63/m[l] Monoclinic[m]	Yes	Basic (>7)	OXA	Needles	$5.5*10^{-118}$ $(mol/l)^9$	1.67
ClAp Chloroapatite	$Ca_5(Cl)(PO_4)_3$ Hexagonal, P63/m	Yes	Basic (>7)		Needles		1.67
FAp[h] Fluorapatite	$Ca_5(F)(PO_4)_3$ Hexagonal, P63/m	Yes	Basic (>7)		Needles	$5.0*10^{-123}$ $(mol/l)^9$	1.67
TTCP Hilgenstockite	$Ca_4O(PO_4)_2$		Basic	HAp			2
OxAp[i]	$Ca_{10}O(PO_4)_6$	No[n]	Basic				
MCP[j]	$CaH_4(PO_4)_2$	No[o]	Acidic				0.5
MCPM[k]	$CaH_4(PO_4)_2*H_2O$		Acidic				0.5

B. Light scattering, principles, possibilities and limitations

1. Purpose

Light scattering is useful in the characterization of colloids such as polymer solution, micelles, vesicles or small crystals. Studying the scattering of a laser beam by a colloid as a function of scattering angle and concentration allows calculating shape, internal structure or solubility parameters. It is possible to either study the absolute value of the scattered intensity (static light scattering, SLS) or the relative variations in intensity caused by interferences (dynamic light scattering, DLS). These two modes yield complementary information, respectively hydrodynamic and thermodynamic properties.

2. Basic principles

Photons (electro-magnetic waves) may interact with local instant variations in refractive index (electron density) of the medium. This interaction results in an energy transfer from the photons to the electrons (fluctuations in the polarizability of the medium). Since any accelerated particle will emit light, electrons reemit photons. The reemission may happen in any direction –though it is not completely random. Overall, the absorption and reemission of a photon is called scattering. Analysis of the reemitted photon beam may reveal information about the medium itself. Lasers are the common photon source: they provide a directional, coherent (single wavelength and phase) photon beam, which makes this analysis possible –under the condition that the scattering is elastic, that is, when the excited electron returns to the ground state where it was before, the absorbed and reemitted photons have the same wavelength (energy). Inelastic light scattering happens when some electrons may return to an energy level that is in between the excited state and the ground state (Compton effect), or were before the excitation in such a level, but do return to the ground state (inverse-Compton effect). This is the object of Raman scattering and requires a different detection system.

In practice, a typical 'local variation of electron density' occurs when a visible light photon hits a solute molecule in a homogeneous solvent, therefore light scattering is adapted to the study of solutions. Primarily, two modes of analysis, called static and dynamic light scattering, deliver information about the mass, size, shape and solubility of particles from molecules (nanometer scale) to large aggregates (sub-micron scale):

In the static mode, the time-averaged scattered intensity is recorded as a function of concentration and deviation angle (ϑ, measured from the primary beam), then is extrapolated to zero

against these two parameters. Several models make the link between the intensity and the molar mass, between the concentration-dependence and the solubility (second virial coefficient), between the angle-dependence and the shape of the particles.

The dynamic mode analyses the Brownian motions taking place in the solvent. This motion generates 2 extra frequencies ± $\Delta\upsilon$ of equal intensity and width in the emission spectrum, which correspond to a positive and a negative Doppler shift and is proportional to the particle velocity. Recording the minute variations in intensity caused by the interference between the main beam and the two side beams is the base of DLS. The scattered intensity is acquired as a function of time, and then self-correlated, which yields the relaxation time of the Brownian motion and leads to the particle size via hydrodynamic models and a diffusion coefficient. In the case of a mixture of particles or polydisperse particles, further models enable to retrieve the distribution of Brownian motions.

Complementary definitions:

The **Rayleigh scattering** is the first simple model of scattering by a colloid. It assumes elastic scattering from small particles (i.e. treated as point source, $2\pi R/\lambda << 1$). The angle-independent particle scattering power makes the shape undetectable. At a typical wavelength of 632 nm, this means $R < 100$ nm.

The **Mie scattering** describes the elastic scattering by large spheres, i.e. $\lambda/2\pi << R << \lambda$ (upper limit beyond which the detected beam coherence is lost). In that case an angular scattering profile $i(\vartheta)$ is determined by the average particle shape and internal structure. Comparing the scattering profile with model form factors through angular-dependant measurements allows estimating these structure parameters, the first of which is the radius itself.

The **Momentum transfer** is the vector defined as the difference between the incident and scattered wave vectors (Equation 3). It characterizes the angle of reemission of the photons. In practice, the square of its norm (q^2) is preferred to ϑ as a measure of the detection angle because the commonly-used random-coil model for SLS expects a linear dependence of intensity with respect to $\boldsymbol{q^2}$.

$$\vec{q} = \vec{u}_{incident} - \vec{u}_{scattered} \quad \text{, where } q = \frac{4\pi \cdot n_0}{\lambda} \cdot \sin\left(\theta/2\right)$$

Equation 3. Momentum transfer, incident and scattered wave-vectors and detection angle.

3. Dynamic light scattering

a) Signal autocorrelation

The first step after recording the scattered intensity over time is forming the count rate autocorrelation function (Equation 4). Basically the signal *i(t)* is compared with itself a small time interval later. This comparison (*i(t)·i(t+τ)*) is integrated over the acquisition time (*t* from 0 to *T*) as a function of the time interval (*τ*), also called lag time, then normalized (*i(t)*^{2}). The *AC* value will be all the higher since the considered *τ* often matches with a time interval between two peaks of scattering (constructive interference).

$$AC(\tau) = \frac{\langle i(t) \cdot i(t+\tau) \rangle}{\langle i(t)^2 \rangle} = \lim_{T \to \infty} \frac{1}{T} \int_{-T/2}^{T/2} i(t) \cdot i(t+\tau) \cdot dt$$

Equation 4. Signal autocorrelation function *AC(τ)*.

A plot of *AC(τ)* typically shows:

- a plateau at value 1 (normalized) corresponding to low lag times at which the sample did not have time to move. At this time-scale it is like frozen, therefore the correlation is maximal;

- an exponential decrease, corresponding to the distribution of Brownian motions from all solutes and solvent molecules ; it is naturally this part which contains all the information;

- a second plateau at value zero, corresponding to high lag times after which every molecule seems to occupy a random position, therefore the intensity correlation is minimal.

Note: *AC(τ)* is either the intensity autocorrelation $g_2(\tau)$ or the field autocorrelation $g_1(\tau)$, linked by the Siegert relation[130].

b) Extraction of relaxation times

The second step is to extract the relaxation times from the exponential drop of the autocorrelation function. Several methods exist and each of them relies on a different model. Typical relaxation times range from 10^{-13} s for solvent molecules up to 10^{-8} s for large macromolecules. In order to obtain a statistically significant sampling of relaxation times, billions of such events must be recorded, which means in practice that correct acquisition times are of the order of several tens of seconds, typically a few minutes.

The **Cumulant analysis** is a “simple fit” working in the case of one single and rather monodisperse population of solutes. A polynomial (Equation 5) is fitted to the physically relevant portion (typically excluding 10% of the low-lag time and 10% of the high lag-time data points) of the autocorrelation

function. Its coefficients contain the average and dispersity of lag times. In this equation, Γ represents the average inverse relaxation time.

The **Regularized inverse Laplace transform** enables studying large distributions of solute sizes as a histogram. The CONTIN algorithm proceeds by fitting the autocorrelation function with the sum of a predefined number (typically 250, "grid size") of exponential decays associated with relative weights (relative height of the histogram bar). The result is the decay rate distribution function $G(\tau)$ (Equation 6). Note: $1/\tau$ is often written Γ.

$$\ln\left(g_1(\tau)\right) \approx \ln(A) - \Gamma \cdot \tau + \frac{\mu_2}{2!} \cdot \tau - \frac{\mu_3}{3!} \cdot \tau + \ldots$$

Equation 5. Cumulant analysis polynomial.

$$g_1(\tau) \approx \int_{\Gamma_{min}}^{\Gamma_{max}} G(\Gamma) \cdot e^{-\Gamma \cdot \tau} d\Gamma$$

Equation 6. Decay rate distribution function *G*.

As G will mathematically have a lot of solutions, filters are applied to improve the usual χ^2 least-square matching criteria in order to favor the physically relevant solutions: first, distributions including negative lag times are automatically rejected, then distributions with the smoothest details and the lowest slopes $\left(\frac{\partial G}{\partial \Gamma}\right)$ ("parsimony") are favored. Such a sorting of possible solutions is said to bring the typical incertitude of this model below 10%.

G is intensity-weighted: the relative height of the peaks reflects the relative scattering power of each population, and not the number or mass (the intensity is roughly proportional to the mass, but the angle of detection plays also a role through the particle form factor). This means that populations of larger particles will always be fitted with large peaks although a population of smaller particles might be ultra-dominant in number.

The **non-linear decay time analysis** allows fitting $AC(\tau)$ from a small number of exponential decays with predefined peak shapes. It is convenient for mixtures of relatively narrow populations.

c) From correlation time to correlation length, Stokes-Einstein equation

The relation between diffusion coefficient and particle mobility is given by Einstein's Brownian motion equation (Equation 7), where D (m^2/s) is the diffusion coefficient, μ the particle mobility (particle speed / potential difference), k_BT (J) the particle thermal energy. The particle mobility is also related to the particle hydrodynamic radius by the Navier-Stokes equation (in the case of hard spheres in homogeneous medium (solvent molecules small against particles) at low Reynolds number, i.e. laminar flow or very small particles):

$$D = \mu \cdot k_B T$$

Equation 7. The Einstein equation.

$$\mu = \frac{1}{6\pi\eta R}$$

Equation 8. Navier-Stokes equation.

The Reynolds number is defined as $\Re e = \frac{\rho \cdot v \cdot L}{\mu} = \frac{\rho \cdot v^2 / L}{\mu \cdot v / L^2}$ and measures the ratio between forces of inertia and viscous forces, v (m/s) being the fluid velocity, ρ (kg/m^3) the fluid volumic mass, η (Pa·s = kg·m^{-1}·s^{-1}) the dynamic viscosity and L (m) a characteristic dimension of the system (in this case the particle diameter).

Their combination yields the relation between diffusion coefficient and hydrodynamic radius (Equation 9), which when adapted to interferences detected by light scattering, yields Equation 10, where the diffusion coefficient D is equal to Γ/q^2 : this enables the conversion from lag time to radius.

$$D = \frac{k_B \cdot T}{6\pi\eta R_H}$$

Equation 9. Diffusion coefficient and hydrodynamic radius.

$$R_H = \frac{k_B T}{6\pi\eta} \cdot \frac{q^2}{\Gamma}$$

Equation 10. Hydrodynamic radius and Brownian relaxation time.

What is measured is an apparent hydrodynamic radius, which has to be cleared from the angle-dependence, by extrapolating q^2/Γ to zero q^2.

d) Remarks

The 'generalized Stokes-Einstein equation takes the particle-particle interaction (friction factor) into account and is useful in a semi-dilute regime. The simple "tracer diffusion coefficient" D becomes the "mutual diffusion coefficient" D_m.

There exists a further detection mode called heterodyne detection. In this particular setup, part of the primary light is reflected towards the detector where it interferes with the scattered beam. This portion of primary light acts as a dominant stable reference for the frequency-shifted scattered light, whereas in the simple and common case of homodyne detection, one detects all interferences between all frequencies. The stable reference permits a gain in either accuracy or sampling time.

4. Static light scattering

a) Rayleigh ratio and calibration with toluene

The **Rayleigh ratio** (m^{-1}) is a measure of the scattering power (Equation 11), where i_0 is the incident laser intensity and i_S the detected scattered intensity, d is the sample-to-detector distance, f is the polarization factor $(1+\cos^2\theta)/2$ (equal to 1 if the incident beam has a linear vertical polarization i.e. normal to the detection plane), and V is the scattering volume, i.e. the intersection between the illuminated sample cylinder and the detection cone. [130]

$$R_\theta = \frac{i_s(\theta)}{i_0} \cdot \frac{d^2}{f \cdot V}$$

Equation 11. The Rayleigh ratio.

In practice, $\frac{i_s(\theta)}{i_0}$ is acquired as an average over time $\left\langle i_\theta / i_0 \right\rangle$. The solute Rayleigh ratio is accessible after removing the solvent contribution (Equation 12), in an intensity-calibrated setup, i.e. of known $\left(\frac{d^2}{f \cdot V} \right)$.

$$\Delta R_\theta^{\ SOLUTE} = R_\theta^{SAMPLE} - R_\theta^{SOLVENT} = \left[\left\langle i_\theta / i_0 \right\rangle_{SAMPLE} - \left\langle i_\theta / i_0 \right\rangle_{SOLVENT} \right] \cdot \frac{d^2}{f \cdot V}$$

Equation 12. Solute Rayleigh ratio.

The calibration requires measuring $\left\langle i_\theta / i_0 \right\rangle_{STANDARD}$ from a sample of known Rayleigh ratio. Equation 13 is the calibrated useful form.

$$\Delta R_\theta^{\ SOLUTE} = \frac{\left\langle i_\theta / i_0 \right\rangle_{SAMPLE} - \left\langle i_\theta / i_0 \right\rangle_{SOLVENT}}{\left\langle i_\theta / i_0 \right\rangle_{STANDARD}} \cdot R_\theta^{STANDARD}$$

Equation 13. Calibrated solute Rayleigh ratio.

Toluene is typically used for calibration because it presents several advantages over other solvents:

- a strong Rayleigh ratio ($R_\vartheta^{Toluene}$ = 1.352·10^{-5} cm^{-1} at 20°C), which is about 10 times more than that of water ;

- a close index match with glass (toluene 1.49, quartz 1.5), which reduces reflections and refractions on the laser path and thus reduces reflection and scattering artifacts ;

- a low viscosity, which allows quick Brownian motions and therefore good scattering intensity averages over a reduced acquisition time.

b) Contrast factor and normalized inverse Rayleigh ratio

The contrast factor *K* gathers all constant parameters (Equation 14), with n_{STD} standard solvent refractive index and ∂*n*/∂*C* solution refractive index increment (i.e. solvent/particle contrast, which determines the sensitivity of the measurement). For polymer solutions is usually about 10^{-7} mol·cm^2·g^{-2}, assuming a typically small refractive index increment of 0.1 mL/g, 300 K and a red laser (~600 nm). The contrast factor enables normalizing the Rayleigh ratio so that measurements between different sample and setups may be compared. Combining Equation 13 and Equation 14 yields the general expression of the normalized inverse Rayleigh ratio (NIRR, mol/g) of the solute (with *C* mass concentration and *Π* osmotic pressure).

$$K = \frac{\left(2\pi \cdot n_{STD} \cdot \frac{\partial n}{\partial C}\right)^2}{N_A \cdot \lambda^4}$$

Equation 14. Contrast factor.

$$\frac{K \cdot C}{\Delta R_\theta} = \frac{1}{k_B T} \cdot \frac{\partial \Pi}{\partial C}$$

Equation 15. Normalized inverse Rayleigh ratio.

c) Osmotic pressure and virial coefficients

The virial coefficients describe the concentration dependence of the solvent chemical potential (Equation 16, in J/mol), with *V* solvent partial molar volume (m^3/mol) and *Π* solvent osmotic pressure (Equation 17), expressed in Pascal (Pa), i.e. kg·m^{-1}·s^{-2}.

$$\mu_S - \mu_S^0 = -\Pi \cdot V$$

Equation 16. Osmotic pressure and chemical potential

$$\Pi = RT \cdot \left(A_1 \cdot C + A_2 \cdot C^2 + \ldots\right)$$

Equation 17. Osmotic pressure and virial coefficients.

In short, the first virial coefficient describes the particle itself (molar mass), while the second virial coefficient compares the particle/solvent affinity with the particle/particle affinity. It is positive in a good solvent; negative for a poor solvent and zero in theta-conditions. This means that for small non-interacting particles, the NIRR is directly equal to the molar mass (M_W in case of polydispersity). However, in the case of large or interacting particles, deviations from this ideal situation can be calculated via a solution structure factor *S(ϑ)* (interferences due to particle/particle interactions) and a form factor *P(ϑ)* (interferences due to particle shape) as in Equation 18. *P* is equal to 1 for small particles: they scatter equally in all directions.

$$\frac{K \cdot C}{\Delta R_\theta} = \frac{1}{M} \cdot \frac{1}{P \cdot S}$$

Equation 18. Interference factors.

d) Random coil model shape and Zimm plot

The simplest model for large particles assumes neutral random coils (**Error! Reference source not found.**) (a random coil is considered as a string of individual scatterers with no particular orientation). This is the basis for the Zimm plot, which is solved in $1/M_W$, $2A_2$ and $R_G^2/3$ through two consecutive linear regressions and extrapolations to zero angle (q^2) and zero concentration.

R_G is the Radius of gyration (Equation 20), defined as the square-average of the mass-weighted distances from the center of mass within one particle over its whole volume (in polymer science R_G has nothing to see with the rotation momentum). The local density is integrated over the particle volume, with ***r*** position vector and *ρ(**r**)* local density.

$$\frac{K \cdot C}{\Delta R_\theta} = \left(\frac{1}{M_W} + 2 \cdot A_2 \cdot C \right) \cdot \left(1 + q^2 \cdot \frac{R_G^2}{3} \right)$$

Equation 19. Standard SLS model.

$$R_g{}^2 = \frac{\iiint r^2 \rho(\vec{r}) dr^3}{\iiint \rho(\vec{r}) dr^3}$$

Equation 20. Radius of gyration R_G.

In practice, this model is also commonly used for large particles that have nothing to see with random coils. Details of form factors quickly vanish when the polydispersity increases. Eventually, all polydisperse particles 'look like random coils' when taken as an average, in that they can be fitted with a linear form factor i.e. a seemingly random distribution of mass. Despite the apparent physical

incompatibility, this approach is valid when such a radius of gyration is compared to the hydrodynamic radius from DLS. Table 6 summarizes some typical characteristic values of the ratio R_G/R_H.

Table 6. Sphericity ratios of model shapes.

Model shape	R_G/R_H
homogeneous hard ball	0.78
hollow sphere	1
monodisperse random coil, theta-conditions	1,5
polydisperse random coil, theta-conditions	1,7
monodisperse random coil, good solvent	1.8
polydisperse random coil, good solvent	2

e) Form factors

However, in the case of large colloids of rather monodisperse, well-defined shape approaching 60 nm or more, the correct particle form factor should be used (examples given in Table 7) in the more general Equation 21.

$$\frac{K \cdot C}{\Delta R_\theta} = \left(\frac{1}{M_W} + 2 \cdot A_2 \cdot C \right) \cdot \frac{1}{P}$$

Equation 21. SLS model for large weakly interacting colloids.

Table 7. Examples of model form factors.

Model shape	**Form factor**
Gaussian coil	$\frac{2}{u^4}\left(e^{-u^2} + u^2 - 1\right)$ $u = R_G.q$
Hard sphere	$\left(\frac{\sin(u) - u.\cos(u)}{u^3/3}\right)^2$ $u = R.q$
Vesicle	$\left\{\frac{3}{u_{out}^3 - u_{inn}^3}\left[\sin(u_{out}) - u_{out} \cdot \cos(u_{out}) - \sin(u_{inn}) + u_{inn} \cdot \cos(u_{inn})\right]\right\}^2$ $u_{out} = q.R_{out}$ *and* $u_{inn} = q.R_{inn}$ (inner and outer radii)

Additional plots and analyses

Various ways to display and analyze SLS data all aim at obtaining quasi-linear dependences with concentration or angle (e.g. Zimm and Berry plots), or at least intuitive representations (e.g. Debye and Krotzky plot), depending on the nature of the observed colloid.

Table 8. SLS plots and analyses.

Name	Data formulation	Interest
Zimm	$K \cdot C/R_\vartheta = f(q^2+k \cdot C)$	Random coils, polydisperse or poorly defined shapes
Berry	$\sqrt{(K \cdot C/R_\vartheta)} = f(q^2+k \cdot C)$	large particles with strong inter-particle interactions involving the third virial coefficient
Debye	$R_\theta/(K \cdot C) = M \cdot P(q^2)$	large non-interacting particles ; directly shows the form factor
Guinier	$\log(R_\theta/(K \cdot C)) = M \cdot P(q^2)$	large non-interacting particles with strong form factors
Krotzky	$R_\theta \cdot q^2 = f(q)$	Thin rods. Angle-dependant random walk to thin rod transition

C. Projects and collaborations co-published in parallel to the PhD studies

1. Ionic Liquid-Crystal Precursors (ILCPs) for CuCl Platelets[142]

This chapter is constituted by the following publication : Ionic Liquid-Crystal Precursors (ILCPs) for CuCl Platelets: The Origin of the Exothermic Peak in the DSC Curves, A. Taubert, C. Palivan, O. Casse, F. Gozzo, B. Schmitt, The Journal of Physical Chemistry C 2007 111 (11), 4077-4082.

ARTICLES

Ionic Liquid-Crystal Precursors (ILCPs) for CuCl Platelets: The Origin of the Exothermic Peak in the DSC Curves

Andreas Taubert,*,†,§ Cornelia Palivan,† Olivier Casse,† Fabia Gozzo,‡ and Bernd Schmitt‡

Department of Chemistry, University of Basel, CH-4056 Basel, Switzerland, and Swiss Light Source, Paul-Scherrer-Institute, CH-5232 Villigen, Switzerland

Received: August 17, 2006; In Final Form: December 12, 2006

We have recently reported (Taubert, A.; Steiner, P.; Mantion, A. *J. Phys. Chem. B* **2005**, *109*, 15542) that DSC traces of an ionic liquid-crystal precursor for CuCl nanoplatelets exhibit an intense exothermic peak. The current paper presents a detailed investigation into the origin of this exothermic peak. Electron paramagnetic resonance spectroscopy, high-temperature X-ray scattering, and isothermal differential scanning calorimetry show that the Cu(II)−Cu(I) reduction is complete after about 35 min. It is the rate-determining step in the CuCl formation process and is responsible for the exothermic peak. Cu(II) reduction strongly overlaps with the formation of a first generation of CuCl particles. The formation of the large CuCl platelets observed in the SEM (Taubert, A. *Angew. Chem., Int. Ed*., **2004**, *43*, 5380) is inhibited by the organic matrix and occurs over the course of about 5 h.

Introduction

Ionic liquids (ILs) have been studied intensely, because they can often be green and efficient solvents.[1] While initially a domain of organic and electrochemists, ILs have more recently attracted attention from the (inorganic) materials community. As ILs can easily be tuned to interact with many different surfaces and chemical environments, they should be prime candidates for the controlled fabrication of inorganic and organic/inorganic hybrid materials. In some cases, ILs indeed provide protocols for the fabrication of materials that are not otherwise accessible, or only with great effort.[2]

So far, inorganic materials chemistry in ILs has mainly focused on the fabrication and stabilization of ordered metal oxides[3−8] or on metal, alloy, metal oxide, and metal sulfide nanoparticles.[9−21] For an overview, see ref 22. Ionic liquid crystals (ILCs), that is, ionic liquids with a long-range order, have also been studied in some detail.[23−39]

Combining ILCs and inorganic materials chemistry, we have recently shown that an ILC from a 50:50 (wt/wt) mixture of bis(dodecyl pyridinium) tetrachlorocuprate **1** and 6-*O*-palmitoyl ascorbic acid **2** (Scheme 1) is a precursor (an ionic liquid-crystal precursor, ILCP) for CuCl platelets.[40] We have also shown that crystalline ILCP analogs can serve as templates for metal particle formation.[41] Similar approaches have more recently also been published by other research groups.[42−45]

SCHEME 1: Bis(dodecyl pyridinium) Tetrachlorocuprate 1 and 6-*O*-Palmitoyl Ascorbic Acid 2

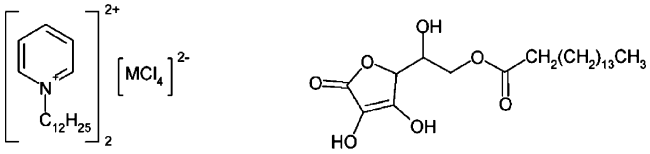

1 M = Cu **2**

ILCPs composed of **1** and **2** are crystalline or partly crystalline at room temperature and liquid crystalline at elevated temperatures. The liquid-crystal region is up to 90 °C wide, but because **1** and **2** react to form CuCl, the phase diagram reported earlier is only a transient phase diagram of the original mixture of **1** and **2**. DSC traces of these mixtures exhibit a broad exothermic peak between about 70 and 170 °C, which is due to a so far unspecified process involved in CuCl particle formation.[46]

To more clearly determine the origin of the exothermic peak in the DSC and to better understand CuCl particle formation, we have performed time-resolved electron paramagnetic resonance (EPR) spectroscopy, high-temperature in-situ X-ray scattering, and isothermal differential scanning calorimetry (DSC) measurements. The experiments show that the exothermic peak is caused by the thermally induced reduction of Cu(II) to Cu(I), whereas the crystallization of the final CuCl platelets is strongly inhibited by the organic matrix and starts only after about 2 h.

Experimental Section

Synthesis. 6-*O*-Palmitoyl ascorbic acid **2** was obtained from Fluka and used without further purification. Dodecylpyridinium chloride (Aldrich) was recrystallized several times from THF, affording a crystalline white powder. Compound **1** was obtained

* Author to whom correspondence should be addressed at Institute of Chemistry, University of Potsdam, Karl-Liebknecht-Str. 24-25, Building 26, D-14476 Golm, Germany. Tel: ++49 (0)331 977 5773. E-mail: ataubert@uni-potsdam.de.

† University of Basel.

‡ Swiss Light Source.

§ Current address: Institute of Chemistry, University of Potsdam, D-14476 Golm, Germany and Max-Planck-Institute of Colloids and Interfaces, D-14476 Golm, Germany.

10.1021/jp065332q CCC: $37.00
Published on Web 02/24/2007

as described by Neve et al.[24] Mixtures of **1** and **2** were obtained as described previously.[46]

Thermal Analysis. Isothermal DSC experiments were run between 50 and 110 °C on a Perkin-Elmer DSC6. The DSC was held at the desired temperature, and the DSC pan containing the sample was loaded. ΔH values were calculated using an apparent molecular weight of 566.4 g/mol computed from the weight fractions (50 wt % of each component) and their respective molecular weight of 702.2 (**1**) and 430.6 (**2**) g/mol, respectively.

Spectroscopy. EPR spectra were recorded at 20, 75, and 80 °C using a Bruker ESP300E X-band spectrometer with an ER4103TM cylindrical mode resonant cavity. A 100-kHz modulation frequency and 0.3-mT modulation amplitude were used in all experiments. For measurements of **1** and for mixtures of **1** and **2**, 2-mW and 10-mW microwave power, respectively, were used. The samples were measured in air and nitrogen. UV−vis spectroscopy was done on a Safas 2000 UV/Vis spectrometer from 250 to 800 nm. **1** was dissolved in acetonitrile and measured at room temperature.

X-ray Diffraction. X-ray scattering experiments were done at the Swiss Light Source (Paul Scherrer Institute, Villigen) using the powder diffraction station with the MYTHEN microstrip detector[47] at the materials science beamline X04SA. Samples were mounted in 1 mm Lindemann capillaries (Hilgenberg) and measured from 35 to 180 °C while rotating the sample (instead of rotating the samples). In a second set of experiments, the samples were held at 90 °C until the peak intensities did not change anymore. Time windows for measurement of individual X-ray patterns were 15 s. For data analysis, 10 patterns were averaged providing a total time resolution of below 3 min/step. Beam energy was 17.5 keV, and the X-ray wavelength λ was 0.708 Å. Data analysis was performed with OriginLab Origin 6.1. Peaks were background-subtracted and fitted with Lorentzians to give peak position, width, area, and full width at half-maximum (FWHM).

Results and Discussion

Differential Scanning Calorimetry. Figure 1 shows a typical isothermal DSC trace of a 50:50 (wt/wt) mixture of **1** and **2** during the first hour of the experiment. All traces exhibit an intense endothermic peak. It is due to the loading and heating of the DSC pan and the melting of the sample in the DSC sample cell at the very beginning of the experiment. This signal is immediately followed by a less intense exothermic peak, which corresponds to the exothermic peak observed in our earlier experiments.[46]

Figure 2 and Table 1 show that the ΔH values of the exothermic peak have a roughly linear correlation with the holding temperature of the sample, although some samples show a rather large error in the data. We assign this error to heterogeneities in the sample: even though our earlier DSC experiments have shown that the samples (with a few exceptions) do not contain large heterogeneities, they may be significant enough to cause the variations in the measurements. This is supported by the breadth of about 100 °C of the exothermic peak in the original temperature ramping experiments.[46]

The linear reduction of ΔH with holding temperature clearly demonstrates that the reaction causing the exothermic peak is thermally activated. However, Figure 3 shows that the half-lives of reaction ($t_{1/2}$) obtained from the DSC curves are discontinuous. At 50 °C, $t_{1/2}$ is about 20 min. Between 55 and 70 °C, $t_{1/2}$ is between 8 and 14 min, but these values are roughly

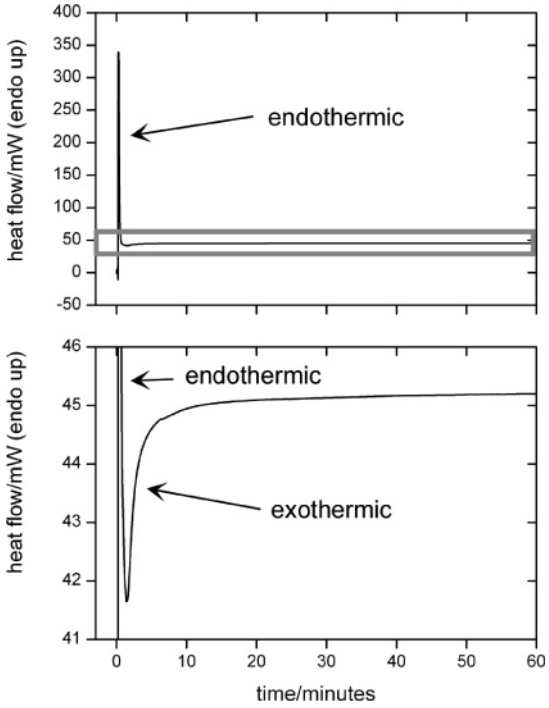

Figure 1. Representative isothermal DSC trace of a mixture of **1** and **2** at 110 °C. The gray frame indicates the magnified area shown in the lower graph. The endothermic peak is due to the heating of the DSC pan and the melting of the sample at the beginning of the experiment.

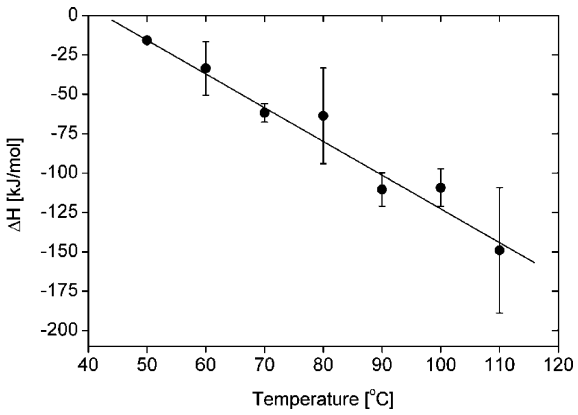

Figure 2. ΔH values of the exothermic peak vs holding temperature.

TABLE 1: ΔH Values of the Exothermic Peaks at Different Holding Temperatures[a]

holding temperature	ΔH [kJ/mol]
temperature ramping[b]	−150 ± 60.5
110	−149.1 ± 39.8
100	−109.4 ± 11.9
90	−110.4 ± 10.6
80	−63.7 ± 30.4
70	−61.8 ± 5.8
60	−33.6 ± 16.9
50	−15.7 ± 0.4

[a] Values and errors were obtained from three repeat measurements. [b] Ref 46.

constant within the experimental error, which is relatively large at 20−25%. At 80 °C and higher, $t_{1/2}$ is between 2 and 3 min.

We explain the lower "gap" between 50 and 55 °C with the fact that, at 50 °C, some fractions of both **1** and **2** are still below their melting temperature and that the sample is not perfectly homogeneous. Partial crystallinity will reduce the mobility of the components and also their ability to react. At and above 55

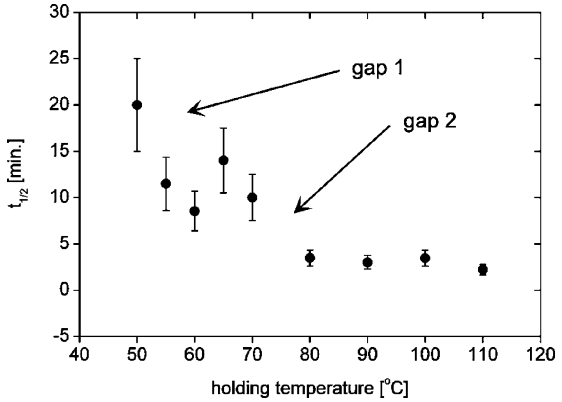

Figure 3. Half-lives $t_{1/2}$ of the exothermic peak vs holding temperature. "Gap 1" and "gap 2" indicate the locations of the drops in $t_{1/2}$. The error bars indicate the maximum estimated error of 25% obtained from three repeat measurements.

°C, pure **1** is above the crystalline−liquid-crystalline transition,[24] which improves the mobility of **1** and presumably the miscibility with **2**. This will lead to an improved and more homogeneous reactivity throughout the sample.

The upper gap in $t_{1/2}$ above 70 °C is most likely due to effects associated with Cu(II) reduction or CuCl nucleation, because this gap between short and long $t_{1/2}$ values is right at the lower end of the exothermic DSC peak reported earlier.[46]

Overall, isothermal DSC measurements show that the process causing the exothermic peak is completed after 30−40 min. The signal vanishes and no further peaks have been observed at later stages; therefore, a process occurring in the first 5−30 min (depending on the holding temperature) is responsible for the exothermic peak.

In principle, there are two major possible reasons for the exothermic peak: (i) thermally induced reduction of Cu(II) to Cu(I), and (ii) formation of the CuCl platelets after Cu(I) formation. As electron paramagnetic resonance (EPR) spectroscopy is sensitive for the paramagnetic Cu(II) ion, EPR spectroscopy is suited for monitoring the Cu(II) reduction and hence to discriminate between options (i) and (ii).

EPR Spectroscopy. Figure 4 shows the EPR spectra of **1** and its mixture with **2** at 20 and 80 °C. At room temperature, all spectra show broad and poorly resolved lines. This is typical for pure samples of low-molecular-weight transition-metal complexes with strong exchange interactions between unpaired electrons on different molecules. However, there are significant differences in the spectra of pure **1** compared to the spectra of the mixtures of **1** and **2**; the spectrum of **1** has very broad features that are essentially isotropic with a *g*-value of 2.163 and a line width $\Delta\Gamma \approx 700$ G. Contrary to **1**, an anisotropic spectrum with $g_{iso} = 2.197$ and a line width $\Delta\Gamma \approx 350$ G characterizes the mixture of **1** and **2**. Increasing temperatures do not change the spectral features, but the line width increases substantially.

To observe the reduction of the Cu(II) ion to Cu(I), EPR spectra were recorded as a function of time, Figure 5. After about 30 min the signal is basically zero at both temperatures, which indicates that the Cu(II) concentration is below the detection limit and almost all Cu(II) is reduced to EPR-silent Cu(I).

The decrease of the EPR signal intensity indicates that during the first 11−12 min 80−85% of the initial amount of Cu(II) is reduced to Cu(I). The data also show that the rates for this initial reduction are similar for both temperatures. After a reaction time of 11−12 min, however, the reduction of the remaining Cu(II)

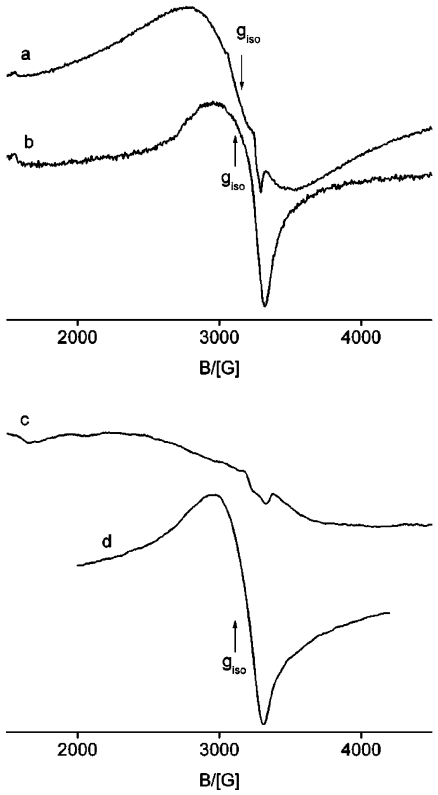

Figure 4. Ambient-temperature EPR spectra of pure **1** (a) and a 50:50 (wt/wt) mixture of **1** and **2** (b). High-temperature (80 °C) EPR spectra of pure **1** (c) and a 50:50 (wt/wt) mixture of **1** and **2** (d) immediately after their placement in the resonant cavity.

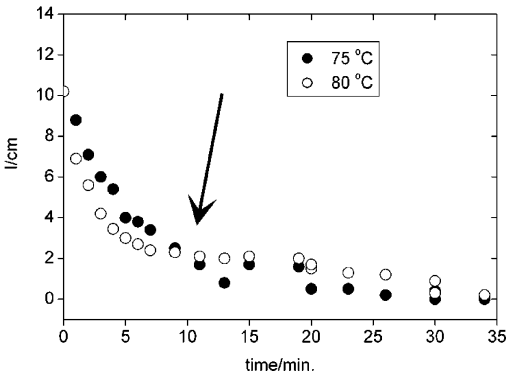

Figure 5. Time evolution of the EPR signal intensity at 75 and 80 °C. The arrow shows the crossover between measurement at 80 and 75 °C (see text for details).

occurs simultaneously with another process, which is indicated by a different slope in the data and the crossover between the intensities of the EPR signal. Because after 11− 12 min the intensity of the EPR signal at 75 °C is lower than at 80 °C, we conclude that this second process affects the reduction such that at 75 °C the reduction of the remaining Cu(II) is more rapid than at 80 °C.

One possible explanation is heterogeneous nucleation on already existing CuCl particles. Indeed, X-ray diffraction (see below) shows that already after 2 − 3 min, CuCl particles are present in the reaction mixture above 50 °C. Therefore, EPR data suggest that heterogeneous nucleation is more pronounced at lower temperatures, which could lead to a faster reduction of the remaining Cu(II) ions by more efficiently removing the Cu(I) ions from the reaction mixture via incorporation into the growing crystals. Alternatively, the intensity variations could

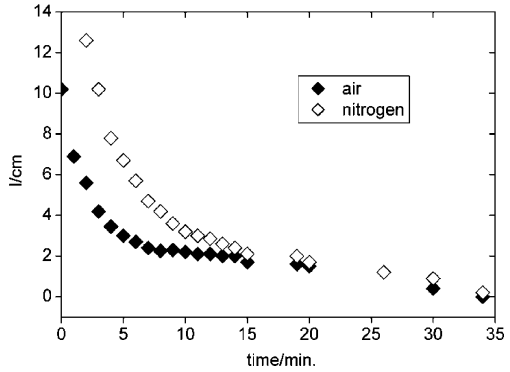

Figure 6. Intensity of the Cu(II) EPR signal vs time in air and nitrogen, respectively, at 80 °C.

also be due to sample heterogeneity, similar to the DSC measurements.

To determine whether or not the reduction of Cu(II) to Cu(I) is influenced by the atmosphere in which the sample is placed, EPR spectra of the ILCP were measured in air and nitrogen as a function of time. Figure 6 shows that in a nitrogen atmosphere, the initial reduction is delayed. However, complete reduction is achieved after about 30 min in both air and nitrogen.

In summary, EPR and DSC are consistent in that $t_{1/2}$(EPR) is between 3 and 4 min, which is reasonably close to $t_{1/2}$(DSC) for holding temperatures at and above 80 °C. EPR and isothermal DSC measurements thus demonstrate that the exothermic peak observed earlier in the DSC heating traces[46] is due to the thermally induced reduction of Cu(II) by **2**.

X-ray Scattering. To further rule out that the exothermic peak in the DSC heating curves is due to CuCl crystal formation (and not to Cu(II) reduction), we have done high-temperature X-ray scattering experiments. Compound **2** and the free ligand dodecyl pyridinium chloride show a behavior consistent with our earlier measurements.[46] As the phase behavior of **1** is known[24] and has been confirmed by our earlier DSC and optical microscopy experiments,[46] we did not study **1** individually here.

Figure 7a shows X-ray patterns obtained from temperature ramping experiments on a 50:50 (wt/wt) mixture of **1** and **2**. The patterns show two reflections at low angles that can be assigned to the 100 and 200 reflections of a layered ILCP. This assignment is consistent with our earlier assignment from optical microscopy and room-temperature XRD.[40,46] However, because the patterns recorded at and above 35 °C show only a few weak remaining reflections due to crystalline **1** or **2**, X-ray measurements show that above 35 °C the ILCP is in a (transient and reactive) liquid-crystal state.

The lamellar spacing of the ILCP at and above 35 °C (the lowest temperature accessible with the oven available) is 34.8 Å. This is slightly larger than the 33.1 Å observed at room temperature.[46] The approximately 5% difference in the layer spacing is assigned to minor differences in the sample composition between different measurements.

Figure 7b shows that heating the sample also produces reflections that correspond to CuCl (JCPDS 6-344). As these reflections are already observed at around 50 °C, X-ray confirms isothermal DSC, where an exothermic peak has been observed as low as 50 °C. As a result, X-ray of the ILCP shows that the formation of CuCl clusters or similar structures starts already below 70 °C, where the exothermic peak appears in temperature-ramping DSC.[46]

Finally, we have acquired X-ray patterns at 90 °C over the course of several hours. Unfortunately, Figure 8 shows that the CuCl reflections do not change over the course of the measurement. Because there are no CuCl reflections visible below about 50 °C (see above) and because $t_{1/2}$ is short at higher temperatures, these data suggest that the thermally activated reduction of Cu(II) to Cu(I) is the rate-determining step, but is immediately followed by the formation of a first generation of small clusters or particles.

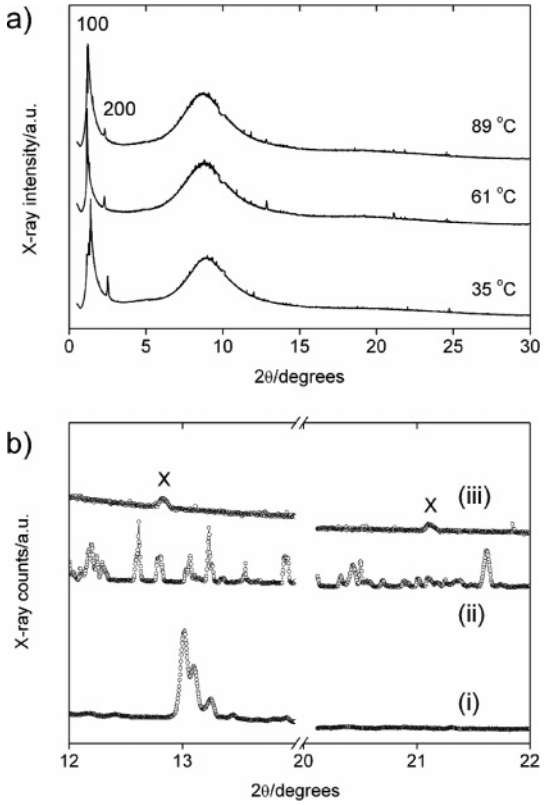

Figure 7. Temperature ramping data: (a) X-ray patterns of an ILCP at various temperatures; 100 and 200 denote the 100 and 200 reflections of the lamellar ILCP. (b) Magnified view of two regions of the X-ray patterns showing the CuCl reflections (x): (i) pure **2**, (ii) pure ligand dodecylpyridinium chloride, (iii) ILCP of 50:50 (wt/wt) **1** and **2** at 89 °C showing CuCl reflections (JCPDS 6-344).

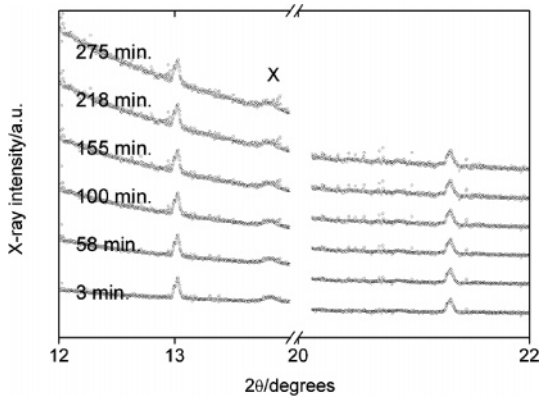

Figure 8. CuCl reflections as a function of reaction time. Neither the position nor the intensity changes after reaching the intended reaction temperature of 90 °C after 2 min. An unidentified reflection is denoted by x.

As the heating time to 90 °C is about 2 min and $t_{1/2}$ at 90 °C is also between 2 and 3 min, these data present clear evidence for the formation of small primary particles immediately after Cu(II) reduction. Therefore, reduction and nucleation phases most likely strongly overlap. At this stage, neither SEM nor optical microscopy show particles. The final particle morphology as observed in the SEM after 24 h[40] must

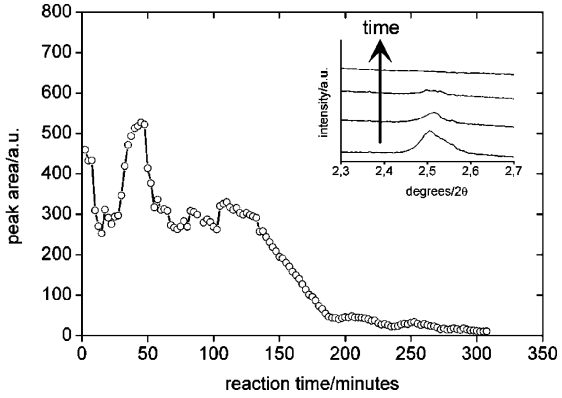

Figure 9. Peak area evolution of the 200 reflection of a 50:50 (wt/wt) mixture of **1** and **2** at 90 °C with reaction time. Inset: select 200 reflections showing the decrease of the peak area after 100 min of reaction time.

therefore be the consequence of aggregation or recrystallization of these first particles.

Figure 9 shows that (unlike the CuCl reflections shown in Figure 8) the 200 reflection of the ILCP changes with time. First, we observe a rapid drop in the peak area, which is followed by an increase at about 25 min, followed by another drop at about 50 min. Thereafter, the peak area remains constant until at about 130 min of reaction time the 200 peak area decreases steadily until the peak vanishes.

Proposed Growth Model. On the basis of our data and using the changes of the 200 peak area as a guideline for discussion, we suggest the following growth model for CuCl platelets from our ILCP: the first rapid decrease in the 200 peak area is due to melting of the ILCP and the transition into the liquid-crystal state upon rapid heating to 90 °C. This is consistent with isothermal DSC experiments, Figures 1 and 2.

The increase of the 200 peak area after 25 min can be explained by a combination of EPR, DSC, and X-ray data. EPR (Figures 5 and 6) shows that the Cu(II) reduction is complete after about 25−30 min, but proceeds as a two-step process. EPR and isothermal DSC (Figure 3) show that the reaction has a $t_{1/2}$ of about 2−4 min at 90 °C. X-ray diffraction (Figures 7 and 8) shows that CuCl particles form already at about 50 °C and after a few minutes.

As a consequence, the increase of the peak area after 25 min is explained as follows. Cu(II) reduction and formation of primary CuCl particles are strongly overlapping processes. Complete Cu(II) reduction requires about 30 min, but the first particles form after about 3 min. This suggests that after about 25−30 min there are many small particles in the sample. Also, the organic molecules (i) are still present, (ii) still have a supramolecular (layered) order as seen in the X-ray patterns, and (iii) contain polar and nonpolar regions. Therefore, the small CuCl particles can sequester into one of these domains. As a result, the X-ray contrast and hence the 200 peak area increases due to increased electron density in one domain type (polar or nonpolar). Possibly, the particles also increase the overall order in the assembly.

The 200 peak area reduction after 50 min could be due to a change in the CuCl growth mechanism; initially, in the absence of other particles, CuCl forms via "homogeneous" nucleation within the fluid ILCP. However, EPR suggests that a second process, possibly heterogeneous nucleation, starts after 10−12 min. Therefore, particles may also grow by heterogeneous processes once primary particles exist. Alternatively, the primary particles could undergo an Ostwald ripening or recrystallization process, all of which disturbs the order in the reacting ILCP and thus reduces the X-ray contrast again.

Finally, the growing or aggregating particles reach hundreds of nanometers to micrometers in size.[40] As these rather large crystals grow, they increasingly disrupt the order of the ILCP without entirely destroying it. This will give rise to the disappearance of the 200 but not the 100 reflection.

Conclusion

As pointed out earlier,[40,46] ILCPs could serve as a generic precursor for the low-temperature synthesis of inorganic matter. This study is a continuation of our efforts aimed at quantifying the role of ILCPs for the controlled formation of inorganics. In particular, the study shows that the formation of CuCl platelets within an ILCP of **1** and **2** is a very complex process with several overlapping steps. This reduces the possibilities of quantitatively studying and exactly controlling the particle formation. As a result, single-component ILCPs, similar to a recent example by Douce and colleagues[42] (but with the possibility of depositing a wide range of inorganics and not only metals), would be more suitable for technical applications and quantitative study. Experiments aimed at simplifying our system are underway.

Acknowledgment. The authors thank A. Mantion and R. Mattei for help with the synchrotron experiments and Prof. K. Binnemans (KU Leuven) for useful discussions. C.P. thanks Prof. A. Schweiger (ETH Zürich), in whose laboratory the EPR measurements were done. We thank the Swiss National Science Foundation and the NCCR Nanosciences for financial support, and A.T. acknowledges the Holcim Stiftung Wissen for a Habilitation Fellowship.

References and Notes

(1) *Ionic Liquids in Synthesis*; Wasserscheid, P, Welton, T., Eds.; Wiley-VCH: Weinheim, 2002.
(2) Taubert, A. *Acta Chim. Slov.* **2005**, *52*, 183.
(3) Nakashima, T.; Kimizuka, N. *J. Am. Chem. Soc.* **2003**, *125*, 6386.
(4) Zhou, Y.; Antonietti, M. *Adv. Mater.* **2003**, *15*, 1452.
(5) Zhou, Y.; Antonietti, M. *Chem. Commun.* **2003**, 2564.
(6) Zhou, Y.; Antonietti, M. *J. Am. Chem. Soc.* **2003**, *125*, 14960.
(7) Dai, S.; Ju, Y. H.; Gao, H. J.; Lin, J. S.; Pennycook, S. J.; Barnes, C. E. *Chem. Commun.* **2000**, 243.
(8) Yang, L.-X.; Zhu, Y.-J.; Wang, W.-W.; Tong, H.; Ruan, M.-L. *J. Phys. Chem. B* **2006**, *110*, 6609.
(9) Dupont, J.; Fonseca, G. S.; Umpierre, A. P.; Fichtner, P. F. P.; Teixeira, S. R. *J. Am. Chem. Soc.* **2002**, *124*, 4228.
(10) Desmukh, R. R.; Rajagopal, R.; Srinivasan, K. V. *Chem. Commun.* **2001**, 1544.
(11) Swatloski, R. P.; Spear, S. K.; Holbrey, J. D.; Rogers, R. D. *J. Am. Chem. Soc.* **2002**, *124*, 4974.
(12) Fonseca, G. S.; Umpierre, A. P.; Fichtner, P. F. P.; Teixeira, S. R.; Dupont, J. *Chem. Eur. J.* **2003**, *9*, 3263.
(13) Scheeren, C. W.; Machado, G.; Dupont, J.; Fichtner, P. F. P.; Ribeiro Texeira, S. *Inorg. Chem.* **2003**, *42*, 4738.
(14) Rossi, L. M.; Dupont, J.; Machado, G.; Fichtner, P. F. P.; Radtke, C.; Baumvol, I. J. R.; Teixeira, S. R. *J. Braz. Chem. Soc.* **2004**, *15*, 904.
(15) Trewyn, B. G.; Whitman, C. M.; Lin, V. S.-Y. *Nano Lett.* **2004**, *4*, 2139.
(16) Yoo, K.; Choi, H.; Dionysiou, D. D. *Chem. Commun.* **2004**, 2000.
(17) Cassol, C. C.; Umpierrre, A. P.; Machado, G.; Wolke, S. I.; Dupont, J. *J. Am. Chem. Soc.* **2005**, *127*, 3298.
(18) Jiang, Y.; Zhu, Y.-J. *J. Phys. Chem. B* **2005**, *109*, 4361.
(19) Wang, Y.; Yang, H. *J. Am. Chem. Soc.* **2005**, *127*, 5316.
(20) Liu, Z.; Sun, Z.; Han, B.; Zhang, J.; Huang, J.; Du, J.; Miao, S. *J. Nanosci. Nanotechnol.* **2006**, *6*, 175.
(21) Gao, S.; Zhang, H.; Wang, X.; Mai, W.; Peng, C.; Ge, L. *Nanotechnology* **2005**, *16*, 1234.
(22) Antonietti, M.; Kuang, D.; Smarsly, B.; Zhou, Y. *Angew. Chem., Int. Ed.* **2004**, *43*, 4988.
(23) Neve, F.; Crispini, A.; Armentano, S. *Chem. Mater.* **1998**, *10*, 1904.

(24) Neve, F.; Francescangeli, O.; Crispini, A.; Charmant, J. *Chem. Mater.* **2001**, *13*, 2032.
(25) Neve, F.; Francescangeli, O.; Crispini, A. *Inorg. Chim. Acta* **2002**, *338*, 51.
(26) Neve, F.; Imperor-Clerc, M. *Liq. Cryst.* **2004**, *31*, 907.
(27) Neve, F.; Francescangeli, O. *Cryst. Growth Des.* **2005**, *5*, 163.
(28) Lee, C. K.; Peng, H. H.; Lin, I. J. B. *Chem. Mater.* **2004**, *16*, 530.
(29) Bowlas, C. J.; Bruce, D. W.; Seddon, K. R. *Chem. Commun.* **1996**, 1625.
(30) Gordon, C. M.; Holbrey, J. D.; Kennedy, A. R.; Seddon, K. R. *J. Mater. Chem.* **1998**, *8*, 2627.
(31) Holbrey, J. D.; Seddon, K. R. *J. Chem. Soc., Dalton Trans.* **1999**, 2133.
(32) Carmichael, A. J.; Hardacre, C.; Holbrey, J. D.; Nieuwenhuyzen, M.; Seddon, K. R. *Mol. Phys.* **2001**, *99*, 795.
(33) Hardacre, C.; Holbrey, J. D.; McCormac, P. B.; McMath, S. E. J.; Nieuwenhuyzen, M.; Seddon, K. R. *J. Mater. Chem.* **2001**, *11*, 346.
(34) Bowers, J.; Butts, C. P.; Martin, P. J.; Vergara-Gutierrez, M. C.; Heenan, R. K. *Langmuir* **2004**, *20*, 2191.
(35) Yoshio, M.; Mukai, T.; Ohno, H.; Kato, T. *J. Am. Chem. Soc.* **2004**, *126*, 994.
(36) Firestone, M. A.; Dzielawa, J. A.; Zapol, P.; Curtiss, L. A.; Seifert, S.; Dietz, M. L. *Langmuir* **2002**, *18*, 7258.
(37) Yoshio, M.; Mukai, T.; Kanie, K.; Yoshizawa, M.; Ohno, H.; Kato, T. *Chem. Lett.* **2002**, 320.
(38) Binnemans, K. *Chem. Rev.* **2005**, *105*, 4148.
(39) Dupont, J. *J. Braz. Chem. Soc.* **2004**, *15*, 341.
(40) Taubert, A. *Angew. Chem., Int. Ed.* **2004**, *43*, 5380.
(41) Taubert, A.; Arbell, I.; Mecke, A.; Graf, P. *Gold Bull.* **2006**, *39* (4), 205.
(42) Dobbs, W.; Suisse, J.-M.; Douce, L.; Welter, R. *Angew. Chem., Int. Ed.* **2006**, *45*, 4179.
(43) Lee, C. K.; Vasam, C. S.; Huang, T. W.; Wang, H. M. J.; Yang, R. Y.; Lee, C. S.; Lin, I. J. B. *Organometallics* **2006**, *25*, 3768.
(44) Zhu, H.; Huang, J.-F.; Pan, Z.; Dai, S. *Chem. Mater.* **2006**, *18*, 4473.
(45) Kim, K.-S.; Choi, S.; Cha, J.-H.; Yeon, S.-H.; Lee, H. *J. Mater. Chem.* **2006**, *16*, 1315.
(46) Taubert, A.; Steiner, P.; Mantion, A. *J. Phys. Chem. B* **2005**, *109*, 15542.
(47) Schmitt, B.; Brönnimann, C.; Eikenberrya, E. F.; Gozzo, F.; Hörmann, C.; Horisberger, C.; Patterson, B. *Nucl. Instrum. Methods Phys. Res., Sect. A* **2003**, *501*, 267.

In the two next publications, light scattering proved to be a useful tool in the characterization of vesicles. In the first case, the relatively large size distribution of the vesicles (radii ranging from 50 to 110 nm according to TEM) prevented from using the vesicle form factor when analyzing the SLS data. We therefore used the standard Zimm plot (Figure 27), i.e. the random coil form factor. This yielded a mean radius of gyration equal to the hydrodynamic radius obtained by DLS, which is characteristic of vesicles.

In the second case, the relatively narrow size distribution of the vesicles (radius of 118 nm with a polydispersity index of 1.08) made possible the use of the vesicle form factor when analyzing the SLS data. The vesicle membrane thickness was estimated from TEM and literature, then the Rayleigh ratios were fitted against molar mass, second virial coefficient and outer geometrical radius.

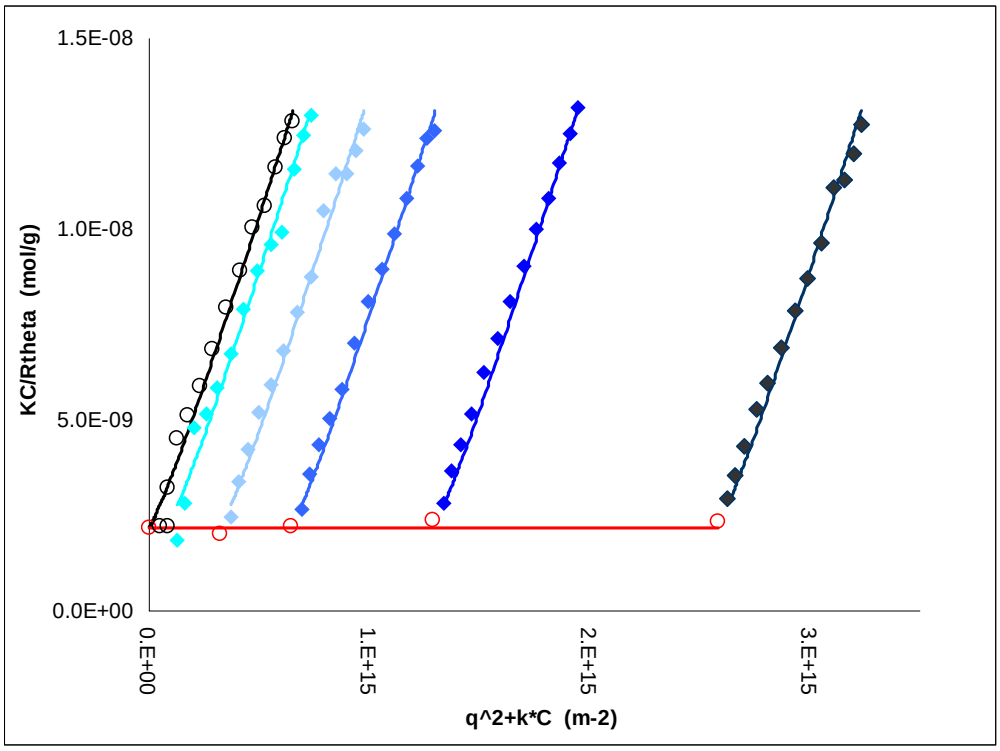

Figure 27. Zimm plot of poly-(2-methyloxazoline)-poly(dimethylsiloxane)-poly(2-methyloxazoline) vesicles (lines are simulated data).

2. Antioxidant Nanoreactor based on Superoxide Dismutase Encapsulated in Superoxide-Permeable Vesicles[143]

3. Amphiphilic Diblock Copolymers for Molecular Recognition: Metal-NTA Functionalized Vesicles[144]

THE JOURNAL OF PHYSICAL CHEMISTRY B

 VOLUME 112, NUMBER 28, JULY 17, 2008

ARTICLES

Antioxidant Nanoreactor Based on Superoxide Dismutase Encapsulated in Superoxide-Permeable Vesicles

Fabian Axthelm,[†] Olivier Casse,[†] Willem H. Koppenol,[‡] Thomas Nauser,[‡] Wolfgang Meier,[†] and Cornelia G. Palivan*,[†]

Department of Chemistry, University of Basel, Klingelbergstrasse 80, CH-4056 Basel, Switzerland, and Institute of Inorganic Chemistry, Department of Chemistry and Applied Bioscience, ETH, CH-8093 Zurich, Switzerland

Received: April 8, 2008; Revised Manuscript Received: April 21, 2008

We designed and tested an antioxidant nanoreactor based on encapsulation of Cu,Zn superoxide dismutase in amphiphilic copolymer nanovesicles, the membranes of which are oxygen permeable. The nanovesicles, made of poly(2-methyloxazoline)−poly(dimethylsiloxane)−poly(2-methyloxazoline), successfully encapsulated the protein during their self-assembling process, as proved by confocal laser-scanning microscopy and fluorescence-correlation spectroscopy. Electron paramagnetic resonance spectroscopy and circular dichroism analyses showed that no structural changes appeared in the protein molecules once inside the inner space of the nanovesicles. The function of this antioxidant nanoreactor was tested by pulse radiolysis, which demonstrated that superoxide dismutase remains active inside the nanovesicles and detoxifies the superoxide radical in situ. The membrane of our triblock copolymer nanovesicles plays a double role, both to shield the sensitive protein and to selectively let superoxide and dioxygen penetrate to its inner space. This simple and robust hybrid system provides a selective shielding of sensitive enzymes from proteolytic attack and therefore a new direction for developing drug delivery applications.

Introduction

Efficient strategies for the regulation of partially reduced oxygen species (PROS), including cellular antioxidants, such as glutathione and ascorbate, and enzymes, such as glutathione peroxidase, glutathione transferases, catalase, and superoxide dismutase (SOD), exist in living cells. In certain pathologies, the production of PROS overwhelms cellular antioxidant defense mechanisms leading to oxidative stress. PROS, which include the superoxide radical anion ($O_2^{\bullet -}$), peroxynitrite, the hydroxyl radical, and hydrogen peroxide, are constantly produced in living organisms and are involved in the initiation and progression of chronic inflammation. Oxidative stress has been shown to play a significant role in many disease states including arthritis, Parkinson's disease, amyotrophic lateral sclerosis, cancer, and AIDS.[1–4]

Cu,Zn-SOD is known to decrease the steady-state concentration of superoxide radicals and could be a suitable candidate drug; it is, however, quickly eliminated from the bloodstream (6 min in rats and 30 min in humans)[5] and poorly adsorbed from and rapidly degraded in the gastrointestinal tract,[4] thereby compromising its delivery. Attempts have been made to improve delivery by protecting the protein (i) with the hydroxyl radical

* E-mail: Cornelia.Palivan@unibas.ch.
[†] University of Basel.
[‡] ETH Zurich.

10.1021/jp803032w CCC: $40.75
Published on Web 06/21/2008

scavengers homocarnosine or anserine,[6] (ii) by covalent modification with polyethylene glycol (PEG)[7] or sodium chondroitin sulfate,[8] and (iii) by encapsulation into liposomes.[9–11] Although modification with PEG represents one of the most conventional ways to protect an enzyme from proteolytic attack, excessive covalent modification can compromise activity.[12] Likewise, encapsulation of SOD into liposomes has serious drawbacks, such as significant leakage due to structural defects,[13] mechanical instability, interaction with high-density lipoproteins,[14] and a short circulation lifetime.[15]

Another way, which emerged these last years, for protection of sensitive proteins consists in shielding the protein in polymeric carriers that contain an internal space; the system of cage and encapsulated protein has been named a nanoreactor if the protein is acting in situ.[16,17] Various types of polymerosome nanoreactors have been developed, either by changing the nature and the combination of block copolymers or to address different applications based on an enzyme or combination of enzymes.[18–20] Unlike liposome-based carriers, the polymeric vesicles have morphologies and properties that may be controlled by the high diversity of block copolymers. This approach allows the variation of the chemical constitution, length of different blocks, or molecular architecture of the whole copolymer, which makes them more versatile for a wider range of applications.[21] A simple and robust approach to prepare polymeric drug carriers is to use amphiphilic copolymers which self-assembly in aqueous solutions into vesicular structures. In a fashion analogous to that for lipids.[22]They consist of spherical closed block-copolymer membranes with diameters in the range from 50 nm to approximately 10 μm, depending on the chemical constitution, size of polymer blocks, preparation method, and reaction conditions.[23] The polymer vesicles thus obtained are significantly more stable against lysis by classical surfactants than liposomes because of the low entropy of mixing of polymers while preserving the low immunogenicity.[24,25] In addition, the vast amount of available blocks makes it possible to tune their properties, such as wall thickness, polarity, toxicity, or sensor-responsivity.[16,26] To the best of our knowledge, as yet, no nanoreactors that function as antioxidants have been proposed. There have been attempts to encapsulate SOD in polymeric carriers, but in the conventional approach of drug delivery, the enzyme acts only after its release from the carrier.[27,28]

We propose here a new strategy to detoxify the $O_2^{\bullet-}$ based on encapsulation of Cu,Zn-SOD in oxygen-permeable nanovesicles formed by self-assembly of amphiphilic triblock copolymer. Herein, we describe the design and analysis of antioxidant nanoreactors prepared from poly(2-methyloxazoline)−poly(dimethylsiloxane)−poly(2-methyloxazoline), PMOX−PDMS−PMOXA,[29] that encapsulates Cu,Zn-SOD as shown in Figure 1. The chosen block copolymers have a proven record of good biocompatibility,[30] and the hydrophilic PMOXA block shows low nonspecific protein binding ability.[31] The polymer membrane of these nanovesicles is stable and impermeable to saccharide ions and water[32] and demonstrates none of the sort of organizational defects responsible for the known instability of liposomal drug carriers.[13] Our nanoreactor is not limited to use with SOD; any compound or combination of compounds having antioxidant properties may be encapsulated.

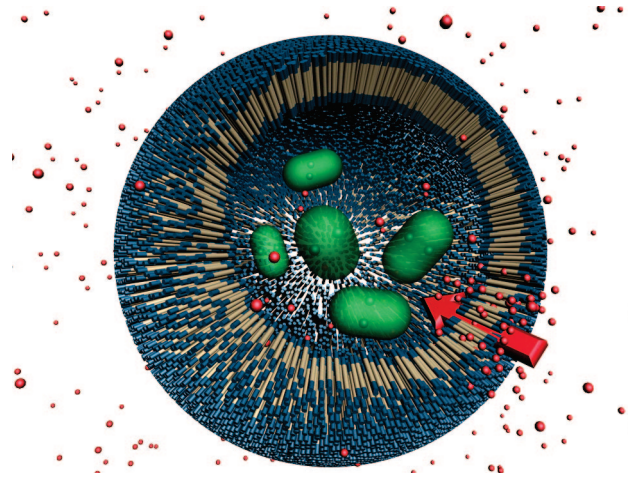

Figure 1. Schematic representation of an antioxidant nanoreactor with encapsulated SOD. The $O_2^{\bullet-}$ is able to penetrate the polymeric shield.

Materials and Methods

Materials. Cu,Zn-SOD from bovine erythrocytes (Sigma Aldrich), Alexa Fluor 488 (Invitrogen), dimethylsulfoxide (DMSO; Aldrich), Sephadex G-50 (Fluka), and ethanol (99.8%; Fluka) were used without any further treatment. Sepharose 4B (Sigma Aldrich) and polycarbonate membrane filters (Millipore, 200 nm) were used. Alexa Fluor 488 (Invitrogen) was used as described in the manufacturer's protocol (MP00143, http://www.invitrogen.com).

Nanovesicle Preparation. The synthesis of $PMOXA_n-PDMS_m-PMOXA_n$ (where $n = 15$ and $m = 110$), has been described elsewhere.[32] Nanovesicles were prepared according to a modification of a previously published method.[33] The triblock copolymer $PMOXA_{15}-PDMS_{110}-PMOXA_{15}$ (50 mg) was dissolved in ethanol at 17% (w/w) and stirred at room temperature for 1 h. After complete dissolution, this solution was slowly added dropwise to phosphate-buffered saline (PBS) buffer to give a final polymer concentration of 10 mg/mL, and the mixture was stirred overnight at room temperature. The solution was then extruded 20 times through a polycarbonate membrane filter (Millipore) with a well-defined pore size of 200 nm to decrease the size polydispersity of vesicles.[33] Subsequently, the extruded solution was purified by size-exclusion chromatography (SEC) on Sepharose 4B (10 × 300 mm).

Fluorescence Labeling of SOD. Fluorescently labeled SOD was obtained by reaction of Alexa Fluor 488 with the primary amines of the protein. Labeled SOD was separated from unbound Alexa Fluor 488 by SEC on Sephadex G50 (10 × 300 mm) equilibrated with PBS buffer. The concentration of labeled protein in solution was determined by pulse radiolysis.[34] The number of Alexa Fluor 488/SOD molecule was determined by fluorescence corelation spectroscopy.

Encapsulation of Fluorescently Labeled SOD in Nanovesicles. Encapsulated SOD was obtained by adding the polymer solution as described above to a solution of labeled SOD (0.26 mg/mL) in PBS buffer. The nonencapsulated protein was removed by size exclusion chromatography on a Sepharose 4B column, with the same buffer. To determine whether the protein can be attacked from outside the vesicles, a stock solution of 20 mg/mL of proteinase K (Roche) was added to the solution of encapsulated, fluorescently labeled SOD at 5% (v:v), and the mixture was incubated for 4 h at room temperature.

Light Scattering. Dynamic (DLS) and static (SLS) light-scattering experiments to determine the sizes and size distribution of empty and SOD-containing polymeric nanovesicles were performed on a ALV (Langen, Germany) goniometer, equipped with an ALV He−Ne laser ($\lambda = 632.8$ nm). SOD-encapsulated

and empty nanovesicles were prepared by serial dilution to polymer concentrations ranging from 3.33 to 0.1 mg/mL. Light scattering was measured in 10 mm cylindrical quartz cells at angles of 30−150° at 293 K. The data for DLS were analyzed by using a Williams−Watts function.[35] The size polydispersity of the vesicles was determined according to the literature.[36–38]

Transmission Electron Microscopy (TEM). Nanovesicle dispersions (empty vesicles and vesicles containing encapsulated SOD-Alexa Fluor 488) were negatively stained with 2% uranyl acetate solution and deposited on a carbon-coated copper grid. The samples were examined with a transmission electron microscope (Philips Morgagni 268D) at 293 K.

Laser-Scanning Microscopy/Fluorescence-Correlation Spectroscopy. Laser-scanning microscopy (LSM) and fluorescence-correlation spectroscopy (FCS) measurements were obtained with a Zeiss LSM 510-META/Confcor2 laser-scanning microscope equipped with an argon laser (488 nm) and a 40× water-immersion objective (Zeiss C/Apochromat 40X, NA 1.2), with the pinhole adjusted to 70 μm. Solutions of polymeric nanoreactors (2−3 mg/mL) with encapsulated SOD-Alexa Fluor 488 were measured at room temperature in special chambered quartz-glass holders (Laboratory-Tek; 8-well, NUNC A/S) that provide optimal conditions for imaging while reducing evaporation of the aqueous solutions. In LSM mode, appropriate filters were chosen, and the detector gain, amplifier gain, and offset were adjusted to optimize micrograph quality; images (512 × 512 pixels) were collected with a scan speed of 0.96 s/pixel at 8-bit color depth. In FCS mode, intensity fluctuations were analyzed in terms of an autocorrelation function with the LSM 510/Confocor software package (Zeiss, AG). Spectra were recorded over 30 s, and each measurement was repeated 10 times; results are reported as the average of three independent experiments. Adsorption and bleaching effects were reduced by exchanging the sample droplet after 5 min of measurement. The excitation power of the Ar laser was $P_L = 15$ mW, and the excitation transmission at 488 nm was 2%. To reduce the number of free fitting parameters, the diffusion times for free dye (Alexa Fluor 488) as well as the labeled SOD were independently determined and fixed in the fitting procedure.

Circular Dichroism. Circular dichroism (CD) spectra (180−260 nm) were recorded to determine the impact of the labeling and encapsulation conditions on the SOD molecule. Measurements were made with an Applied Photophysics Chirascan CD spectrometer. Encapsulated SOD-Alexa Fluor 488 collected from the SEC purification step was treated with a centrifugal filter device (Centricon YM-10, Millipore, 10 kDa nominal molecular weight cutoff) at 5000 g to exchange the PBS buffer with MilliQ water (18 MΩ cm; Purelab UHQ, Elga) and compared with unlabeled SOD solubilized in MilliQ water.

Electron Paramagnetic Resonance Spectroscopy. Electron paramagnetic resonance (EPR) spectra were recorded at 77 K with a CW Bruker ElexSys500 X-band CW spectrometer, equipped with a helium temperature control system (ER4112HV), to which the resonance cavity was attached. Microwave power was adjusted at levels below the saturation condition (2 mW for high-field measurements and 10 mW for low-field measurements). The modulation frequency was 100 kHz, and the modulation amplitude was 0.5 mT; other spectral parameters were adjusted for each spectrum individually. Multiple (150) spectra were acquired to optimize the signal-to-noise ratio, and third-order polynomial averaging was used for subsequent noise reduction. The spectral parameters were obtained with the SIMFONIA software package (Bruker Instruments Inc., Manning Park, Billerica, MA), where coaxial g and hyperfine tensors were assumed. Gaussian line shapes were considered with the line width adjusted for each spectrum. All spectral simulations assumed natural abundance ratios of Cu isotopes. The g values were referenced to diphenylpicryhydrazyl (DPPH, $g = 2.0036$) as an external standard.

TABLE 1: LS Characterization of Empty and SOD-Containing Vesicles

sample	R_g [nm]	R_H [nm]	M [10^8g/mol][a]	A2 [mol/L/g^2][b]
empty vesicles	150 ± 7	156	4.7	5.1×10^{-11}
SOD-containing vesicles	140 ± 10	149	3.4	1.3×10^{-11}

[a] M, weight-average molar mass. [b] A2, second virial coefficient.

SOD Activity Assay. The activity of SOD in the polymeric nanovesicles was investigated by pulse radiolysis with a Febetron 705 (Titan Systems Corp., San Leandro, CA, USA) 2.3 MeV accelerator with a pulse width (fwhm) <50 ns as the radiation source; the optical system consists of a 75 W Xe arc lamp (Hamamatsu, Schüpfen, Switzerland), a 1 or 2 cm optical path quartz cell (Hellma GmbH and Co. KG, Müllheim, Germany), and an Acton SP300i monochromator (Roper Scientific, Ottobrunn, Germany). For signal detection of kinetic traces, a R928 photomultiplier (Hamamatsu) with a DHPCA-200 amplifier (Femto Messtechnik GmbH, Berlin, Germany) with a DL7100 digital storage oscilloscope (Yokogawa Electric Corporation, Tokyo, Japan) is used; a Princeton Instruments PI-MAX 512T gateable ICCD camera (Roper Scientific) is used for detection of time-resolved spectra. $O_2^{\bullet-}$ is formed by irradiation of oxygenated sodium formate (1 M) solutions at pH 8.5. SOD activity is calculated from rates of decay of $O_2^{\bullet-}$, measured at 280 nm, in the presence and absence of SOD. Doses between 10 and 50 Gy/pulse were applied. When experiments with vesicles are carried out, extensive light scattering is observed, which results in a lower signal amplitude. The 100 Hz ripple is caused by the electronic equipment.

Results and Discussion

Formation and Stability of PMOXA−PDMS−PMOXA Vesicles. It has been shown that amphiphilic triblock copolymer PMOXA−PDMS−PMOXA self-assembles spontaneously in dilute aqueous solutions into vesicular structures.[32] Dilute solutions of $PMOXA_{15}-PDMS_{110}-PMOXA_{15}$ form self-assembled nanostructures without encapsulated SOD, which were characterized by TEM, SLS, and DLS experiments. TEM of self-assembled nanostructures of polymer shows circular objects with radii ranging from 50 to 110 nm, in good agreement with results obtained from cryo TEM, which indicated nanovesicles with a radius of 117 nm.[32] TEM measurements repeated after long-term (>3 weeks) storage at 4 °C did not reveal any significant changes, suggesting that the nanovesicles from $PMOXA_{15}-PDMS_{110}-PMOXA_{15}$ are chemically stable.

The LS results are presented in Table 1. We calculate a ratio ($\rho = R_g/R_H$) of the radius of gyration (R_g), obtained from SLS, to the hydrodynamic radius (R_H), from DLS experiments, of 0.96, which is characteristic for hollow spherical objects. On the basis of the assumption of a one-component population, the mean radius of these vesicles is about 150 nm. This larger value is expected, as the R_H from DLS experiments is the sum of the particle and its surrounding hydration sphere.

Formation of PMOXA−PDMS−PMOXA Vesicles with Encapsulated SOD. Nanovesicles prepared with SOD encapsulated were characterized by TEM and LS and compared with empty vesicles. The TEM images for SOD-containing nanoves-

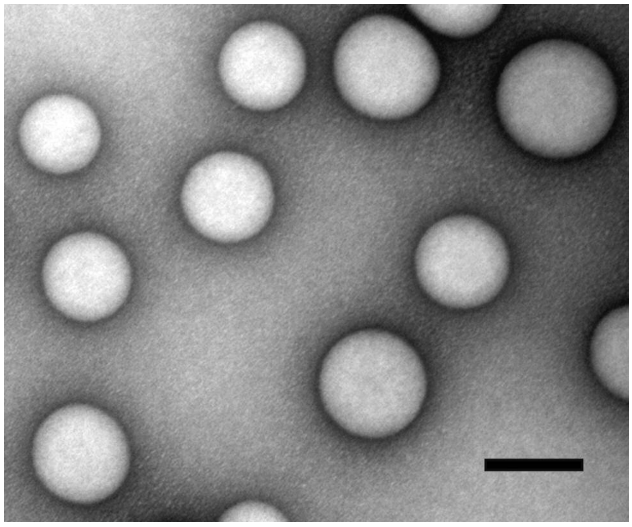

Figure 2. Transmission electron micrograph of SOD-encapsulated in $PMOXA_{15}-PDMS_{110}-PMOXA_{15}$ vesicles (room temperature; scale bar = 200 nm).

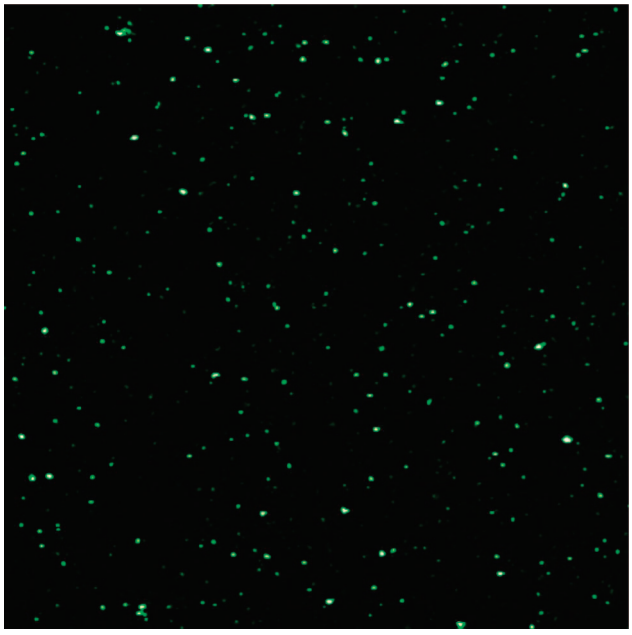

Figure 3. CLSM micrograph of SOD-Alexa Fluor 488 encapsulated in $PMOXA_{15}-PDMS_{110}-PMOXA_{15}$ polymeric nanovesicles.

icles (Figure 2) were essentially identical to those for empty vesicles; additionally, we find a the ratio of $\rho = 0.93$ from SLS and DLS experiments. Taken together, these results indicate that the encapsulation of SOD during the autoassembly process does not influence nanovesicle formation in terms of size or stability.

To investigate whether the protein is located in the inner space of the nanovesicles, a configuration essential for its shielding, we analyzed nanovesicles prepared with encapsulated SOD, labeled with the fluorescence probe Alexa488, by confocal LSM (CLSM) and FCS. CLSM micrographs of encapsulated SOD-Alexa Fluor 488 display a strong fluorescence signal (Figure 3). To verify whether the protein interacts with the surface of the nanovesicles, we examined a purified mixture of empty nanovesicles and free SOD-Alexa Fluor 488 by CLSM. As this purified mixture did not show any fluorescence signal, we conclude that nonspecific interaction between the surface of the empty nanovesicles and the labeled SOD are negligible (data not shown) and that the intense fluorescent signals shown in

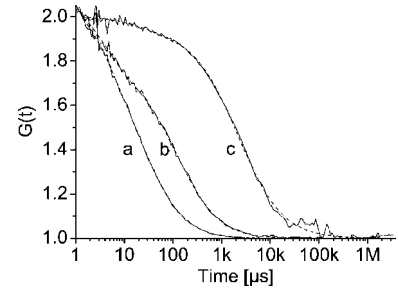

Figure 4. FCS autocorrelation curves. (a) Solution of Alexa Fluor 488 (4×10^{-6} mg/mL) in PBS buffer. (b) Solution of SOD-Alexa Fluor 488 (6×10^{-6} mg/mL) in PBS buffer. (c) Solution of SOD-Alexa Fluor 488 encapsulated in polymeric nanovesicles of $PMOXA_{15}-PDMS_{110}-PMOXA_{15}$. Curves normalized to 2 to facilitate comparison.

the micrograph in Figure 3 are solely from labeled SOD located in the aqueous cavities of the nanovesicles. This is in agreement with previous findings which indicate that the container wall is completely covered by PMOXA chains and shows a very low nonspecific protein binding.[31]

We used FCS to examine in more detail the encapsulation of SOD in nanovesicles, by measuring free Fluor Alexa 488, nonencapsulated SOD-Alexa Fluor 488, and encapsulated SOD-Alexa Fluor 488. In FCS, a special fluctuation correlation approach is applied, in which the laser-induced fluorescence of the excited fluorescent molecules that pass through a very small probe volume is autocorrelated in time to give information about the diffusion times of the molecules. According to the Stokes−Einstein equation, the diffusion times, which are proportional to the R_H of the fluorescent molecules, provide information about interactions of the fluorescent molecules with larger target molecules, including encapsulation of protein in some nanovesicles.[38] The results are presented in Figure 4; autocorrelation amplitudes are normalized to 2 to facilitate comparison of diffusion times and the shapes of the curves. The diffusion time (τ_d) for free Alexa Fluor 488 at room temperature is 23 μs (Figure 4, curve a). For nonencapsulated SOD-Alexa Fluor 488, $\tau_d = 104$ μs, which corresponds to $R_H = 2.4$ nm, in good agreement with the radius of 2.2 nm calculated on the basis of the molecular mass (33 kDa) of SOD-Alexa Fluor 488 (Figure 4, curve b). For encapsulated SOD-Alexa Fluor 488, the multiphasic curve (Figure 4, curve c) indicates the presence of slowly diffusing particles. This population with a reduced diffusion ($\tau_d = 2.3$ ms) represents more than 78% of the total number of fluorescent particles that passes the confocal volume during the measurement time of 30 s and corresponds to vesicles that encapsulate SOD-Alexa Fluor 488. The best fit of the autocorrelation function of the time-dependent fluorescence signal indicates that the remaining diffusing fluorescent particles correspond to free Alexa 488 molecules, which have been encapsulated in vesicles or have not been completely removed from the solution and are detected because of their high quantum yield and the extremely high sensitivity of FCS.[39]

To estimate the number of SOD molecules encapsulated in the nanovesicles, we compared the molecular brightness, reported as count rates per molecule (cpm, in kHz) of free Alexa Fluor 488, nonencapsulated SOD-Alexa Fluor 488, and encapsulated SOD-Alexa Fluor 488. We found that one Alexa Fluor 488 is attached to one SOD molecule by using a calibration curve of molecular fluorescence intensity as function of the known concentrations of Alexa Fluor 488. SOD-Alexa Fluor 488 in the presence of a polymer environment exhibited less

molecular brightness (cpm = 27 kHz) than free Alexa Fluor 488 (cpm = 42 kHz), the difference being mostly attributed to quenching of the dye.[40] In the case of encapsulated SOD-Alexa Fluor 488, the total molecular brightness (cpm_T) corresponds to the weighted sum of the brightnesses of the individual components (cpm_i). By comparing the molecular brightness of the encapsulated SOD-Alexa Fluor 488 solutions with that of the free labeled protein in the presence of polymer, we estimate that an average of 2−5 SOD-Alexa Fluor 488 molecules are encapsulated per nanovesicle when the initial concentration of SOD-Alexa Fluor 488 was 0.1−0.27 mg/mL. This is in agreement with the average number of encapsulated SOD molecules that can be calculated from the initial concentrations of SOD together with the total volume of the inner spaces of the vesicles.The inclusion is a statistical process in which the number of encapsulated molecules is determined by the starting concentrations of the protein. Under the experimental conditions applied, the number of encapsulated SOD molecules is small, as we intended to minimize interactions and functional changes due to confinement in the nanovesicles. In addition, by encapsulating only a small number of SOD molecules, we tested the sensitivity of the nanoreactor, a prerequisite for further therapeutic applications. The study of enzymes at the level of one molecule has the potential to provide significant insight into the detailed spectrum of molecular conformational changes and activities.[41–44]

Structural Stability of PMOXA−PDMS−PMOXA Vesicles Containing SOD-Alexa Fluor 488. The block copolymer membranes can be regarded as mimetics of biological membranes, but they are thicker and far more stable than those of the liposomes.[37,45] To check the stability of the antioxidant nanoreactors, the nanovesicles with encapsulated SOD-Alexa Fluor 488 were reanalyzed by FCS after 3 weeks of storage at 4 °C; no release of encapsulated SOD was observed. Additionally, the LS measurements did not indicate any change in radius or size distribution of the nanoreactors over time (data not shown). This level of stability was expected because of the dimensions of Cu,Zn-SOD and the tightness of the polymer membrane (data not shown). As the vesicles are intended to shield SOD from proteolytic attack, we analyzed the FCS data of a solution of encapsulated SOD-Alexa Fluor 488 to which proteinase K was added in order to see whether the later can attack the encapsulated enzyme. The diffusion time of the vesicles that contain labeled SOD did not change when proteinase K was present, proving that our vesicles protect SOD against enzymatic attack.

Structural and Functional Integrity of the Nanoreactor. In order to investigate whether the encapsulation procedure denatures the protein, we checked for possible geometry changes of the Cu^{II} metal site of the protein by EPR, and characterized the protein's backbone structure by CD. In Cu,Zn-SOD, Cu^{II} is located at the enzyme active site, where it plays a role in the disproportionation of $O_2^{\bullet-}$ to dioxygen and hydrogen peroxide at near diffusion-controlled rates.[46]

It is possible to characterize the first coordination sphere around the metal ion by EPR, from the point of view of both geometry and identification of nuclei with nonzero spin, because the values of spin Hamiltonian parameters can be related to the various distortions of copper environment. Figure 5, curve a shows the frozen-solution EPR spectrum of the encapsulated protein, obtained after a multiple acquisition (more than 500 spectra) procedure. Its simulation derived from a third-order perturbation theory approach (Figure 5, curve b) provides the values of the gyromagnetic and hyperfine tensors: $g_\perp = 2.067$, $g_\parallel = 2.263$, $A_\perp = 4.1$ mT, and $A_\parallel = 13.9$ mT. These values, which are similar to those previously obtained for frozen solutions of bovine Cu,Zn-SOD,[47] indicate that the metal site is not affected by the encapsulation procedure. The metal-binding site of the oxidized form of wild-type Cu,Zn-SOD, as characterized by X-ray diffraction and EPR and electronic spectroscopy, shows the Cu^{II} ion to be five-coordinate, with four histidyl side chains in a tetrahedrally distorted arrangement and one axially situated water molecule.[46,48] Unfortunately, the multiple acquisition procedure required for the encapsulated enzyme impedes the use of either D2-EPR or pulse-EPR methods that would provide more information on the fine details of the coordination sphere of copper.[49]

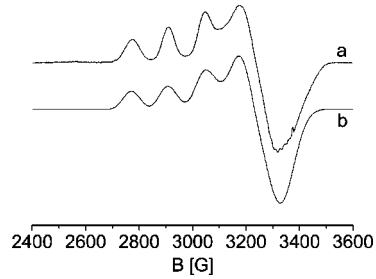

Figure 5. EPR spectra. (a) Cu,Zn-SOD encapsulated in nanovesicles of triblock copolymer $PMOXA_{15}$−$PDMS_{110}$−$PMOXA_{15}$, at 77 K. (b) Simulation derived from a third-order perturbation theory approach.

The CD spectra of SOD-Alexa Fluor 488 before and after being subjected to the encapsulation procedure (Figure S3, Supporting Information) differ only in signal intensity, which is due to sample concentrations. This indicates that if the encapsulation caused any changes to the protein backbone, these changes were reversible.[50]

We performed pulse-radiolysis measurements on series of free and encapsulated SOD samples to determine whether encapsulated SOD remains active. Cu,Zn-SOD is active across a wide functional pH range (5.0−9.5) and under various environmental conditions;[34,51,52] thus, we hypothesized that the protein would not be affected by the encapsulation procedure. Our hypothesis was supported by our observations that encapsulated SOD remains functionally intact. We have previously succeeded in encapsulating other proteins in nanovesicles, for example, β-lactamase and the purine-specific nucleoside hydrolase of *Trypanosoma ViVax* (TvNH), and found that activity was preserved.[53,54] In pulse radiolysis, the kinetics of the dismutation superoxide anions activity is measured directly; the method is sensitive (10 nM), accurate, and reproducible. Figure 6-1 shows the rate of dismutation of the superoxide anion in the presence of empty nanovesicles (curve a, $t_{1/2} \approx 300$ ms) compared to SOD-filled nanovesicles (curve b, $t_{1/2} \approx 4$ ms). The very rapid dismutation of superoxide anions in the presence of encapsulated SOD, together with the finding that SOD is present only in the inner space of the nanovesicles, demonstrates that the nanovesicles are permeable to superoxide and $HO_2^{\bullet}$ and may be described as nanoreactors. The in situ activity assays together with structural characterization of the protein establish that no changes to the protein occur during the encapsulation procedure. The reaction rate of the encapsulated enzyme is similar to that of the free enzyme, which indicates that the diffusion of $O_2^{\bullet-}$ through the triblock copolymer wall is not rate-limiting.

We constructed a calibration curve from a series of pulse-radiolysis determinations of the activity of free SOD in solution (Figure 6-2) and, by assuming free diffusion of superoxide, used the curve to calculate the amount of SOD encapsulated. By taking into account the number of nanovesicles formed in a

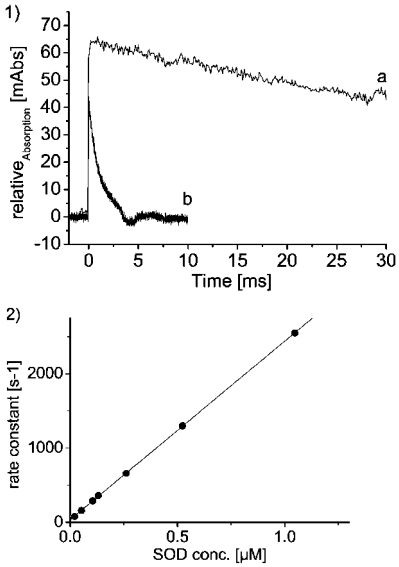

Figure 6. (1) Pulse-radiolysis assay. (a) Uncatalyzed decay observed at 280 nm of 80 μM superoxide produced by a 50 ns pulse of an aerated solution of 1.0 M formate and 10 mM phosphate, pH 8. (b) Superoxide decay catalyzed by SOD (ca. 0.12 μM) encapsulated in $PMOXA_{15}-PDMS_{110}-PMOXA_{15}$ vesicles (10 mg polymer). (2) Pulse-radiolysis standard curve for different concentrations of SOD.

solution of 10 mg/mL of polymer with a weight average molar mass $M = 3.4 \times 10^8$ g/mol (determined from LS experiments) and the concentration of encapsulated SOD (determined by pulse radiolysis), the average encapsulation number is 10 protein molecules/nanovesicle (for an initial concentration of SOD of 0.3 mg/mL). This value is slightly higher than the maximum average number of encapsulated SOD-Alexa Fluor 488 molecules obtained from molecular brightness measurements, where only labeled-SOD molecules are counted (nonlabeled protein molecules are invisible). We emphasize that within the experimental errors and inherent limitations of each method, the results of these two independent methods are in good agreement. Because of the small number of encapsulated SOD molecules, the intermolecular interactions or conformational changes due to confinement of SOD in the nanovesicles can be considered negligible. Because of the mild encapsulation that occurs during the self-assembly process of nanovesicle formation, as well as the experimental conditions aimed at restricting the number of enzyme molecules encapsulated, SOD remains fully active and the dismutation of superoxide takes place in the inner space of the nanoreactor.

According to studies of the permeability of bilayer lipid membranes to superoxide radicals, the transport of $O_2^{\bullet -}$ is strongly dependent on the structural state of the membrane and on the localization of the substrate; the permeability coefficient is estimated at $2.1 \times 10^{-6}-7.6 \times 10^{-8}$ cm/s in lipids.[55,56] Generally, for lipid bilayers, channels for anion transport must be incorporated, and the bilayers tend to break down and release encapsulated compounds over time. However, the polymeric nanoreactors described here are permeable to both dioxygen and superoxid and do not require anion channels.[16,17,54,57] Because the protein is acting inside the polymer vesicles, our nanoreactor is inherently simpler and avoids the problems connected to an efficient release in the body that are specific for conventional carriers, such as liposomes and other polymeric nanocontainers. The antioxidant nanoreactor is not limited to use with SOD; it can be chemically modified for specific targeting approaches and permits the simultaneous encapsulation of other proteins to extend its applicability.

Conclusion

We have designed and tested a novel antioxidant nanoreactor based on encapsulation of SOD in superoxide-permeable nanovesicles. The SOD encapsulated in block copolymer nanovesicles formed via self-assembly is located in the inner cavity of the nanovesicles, and the mild encapsulation process does not affect the structural or functional integrity of the enzyme. The polymeric membrane of the nanovesicles is capable of both protecting the encapsulated SOD and allowing penetration of the inner space by $O_2^{\bullet -}$, where the conversion to hydrogen peroxide and oxygen is catalyzed. Compared with conventional drug nanocarriers made of liposomes or polymers, our system combines the advantages of a polymer shield with an in situ active protein. The tight polymeric membrane of the nanovesicles prevents release of the encapsulated protein from the nanoreactor.[32] The sensitivity of this nanoreactor is high, as proved by the observation that SOD activity was measured although the number of encapsulated SOD molecules is small. The production of the nanoreactor is straightforward, involving simple self-assembly of the amphiphilic copolymer in the presence of the protein. The level of superoxide permeability obviates the necessity of inserting artificial channels in the polymer membrane, as usually done in nanoreactors.[16,17,54,57] The antioxidant nanoreactors remain stable over several weeks of storage at 4 °C. The selective permeability of the polymeric membrane may be generally useful to improve the bioavailability of proteinasceous pharmaceuticals.

Acknowledgment. This work was supported by the *Swiss National Science Foundation* (Project no. 200021-115956/1) and by Polyamphi, NCCR Nanosciences (MRTN-CT-2003-505027), and this is gratefully acknowledged. The authors thank Dr. P.L. Bounds from ETH Zurich for very useful discussions and for reading the manuscript. C.G.P. and F.A. thank M. Grzelakowski from Basel University for providing the polymer. C.G.P. wishes to thank EPR group at ETH Zurich for providing EPR facilities and Dr. S. K. Hillman for reading the manuscript.

Supporting Information Available: Figure S1 shows a transmission electron micrograph of empty $PMOXA_{15}-PDMS_{110}-PMOXA_{15}$ vesicles. Figure S2 shows a Zimm plot of polymer vesicles without encapsulated SOD. Figure S3 shows CD spectra of SOD-Alexa Fluor 488 separated from SOD-filled nanovesicles by SEC and SOD-Alexa Fluor 488 not exposed to the encapsulation conditions. This material is available free of charge via the Internet at http://pubs.acs.org.

References and Notes

(1) Beckman, J. S.; Koppenol, W. H. *Am. J. Physiol.* **1996**, *271*, C1424–37.

(2) Cabelli, D. E.; Riley, D.; Rodriguez, J. A.; Valentine, J. S.; Zhu, H. In *Biomimetic Oxidations Catalyzed by Transition Metal Complexes*; Meunier, B., Ed.; Imperial College Press/World Scientific: London, 2000; pp 461−508.

(3) Droege, W. *Oxidative Stress, Disease and Cancer;* **2006**, 885–895.

(4) Regnault, C.; Soursac, M.; Roch-Arveiller, M.; Postaire, E.; Hazebroucq, G. *Biopharm. Drug Dispos.* **1996**, *17*, 165–74.

(5) Jadot, G.; Vaille, A.; Maldonado, J.; Vanelle, P. *Clin. Pharmacokinet.* **1995**, *28*, 17–25.

(6) Kang, J. H.; Kim, K. S.; Choi, S. Y.; Kwon, H. Y.; Won, M. H.; Kang, T.-C. K. *Biochim. Biophys. Acta* **2002**, *1570*, 89–96.

(7) Maksimenko, A. V. *Curr. Pharm. Des.* **2005**, *11*, 2007–16.

(8) Maksimenko, A. V.; Tischenko, E. G. K. *Biochemistry* **1997**, *62*, 1163–1166.

(9) Corvo, M. L.; Boerman, O. C.; Oyen, W. J. G.; Jorge, J. C. S.; Cruz, M. E. M.; Crommelin, D. J. A.; Storm, G. K. *Pharm. Res.* **2000**, *17*, 600–606.

(10) Estevez, A. G.; Sampson, J. B.; Zhuang, Y. X.; Spear, N.; Richardson, G. J.; Crow, J. P.; Tarpey, M. M.; Barbeito, L.; Beckman, J. S. *Free Radical Biol. Med.* **2000**, *28*, 437–446.
(11) Rengel, R. G.; Filipovic-Grcic, J.; Cepelak, I.; Zanic-Grubisic, T.; Barisic, K. K. *Eur. J. Pharm. Biopharm.* **2005**, *60*, 47–51.
(12) Saifer, M. G. P.; Somack, R.; Williams, L. D. *Adv. Exp. Med. Biol.* **1994**, *366*, 377–87.
(13) Barenholz, Y. *Curr. Opin. Colloid Interface Sci.* **2001**, *6*, 66–77.
(14) Fonseca, M. J.; Alsina, M. A.; Reig, F. *Biochim. Biophys. Acta* **1996**, *1279*, 259–65.
(15) Fidler, I. J.; Raz, A.; Fogler, W. E.; Kirsh, R.; Bugelski, P.; Poste, G. *Cancer Res.* **1980**, *40*, 4460–6.
(16) Vriezema, D. M.; Aragones, M. C.; Elemans, J. A. A. W.; Cornelissen, J. J. L. M.; Rowan, A. E.; Nolte, R. J. M. *Chem. Rev.* **2005**, *105*, 1445–1489.
(17) Vriezema, D. M.; Hoogboom, J.; Velonia, K.; Takazawa, K.; Christianen, P. C. M.; Maan, J. C.; Rowan, A. E.; Nolte, R. J. M. *Angew. Chem., Int. Ed.* **2003**, *42*, 772–776.
(18) Choi, H.-J.; Montemagno, C. D. *Nano Lett.* **2005**, *5*, 2538–2542.
(19) Kishimura, A.; Koide, A.; Osada, K.; Yamasaki, Y.; Kataoka, K. *Angew. Chem., Int. Ed.* **2007**, *46*, 6085–6088.
(20) Vriezema, D. M.; Garcia, P. M. L.; Oltra, N. S.; Natzakis, N. S.; Kuiper, S. M.; Nolte, R. J. M.; Rowan, A. E.; van Hest, J. C. M. *Angew. Chem., Int. Ed.* **2007**, *46*, 7378–7382.
(21) Discher, D. E.; Eisenberg, A. *Science* **2002**, *297*, 967–973.
(22) Herrero-Vanrell, R.; Rincon, A. C.; Alonso, M.; Reboto, V.; Molina-Martinez, I. T.; Rodriguez-Cabello, J. C. *J. Controlled Release* **2005**, *102*, 113–122.
(23) Kita-Tokarczyk, K.; Grumelard, J.; Haefele, T.; Meier, W. *Polymer* **2005**, *46*, 3540–3563.
(24) Antonietti, M.; Foerster, S. *Adv. Mater.* **2003**, *15*, 1323–1333.
(25) Discher, B. M.; Won, Y.-Y.; Ege, D. S.; Lee, J. C. M.; Bates, F. S.; Discher, D. E.; Hammer, D. A. *Science* **1999**, *284*, 1143–1146.
(26) Palivan, C. G.; Vebert, C.; Axthelm, F.; Meier, W. *Nanotechnol. Biol. Med.* **2007**, 32/1–32/26.
(27) Giovagnoli, S.; Luca, G.; Casaburi, I.; Blasi, P.; Macchiarulo, G.; Ricci, M.; Calvitti, M.; Basta, G.; Calafiore, R.; Rossi, C. *J. Controlled Release* **2005**, *107*, 65–77.
(28) Lee, S.; Yang, S. C.; Heffernan, M. J.; Taylor, W. R.; Murthy, N. *Bioconjug. Chem.* **2007**, *18*, 4–7.
(29) Hirt, T.; Baron, R. C.; Lohmann, D.; Meier, W. P. Novartis, Zwitzerland;Application: US patent, 2000.
(30) Broz, P.; Benito Samantha, M.; Saw, C.; Burger, P.; Heider, H.; Pfisterer, M.; Marsch, S.; Meier, W.; Hunziker, P. *J. Controlled Release* **2005**, *102*, 475–88.
(31) Woodle, M. C.; Engbers, C. M.; Zalipsky, S. *Bioconjug. Chem.* **1994**, *5*, 493–6.
(32) Kumar, M.; Grzelakowski, M.; Zilles, J.; Clark, M. M.; Meier, W. *Proc. Natl. Acad. Sci. U. S. A.* **2007**, *104*, 20723–8.
(33) Nardin, C.; Hirt, T.; Leukel, J.; Meier, W. *Langmuir* **2000**, *16*, 1035–1041.
(34) Michel, E.; Nauser, T.; Sutter, B.; Bounds, P. L.; Koppenol, W. H. *Arch. Biochem. Biophys.* **2005**, *444*, 76.
(35) Williams, G.; Watts, D. C.; Dev, S. B.; North, A. M. *Trans. Faraday Soc.* **1971**, *67*, 1323–35.
(36) Van Zanten, J. H. *Surfactant Sci. Ser.* **1996**, *62*, 239–294.
(37) Nardin, C.; Winterhalter, M.; Meier, W. *Langmuir* **2000**, *16*, 7708–7712.
(38) Rigler, P.; Meier, W. K. *J. Am. Chem. Soc.* **2006**, *128*, 367–373.
(39) Schwille, P.; Korlach, J.; Webb, W. W. *Cytometry* **1999**, *36*, 176–182.
(40) Rajagopalan, P. T. R.; Zhang, Z.; McCourt, L.; Dwyer, M.; Benkovic, S. J.; Hammes, G. G. *Proc. Natl. Acad. Sci. U. S. A.* **2002**, *99*, 13481–13486.
(41) Comellas-Aragones, M.; Engelkamp, H.; Claessen, V. I.; Sommerdijk, N. A. J. M.; Rowan, A. E.; Christianen, P. C. M.; Maan, J. C.; Verduin, B. J. M.; Cornelissen, J. J. L. M.; Nolte, R. J. M. *Nat. Nanotechnol.* **2007**, *2*, 635–639.
(42) Flomenbom, O.; Velonia, K.; Loos, D.; Masuo, S.; Cotlet, M.; Engelborghs, Y.; Hofkens, J.; Rowan, A. E.; Nolte, R. J. M.; Van der Auweraer, M.; De Schryver, F. C.; Klafter, J. *Proc. Natl. Acad. Sci. U. S. A.* **2005**, *102*, 2368–2372.
(43) Roeffaers, M. B. J.; De Cremer, G.; Uji-i, H.; Muls, B.; Sels, B. F.; Jacobs, P. A.; De Schryver, F. C.; De Vos, D. E.; Hofkens, J. *Proc. Natl. Acad. Sci. U. S. A.* **2007**, *104*, 12603–12609.
(44) Boukobza, E.; Sonnenfeld, A.; Haran, G. *J. Phys. Chem. B* **2001**, *105*, 12165–12170.
(45) Bermudez, H.; Brannan, A. K.; Hammer, D. A.; Bates, F. S.; Discher, D. E. *Macromolecules* **2002**, *35*, 8203–8208.
(46) Hough, M. A.; Hasnain, S. S. *J. Mol. Biol.* **1999**, *287*, 579–592.
(47) Palivan, C. G.; Palivan, H.; Goodman, B. A. *Proc. R. Soc. Edinburgh, Sect. B* **1994**, *102*, 273–7.
(48) Palivan, C. G.; Goodman, B. A. *Recent Res. Dev. Inorg. Organomet. Chem.* **2001**, *1*, 141–159.
(49) Schweiger, A.; Jeschke, G. *Principles of Pulse Electron Paramagnetic Resonance Spectroscopy*; Oxford University Press: New York, 2001.
(50) Greenfield, N. J. *Trends Anal. Chem.* **1999**, *18*, 236–244.
(51) Ellerby, L. M.; Cabelli, D. E.; Graden, J. A.; Valentine, J. S. *J. Am. Chem. Soc.* **1996**, *118*, 6556–6561.
(52) Fridovich, I. *J. Biol. Chem.* **1997**, *272*, 18515–7.
(53) Ranquin, A.; Versees, W.; Meier, W.; Steyaert, J.; Van Gelder, P. *Nano Lett.* **2005**, *5*, 2220–2224.
(54) Nardin, C.; Thoeni, S.; Widmer, J.; Winterhalter, M.; Meier, W. *Chem. Commun.* **2000**, 1433–1434.
(55) Gus'kova, R. A.; Ivanov, I. I.; Kol'tover, V. K.; Akhobadze, V. V.; Rubin, A. B. *Biochim. Biophys. Acta* **1984**, *778*, 579–85.
(56) Takahashi, M.; Asada, K. *Arch. Biochem. Biophys.* **1983**, *226*, 558–66.
(57) Broz, P.; Driamov, S.; Ziegler, J.; Ben-Haim, N.; Marsch, S.; Meier, W.; Hunziker, P. *Nano Lett.* **2006**, *6*, 2349–2353.

JP803032W

Amphiphilic Diblock Copolymers for Molecular Recognition: Metal−Nitrilotriacetic Acid Functionalized Vesicles

Rainer Nehring, Cornelia G. Palivan, Oliver Casse, Pascal Tanner, Jens Tüxen, and Wolfgang Meier*

Department of Chemistry, University of Basel, Klingelbergstrasse 80, CH-4056 Basel, Switzerland

Received August 21, 2008. Revised Manuscript Received November 16, 2008

Here we describe the design, synthesis, and characterization of new, metal-functionalized, amphiphilic diblock copolymers for molecular recognition. Polybutadiene-*block*-polyethylenoxide copolymers were synthesized by living anionic polymerization and end group functionalized with nitrilotriacetic acid and tris(nitrilotriacetic acid). After complexation with nickel and copper, these groups are known to selectively bind to oligohistidine residues of proteins. The polymers were characterized by ^{1}H NMR spectroscopy, size exclusion chromatography, electron paramagnetic resonance, and UV−vis spectroscopy. Mixtures of these polymers with the respective nonfunctionalized block copolymers self-assemble in aqueous solution into vesicular structures with a controlled density of the metal complex end-groups on their surface. The accessibility of these binding sites was tested using maltose binding protein carrying a terminal decahistidine moiety and His-tagged enhanced green fluorescent protein as model systems. Fluorescence correlation spectroscopy clearly showed a significant and selective binding of these proteins to the vesicle surface.

Introduction

Molecular recognition at surfaces plays a key role in many processes in Nature. Therefore, appropriately designed surface structures containing biological recognition elements offer considerable potential as model systems to investigate such events in more detail or to create new materials that undergo controlled interactions with biological systems.[1,2] In particular, the selective binding of biologically relevant molecules via metal coordination using, for example, complexes with nitrilotriacetic acid (NTA) or iminodiacetic acid (IDA) ligands can be exploited for their functional and oriented immobilization.[3] Combining such metal-based recognition sites with molecules that are inherently able to self-assemble into well-defined supramolecular structures opens the possibility to induce a higher order self-assembly.[4,5] For example, functionalized synthetic lipids with chelating NTA−Ni^{2+} groups have been used to design surfaces that can serve as templates for 2D protein crystallization,[6−13] and to create metal-affinity-tethered membranes for investigating the complex network of recognition, transport, and signaling processes at membranes.[14] Metal−NTA lipids/liposomes are used in so-called "chelating ligand internalization assays" (CLIA) to screen antibodies for their ability to confer target-specific toxicity in tumor treatment,[15] as specific inhibitors in integral metalloenzyme activity tests,[16] or in the therapeutic domain as vaccines or modulators of intracellular signaling pathways by attaching His-Tag peptides and proteins to the metal region of the system.[17,18]

Similarly to lipids, amphiphilic block copolymers may self-assemble in aqueous media into biomimetic membrane structures. Recently such block copolymer membranes have attracted considerable attention due to their large versatility with respect to their physical, chemical, and biological properties. Here the chemical constitution (e.g., nature of the repeat units), the relative lengths and structure of the different blocks, or even the architecture of the whole polymer can be designed with respect to the desired application.[19−21] Generally, block copolymer membranes are considerably thicker and chemically and mechanically more stable than conventional lipid bilayers, while mimicking natural biomechanical properties.[22] It has been shown that block copolymer membranes can be modified with specific recognition sites by attaching, for example, biotin groups to the hydrophilic ends of the polymers[23−25] or by insertion of integral membrane protein receptors.[26] Likewise, we expected that block copolymers could also be functionalized with metal-chelating

* To whom correspondence should be addressed. Phone: +41 (0)61 267 3802. Fax: +41 (0)61 267 3850. E-mail: Wolfgang.Meier@unibas.ch.

(1) Goddard, J. M.; Hotchkiss, J. H. *Prog. Polym. Sci.* **2007**, *32*, 698–725.
(2) Hatakeyama, H.; Kikuchi, A.; Yamato, M.; Okano, T. *Biomaterials* **2007**, *28*, 3632–3643.
(3) Kruppa, M.; Mandl, C.; Miltschitzky, S.; Konig, B. *J. Am. Chem. Soc.* **2005**, *127*, 3362–3365.
(4) Thompson, D. H.; Zhou, M.; Grey, J.; Kim, H.-k. *Chem. Lett.* **2007**, *36*, 956.
(5) Valiokas, R.; Klenkar, G.; Tinazi, A.; Reichel, A.; Tampe, R.; Pielhar, J.; Liedberg, B. *Langmuir* **2008**, *24*, 4959–4967.
(6) Barklis, E.; McDermott, J.; Wilkens, S.; Schabtach, E.; Schmid, M. F.; Fuller, S.; Karanjia, S.; Love, Z.; Jones, R.; Rui, Y.; Zhao, X.; Thompson, D. *EMBO J.* **1997**, *16*, 1199–1213.
(7) Bischler, N.; Balavoine, F.; Milkereit, P.; Tschochner, H.; Mioskowski, C.; Schultz, P. *Biophys. J.* **1998**, *74*, 1522–1532.
(8) Courty, S.; Lebeau, L.; Martel, L.; Lenne, P.-F.; Balavoine, F.; Dischert, W.; Konovalov, O.; Mioskowski, C.; Legrand, J.-F.; Vénien-Bryan, C. *Langmuir* **2002**, *18*, 9502–9512.
(9) Kubalek, E. W.; Le Grice, S. F. J.; Brown, P. O. *J. Struct. Biol.* **1994**, *113*, 117–123.
(10) Lebeau, L.; Lach, F.; Venien-Bryan, C.; Renault, A.; Dietrich, J.; Jahn, T.; Palmgren, M. G.; Kuhlbrandt, W.; Mioskowski, C. *J. Mol. Biol.* **2001**, *308*, 639–647.
(11) Levy, D.; Mosser, G.; Lambert, O.; Moeck, G. S.; Bald, D.; Rigaud, J.-L. *J. Struct. Biol.* **1999**, *127*, 44–52.
(12) Thess, A.; Hutschenreiter, S.; Hofmann, M.; Tampe, R.; Baumeister, W. *J. Biol. Chem.* **2002**, *277*, 36321–36228.
(13) Venien-Bryan, C.; Schertler, G. F.; Thouvenin, E.; Courty, S. *J. Mol. Biol.* **2000**, *296*, 863–871.
(14) Radler, U.; Mack, J.; Persike, N.; Jung, G.; Tampé, R. *Biophys. J.* **2000**, *79*, 3144–3152.
(15) Nielsen, U. B.; Kirpotin, D. B.; Pickering, E. M.; Drummond, D. C.; Marks James, D. *BMC Immunol.* **2006**, *7*, 24.
(16) Waters, E. K.; Morrissey, J. H. *Biochemistry* **2006**, *45*, 3769–3774.
(17) Chikh, G. G.; Li, W. M.; Schutze-Redelmeier, M.-P.; Meunier, J.-C.; Bally, M. B. *Biochim. Biophys. Acta, Biomembr.* **2002**, *1567*, 204–212.
(18) Dorn, I. T.; Neumaier, K. R.; Tampe, R. *J. Am. Chem. Soc.* **1998**, *120*, 2753–2763.
(19) Foerster, S.; Antonietti, M. *Adv. Mater. (Weinheim, Germany)* **1998**, *10*, 195–217.
(20) Taubert, A.; Napoli, A.; Meier, W. *Curr. Opin. Chem. Biol.* **2004**, *8*, 598–603.
(21) Nardin, C.; Meier, W. *Rev. Mol. Biotechnol.* **2002**, *90*, 17–26.
(22) Mecke, A.; Dittrich, C.; Meier, W. *Soft Matter* **2006**, *2*, 751–759.
(23) Broz, P.; Benito, S. M.; Saw, C.; Burger, P.; Heider, H.; Pfisterer, M.; Marsch, S.; Meier, W.; Hunziker, P. *J. Controlled Release* **2005**, *102*, 475–488.

10.1021/la8027308 CCC: $40.75
Published on Web 12/23/2008

moieties without affecting their ability to self-assemble into well-defined membrane structures.

Here we present for the first time the synthesis of amphiphilic block copolymers with hydrophilic blocks carrying terminal lysine−NTA groups at the hydrophilic blocks. After complexing to metal ions such as Cu(II) or Ni(II), this group is known to selectively bind to oligohistidine sequences of proteins. For our experiments, we synthesized poly(butadiene)-*block*-poly(ethylene oxide) polymers as the model system. The self-assembling behavior of these polymers and their derivatives in aqueous media has been carefully characterized.[27−30] The hydrophobic to hydrophilic block length ratios used in these studies are known to lead to the formation of vesicular aggregates in dilute solutions.[30] In addition, the pendant double bonds of the poly(butadiene) blocks within the vesicular membranes can be covalently cross-linked within the self-assembled superstructures,[27] which leads to further stabilization by introducing a rubber-elastic character to the structures.[31]

The individual synthesis steps were confirmed by ^{1}H NMR spectroscopy and size exclusion chromatography, while the metal functionalization was established by electron paramagnetic resonance and UV−vis spectroscopy. We used fluorescence correlation spectroscopy investigations on metal−NTA-functionalized block copolymer vesicles to quantify binding of His-tagged proteins to the metal sites at their surface.

Materials and Methods

Chemicals. All reagents and solvents were purchased from Aldrich or Fluka with the highest purity grade and used as received unless otherwise noted.

1,3-Butadiene (99+%, Aldrich) was cooled to −78 °C and successively distilled from CaH_2 and *n*-BuLi. Ethylene oxide (EO) was also cooled to −78 °C and successively distilled from CaH_2, sodium mirror, and *n*-BuLi. The phosphazene base *t*-BuP_4 {1-*tert*-butyl-4,4,4-tris(dimethylamino)-2,2-bis[tris (dimethylamino)phosphoranylidenamino]-2Λ^5,4Λ^5-catenadi(phosphazene)] (Fluka, 1.00 ± 0.02 M in hexane) and *N*-methylmorpholin (NMM) for the deprotecting step was used as received. *N*,*N*-Bis[(*tert*-butyloxycarbonyl)methyl]-L-lysine *tert*-butyl ester [Lys−NTA.p (protected)], TrisNTA-OtBu (TrisNTA.p), and His-tagged maltose binding protein conjugated to fluorescein (His_{10}-MBP-FITC) were gifts from the group of Prof. Robert Tampé, Institute of Biochemistry, Biocenter, Goethe Universität, Frankfurt/Main and were used as received. His-tagged enhanced green fluorescent protein (His_6-EGFP) was from Abcam and used as received. Tetrahydrofuran was refluxed over Na/K-alloy, distilled, and stirred with Na/K and benzophenone until a purple color occurs; the dried THF is distilled directly into the reactor prior to synthesis. All polymerization reactions were performed in flame-dried glassware under vacuum and argon atmosphere using standard high-vacuum techniques.

Characterization Methods. *NMR.* ^{1}H NMR spectra were recorded with a Bruker DPX-400 spectrometer in $CDCl_3$ (99.8% D, 0.1% TMS, Aldrich) at room temperature. The signals were referenced to that of TMS at $\delta = 0.00$ ppm.

Size Exclusion Chromatography. Thermo Separation Products setups equipped with UV and RI detectors (Agilent 1100 Series) were used. The column set consisted of three columns in series: an Agilent PLgel guard column, 50 × 7.5 mm with 10 μm diameter beads; an Agilent PLgel 300 × 7.5 mm column with 10 μm diameter beads with 100 Å pore size; and an Agilent PLgel 300 × 7.5 mm column with 5 μm diameter beads with 1000 Å pore size. Analyses were performed at 40 °C using THF at a flow rate of 1.0 mL/min. Poly-1,2-butadiene standards (PSS GmbH, Mainz, Germany) with narrow molar mass distributions were used for calibration.

Electron Paramagnetic Resonance. Electron paramagnetic resonance (EPR) spectra were recorded at low temperatures (130 and 77 K) with a CW Bruker ElexSys500 X-band spectrometer, equipped with a helium temperature control system ER4112HV to which the waveguide resonant cavity was mounted. All measurements were taken using 2 mW microwave power. The modulation frequency was 100 kHz and the modulation amplitude was 0.5 mT; other spectral parameters were adjusted for each spectrum individually. Multiple (20) spectra were acquired to optimize the signal-to-noise ratio, and third-order polynomial averaging was used for subsequent noise reduction. The spectral parameters were obtained using the SIMFONIA software package (Bruker Instruments Inc., Billerica, MA), where coaxial *g* and hyperfine tensors were assumed. Gaussian line shapes were assumed with the line width adjusted for each spectrum. All spectral simulations assumed natural abundance ratios of Cu isotopes. The *g*-values were referenced to diphenylpicryhydrazyl (DPPH) ($g = 2.0036$) as an external standard.

UV−Vis Spectroscopy. UV−vis spectra were recorded with a Perkin-Elmer Lambda 35 UV−vis spectrometer in silica glass cells at 25 °C. Polymer solutions (2×10^{-3} mol/L) were prepared in $CHCl_3$.

Preparation and Characterization of Block Copolymer Vesicles. Vesicles were formed using the film rehydration method. The polymer was dissolved in chloroform using a round-bottomed flask, and then the solvent was evaporated under reduced pressure to produce a thin polymer film on the inner glass surface of the flask. The polymer film was hydrated with bidistilled water to give a concentration of 80 μM while the flask was rotated (30 rotations per minute) at room temperature and atmospheric pressure. In order to obtain homogeneous vesicle solutions, each was successively filtered through a 10 μm and a 1 μm polycarbonate membrane (until the polymer flakes were removed). Next the solutions were extruded through a polycarbonate membrane (11 times) with a convenient cutoff diameter (Nuclepore track-etch membrane, 0.08−10 μm cutoff diameter, Whatman, UK) with a LIPEX 10 mL thermobarrel extruder (Northern Lipids Inc.) or a miniextruder (Avanti Lipids).

Light Scattering. Solutions for light scattering were prepared from a stock solution of 1 mg/mL. Dilutions from 0.1 mg/mL down to 0.01 mg/mL were measured. Samples were poured under laminar flow into 10 mm quartz cells mounted in an optical matching bath. Dynamic and static light scattering (DLS, SLS) experiments were performed at $T = 293$ K ± 0.05 K using a commercial goniometer (ALV) with a He:Ne laser (JDS Uniphase, wavelength $\lambda = 632.8$ nm). The refractive index increment $\partial n/\partial C$ of the vesicle dispersions (containing 10 mol % of the Cu^{2+}−NTA modified block copolymer) was determined to 0.50 ± 0.08 mL/g, at 632.8 nm with an ALV-DR1 differential refractometer. The photon intensity autocorrelation function $g^2(t)$ was determined with an ALV-5000E correlator (scattering angles between 50° and 140°). DLS data were analyzed via nonlinear decay-time analysis supported by the regularized inverse Laplace transform of $g^2(t)$ (CONTIN algorithm). The angle-dependent apparent diffusion coefficient was extrapolated to zero momentum transfer (q^2) and then converted to particle dimensions using a hard sphere model.[32] Angle- and concentration-dependent SLS data were analyzed using Zimm plots approach and applying a vesicle form factor analysis.[32,33]

Inductively Coupled Plasma (ICP) Atom Emission Spectrometry. The content of nickel(II) and copper(II) in the metal-doped vesicle solutions was determined with a CIROS VISION ICP spectrometer

(24) Rigler, P.; Meier, W. *J. Am. Chem. Soc.* **2006**, *128*, 367–373.
(25) Lin, J. J.; Silas, J. A.; Bermudez, H.; Milam, V. T.; Bates, F. S.; Hammer, D. A. *Langmuir* **2004**, *20*, 5493–5500.
(26) Graff, A.; Sauer, M.; Van Gelder, P.; Meier, W. *Proc. Natl. Acad. Sci. U.S.A.* **2002**, *99*, 5064–5068.
(27) Discher, B. M.; Bermudez, H.; Hammer, D. A.; Discher, D. E.; Won, Y.-Y.; Bates, F. S. *J. Phys. Chem. B* **2002**, *106*, 2848–2854.
(28) Gao, W.-P.; Bai, Y.; Chen, E.-Q.; Li, Z.-C.; Han, B.-Y.; Yang, W.-T.; Zhou, Q.-F. *Macromolecules* **2006**, *39*, 4894–4898.
(29) Geng, Y.; Discher, D. E.; Justynska, J.; Schlaad, H. *Angew. Chem., Int. Ed.* **2006**, *45*, 7578–7581.
(30) Jain, S.; Bates, F. S. *Science (Washington, DC)* **2003**, *300*, 460–464.
(31) Schwartz, A. *J. Therm. Anal.* **1978**, *13*, 489–497.
(32) Schmitz, K. S. *An Introduction to Dynamic Light Scattering by Macromolecules*: Academic Press Inc.: New York, 1990.
(33) Burchard, W. *Adv. Polym. Sci.* **1983**, *48*, 1–124.

Scheme 1. Synthesis of the Succinic Acid Semi-Ester of Polybutadiene-*block*-poly(ethylene oxide) (PB-PEO-SA-OH) (8), Ni^{2+}−TrisNTA-Modified Polybutadiene-*block*-poly(ethylene oxide) (PB_{39}-PEO_{36}-SA-TrisNTA.d−Ni^{II}) (13a), and Ni^{2+}−NTA-Modified Polybutadiene-*block*-poly(ethylene oxide) (PB_{60}-PEO_{34}-SA-NTA.d−Ni^{II}) (13b)[a]

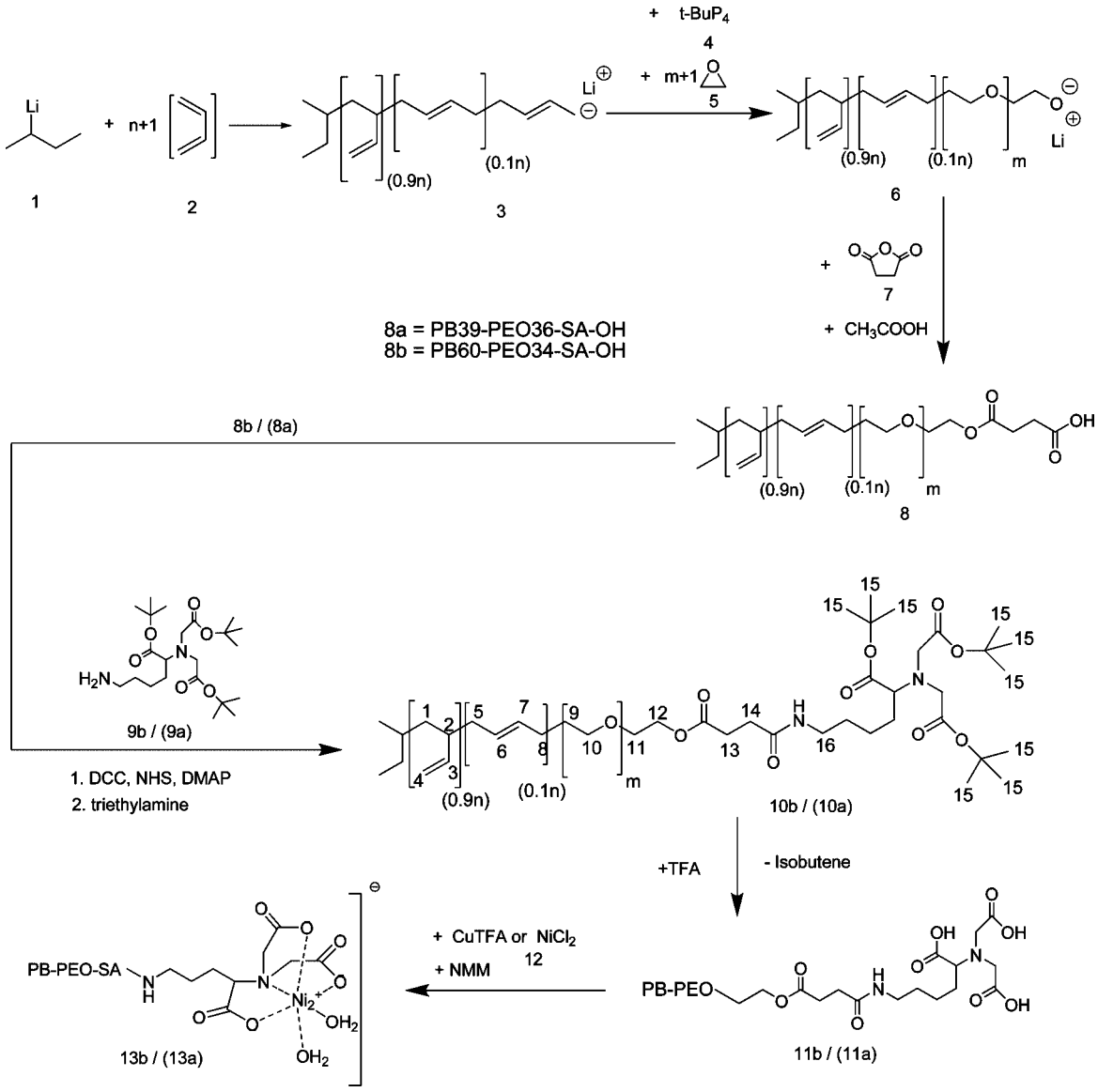

[a] The structures of **9a**, **10a**, **11a**, and **13a** are given in Supporting Information.

from Spectra. The specimen flux was 2 mL/min. The solution was injected from a cyclone spray chamber into the argon plasma at a temperature of $T = 10\,000$ K.

Optical Microscopy. Vesicle dispersions in bidistilled water were examined with a transmission microscope (DMIRE2, Leica), at a magnification of 20 × 10, with a polarization filter.

Fluorescence Correlation Spectroscopy. Fluorescence-correlation spectroscopy (FCS) measurements were performed with a Zeiss LSM 510-META/Confocor2 laser-scanning microscope equipped with an argon laser (488 nm) and a 40× water-immersion objective (Zeiss C/Apochromat 40×, NA 1.2), with the pinhole adjusted to 70 μm. Solutions were measured at room temperature in specially chambered quartz-glass holders (Laboratory-Tek; 8-well, NUNC A/S) that provide optimal conditions by reducing evaporation. Respectively, 30 nM His_{10}-MBP-FITC and 20nM His_6-EGFP were added to the solutions of metal-doped vesicles, and the mixtures were immediately measured.

Spectra were recorded over 30 s, and each measurement was repeated 10 times; results are reported as the average of three independent experiments. Adsorption and bleaching effects were reduced by exchanging the sample droplet after 5 min of measurement. To reduce the number of free fitting parameters, the diffusion times for free dye (FITC) as well as free, labeled proteins (His_{10}-MBP-FITC and His_6-EGFP, respectively) were determined independently and fixed in the fitting procedure of the autocorrelation function. Intensity fluctuations were analyzed in terms of an autocorrelation function using the LSM 510/Confocor software package (Zeiss, AG).

Experimental Procedures. *Synthesis and Characterization of the NTA−Diblock Copolymers (Scheme 1).* The diblock copolymers (PB_{39}-PEO_{36}-O^-) were synthesized via anionic polymerization as described elsewhere.[34−36] The product PB_{39}-PEO_{36}-O^- (**6**) (8.01 g, 2.27 mmol) was used in situ for the next step.

Functionalization of Polybutadiene-b-poly(ethylene oxide) (PB_{39}-PEO_{36}-SA-OH), **8** The polymerization was quenched with a 0.30 M solution of succinic anhydride (**7**) (20 mL, 6.00 mmol, 2.10 equiv) in THF, and afterward, 3 mL of acetic acid was added. Two spatula tips of ion-exchange resin Dowex 50WX4-100 were added. The ion-exchange resin was filtered off and most of the solvent was

(34) Foerster, S.; Kraemer, E. *Macromolecules* **1999**, *32*, 2783–2785.
(35) Schlaad, H.; Kukula, H.; Rudloff, J.; Below, I. *Macromolecules* **2001**, *34*(13), 4302–4304.
(36) Zalipsky, S. *Bioconjugate Chem.* **1995**, *6*, 150–165.

Table 1. Molar Masses and Polydispersities of the PB Precursors and the PB-PEO Diblock Copolymers[a]

	N_n PB			N_n PEO				
sample ID	calc[b]	GPC[c]	GPC M_w/M_n PB	calc[d]	NMR	GPC[e] M_w/M_n PB-PEO	NMR ratio PB 1.2/1.4	GPC + NMR[f] M_n (g/mol) PB-PEO
PB_{60}-PEO_{34}-SA-OH (**8b**)	46	60	1.12	24	34	1.08	0.9/ 0.1	4310
PB_{60}-PEO_{34}-SA-NTA.d (**11b**)	46	60	1.12	24	34	1.12	0.9/ 0.1	4750
PB_{39}-PEO_{36}-SA-OH (**8a**)	46	39	1.08	24	36	1.08	0.9/ 0.1	3530
PB_{39}-PEO_{36}-SA-TrisNTA.d (**11a**)	46	39	1.08	24	36	1.13	0.9/ 0.1	3690

[a] GPC was performed in THF; ^{1}H NMR spectroscopy was performed in $CDCl_3$. [b] N_n was calculated from the monomer/initiator ratio. [c] N_n of the PB precursor was determined by GPC (calibrated with narrow PB standards). [d] N_n of the PEO block was calculated from the PB/PEO ratio obtained from the ^{1}H NMR spectra. [e] M_w/M_n of the diblock was obtained by GPC (PB standards). [f] Average number was calculated from GPC and ^{1}H NMR spectroscopy.

evaporated under reduced pressure until the reaction mixture became viscous.

After precipitation in 1.5 L of cold ($T = -94$ °C) acetone and drying under vacuum to constant weight, the polymer **8** (5.63 g, yield: 66%) was obtained as a yellow solid. GPC: $M_n = 3437$ g/mol, $M_w/M_n = 1.077$. ^{1}H NMR (400 MHz, $CDCl_3$, δ/ppm): 5.57−5.28 (m, 3H, 3, 6, 7), 4.97−4.85 (m, 2H, 4), 4.25 (t, $^3J_{HH} = 4.6$ Hz, 2H, 12), 3.82 (t, $^3J_{HH} = 4.5$ Hz, 2H, 11), 3.74−3.64 (m, 2H, 9, 10), 2.64 (m, 4H, 13, 14), 2.12−1.85 (m, 5H, 2, 5, 8), 1.25−1.06 (m, 2H, 1).

Synthesis of PB_{39}-PEO_{36}-SA-TrisNTA.p (**10a**). PB_{39}-PEO_{36}-SA-OH (**8**) (5.63 g, 1.00 mmol, 1.0 equiv) was introduced into a 500 mL round-bottom flask. The polymer was dissolved in 40 mL of dichloromethane. A solution of dicyclohexylcarbodiimide (206 mg, 1.00 mmol, 1.0 equiv), *N*-hydroxysuccinimide (115 mg, 1.00 mmol, 1.0 equiv), and 4-(dimethylamino)pyridine (15 mg, 0.12 mmol, 0.12 equiv) in 40 mL of dichloromethane was added. After 12 h of stirring at room temperature under the exclusion of light, the precipitated urea was filtered off and a solution of TrisNTA.p (**9a**) (0.50 g, 0.347 mmol, 0.35 equiv) and triethylamine (400 μL) in 60 mL of dichloromethane was added. The reaction mixture was stirred for 24 h at room temperature under dark. Thereafter the solvent was removed under reduced pressure until the reaction mixture became viscous. Product **10a** was precipitated in cold methanol (1 L) and dried under vacuum to give a yield of 63% (3.53 g).

^{1}H NMR (400 MHz, $CDCl_3$, δ/ppm): 5.57−5.28 (m, 3H, 3, 6, 7), 4.97−4.85 (m, 2H, 4), 4.29 (m, TrisNTA.p), 4.28−4.25 (m, 2H, 12), 3.82 (m, 2H, 11), 3.74−3.64 (m, 2H, 9, 10), 3.42 (m, Tris−NTA.p), 3.02−2.62 (m, TrisNTA.p), 2.62 (m, 4H, 13, 14), 2.12−1.85 (m, 5H, 2, 5, 8), 1.43−1.46 (m, *tert*-Bu, 15),1.25−1.06 (m, 2H, 1). ^{13}C NMR (100 MHz, $CDCl_3$, δ/ppm): 143.2 (s, Ct, 3), 114.3 (s, Cs, 4), 70.5 (s, Cs, 9, 10), 38.7 (s, Cs, 1), 38.5 (s, Ct, 2), 28.2 (*tert*-Bu, 15).

Deprotection of PB_{39}-PEO_{36}-SA-TrisNTA.p (**10a**). The functionalized polymer **10a** (3.53 g, 0.9 mmol) was dissolved in 40 mL of chloroform. A mixture of 20 mL of trifluoroacetic acid and 40 mL of chloroform was added to the polymer solution. The reaction mixture was stirred for 24 h at room temperature in the dark. After evaporating the solvent and the trifluoroacetic acid under vacuum, the crude product was washed with a 1 M aqueous solution of sodium hydroxide (2 × 10 mL) and water (2 × 10 mL). The last aqueous phase was extracted (4 × 100 mL) with $CHCl_3$, and the combined organic layers were dried over sodium sulfate. The solvent was evaporated under vacuum. The deprotected diblock copolymer (**11a**, 2.40 g, yield: 62%) was obtained as a yellow viscous liquid. GPC: $M_n = 3171$ g/mol, $M_w/M_n = 1.129$. ^{1}H NMR (400 MHz, $CDCl_3$, δ/ppm): 5.57−5.28 (m, 3H, 3, 6, 7), 4.97−4.85 (m, 2H, 4), 4.29 (m, TrisNTA.d), 4.27−4.25 (m, 2H, 12), 3.82 (m, 2H, 11), 3.74−3.64 (m, 2H, 9, 10), 3.44 (m, TrisNTA.d), 2.65 (m, 4H, 13, 14), 2.12−1.85 (m, 5H, 2, 5, 8), 1.43 (s, TrisNTA.p, *tert*-Bu, 15; residual peak), 1.25−1.07 (m, 2H, 1).

PB_{39}-PEO_{36}-SA-TrisNTA.d (**11a**) + *$NiCl_2$/Cu(TFA)$_2$* (**12**). In order to complex the Ni^{2+} ions/Cu^{2+} ions (**12**) with the block copolymer-NTA.d, a 0.30 mM solution of polymer in $CHCl_3$/MeOH (10:1) and 15 mM $NiCl_2$/Cu(TFA)$_2$ (**12**), 200 mM tris(hydroxymethyl)aminomethane (TRIS)/HCl (pH = 8.5) solution were mixed and stirred overnight at 25 °C. The water phase was removed and the chloroform phase was washed once with TRIS buffer. The solvent was removed via rotary evaporator. The greenish polymer (**13a**) was dried in vacuum overnight at room temperature to obtain 2 g (yield 83%) of the final product.

Results and Discussion

Scheme 1 shows the synthesis of TrisNTA−Ni^{2+}- and NTA−Ni^{2+}-functionalized poly(butadiene)-*block*-poly(ethylene oxide). The introduction of terminal NTA−Ni^{2+} groups was performed under identical conditions using *N*,*N*-bis[(*tert*-butyloxycarbonyl)methyl]-L-lysine *tert*-butyl ester (Lys-NTA-OtBu) and TrisNTA-OtBu as reagent.

The anionic polymerization was performed as reported before using *t*-BuP_4 (**4**) as a base.[34] *t*-BuP_4 is known to efficiently complex lithium ions and therefore suppresses ion pair association and facilitates the subsequent polymerization of EO.[34] Size exclusion chromatography of the polybutadiene (PB, **3**) proves a narrow molar mass distribution of $M_w/M_n = 1.08$. Poly(ethylene oxide) polymerization was initiated by adding ethylene oxide to the living PB anions. After activation with dicyclohexylcarbodiimide, the polymeric carboxylic acid PB_{39}-PEO_{36}-SA-OH (**8a**) or PB_{60}-PEO_{34}-SA-OH (**8b**) was reacted with the *tert*-butyl protected TrisNTA (**9a**) or Lys-NTA (**9b**), respectively.[18] After deprotection[37] and further purification, the yield of the functionalized block copolymer was found to be 68% (PB_{39}-PEO_{36}-SA-TrisNTA.d, **11a**) and 35% (PB_{60}-PEO_{34}-SA-NTA.d, **11b**), respectively. The yield of polymer **11a** is higher due to its more hydrophilic character, which promotes an easier precipitation in nonpolar solvents. Table 1 shows the molar masses and polydispersities determined by SEC and NMR data of the different block copolymers. To obtain the metal−polymer complex, the block copolymers (**11a** and **11b**) were stirred with the respective metal salt solutions overnight until a green polymer solution was obtained, which indicates a change in the coordination sphere of the metal.

Characterization of the Block Copolymers. The individual reaction steps during functionalization of the PB-PEO block copolymers were analyzed by ^{1}H NMR spectroscopy.

The ^{1}H NMR spectrum of PB_{60}-PEO_{34}-SA-OH (**8b**) (Figure 1a) clearly shows the presence of the terminal semi-ester of succinic acid. The multiplet at 4.22 ppm can be attributed to the methylene protons of the semi-ester of succinic acid at the end of the hydrophilic blocks. Integration indicates that more than 90% of the PEO blocks of the polymers have been converted. Upon reaction of *tert*-butyl protected Lys-NTA with polymer PB_{39}-PEO_{36}-SA-OH a broad singlet at 1.45 ppm (s, 27H) (Figure 1b) appears that can be attributed to the methyl protons of the *tert*-butyl groups. The ^{1}H NMR indicates the formation of an amide bond[38] between the polymer and the protected NTA by the presence of the multiplet at 3.30 ppm (−CONHCH_2C−) (m, 2H). Heteronuclear multiple bond correlation (HMBC)—not shown here—indicates a coupling of proton 16 (Scheme 1, **10b**) with the carbon of the carboxylic group of the amide bond. Finally, the ^{1}H NMR spectrum in Figure 1c indicates that the deprotection

(37) Brückner, R. *Reaktionsmechanismen*, 2nd ed.; Spectrum Verlag: München, 2002 p 190.

(38) Schmitt, L.; Dietrich, C.; Tampé, R. *J. Am. Chem. Soc.* **1994**, *116*, 8485–8491.

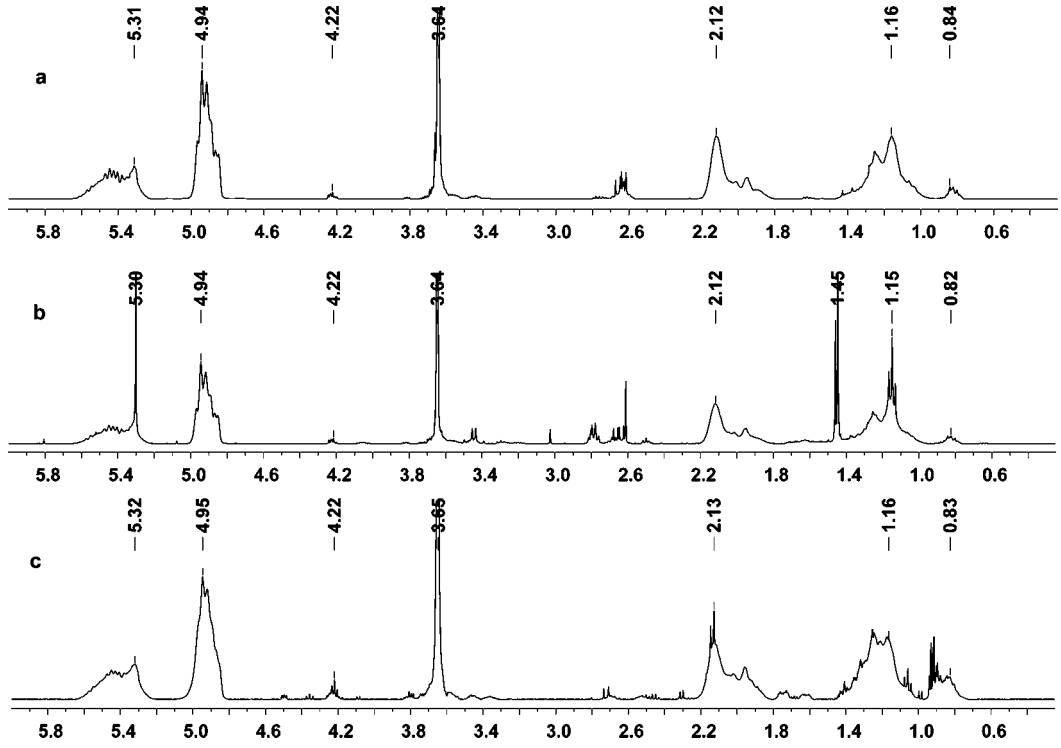

Figure 1. ^{1}H NMR spectra of (a) PB_{60}-PEO_{34}-SA-OH, (b) PB_{60}-PEO_{34}-SA-NTA.p, and (c) PB_{60}-PEO_{34}-NTA.d showing the steps of specific functionalization at 4.22 ppm ($-CH_2OCO-$), 3.30 ppm ($-CONHCH_2C-$), and 1.45 ppm [$3 \times (CH_3)_3-$] as well as the decrease of the peak intensity at 1.45 ppm for the deprotected polymer, respectively.

of the NTA group was nearly complete since the peak of the *tert*-butyl group at 1.41 (1.45) ppm is significantly reduced. In the case of Tris−NTA polymer, the ^{1}H NMR investigation also confirmed a well-defined polymer structure.

Characterization of the Metal-Functionalized Block Copolymers. After stirring the block copolymer solutions with aqueous buffers containing $Cu(TFA)_2$ or $NiCl_2$, respectively, we investigated whether the metals were coordinated to the NTA moiety at the hydrophilic chain end, by EPR and UV−vis spectroscopy. It has to be noted that the addition of the metal salts caused in both cases an immediate color change of the polymer solution from pale yellow to green.

The UV−vis spectra of PB_{60}-PEO_{34}-SA-OH (**8b**) and PB_{39}-PEO_{36}-SA-OH (**8a**) were compared to that of the corresponding metal-functionalized polymers PB_{60}-PEO_{34}-SA-NTA.d−Ni^{2+}/Cu^{2+} (**13b**) (see Supporting Information, Figure S1) and PB_{39}-PEO_{36}-SA-TrisNTA.d−Ni^{2+}/Cu^{2+} (**13a**), respectively. After addition of Ni(II), both NTA-functionalized polymers showed nearly identical electronic spectra with absorption bands at $\lambda_1 =$ 622 nm and $\lambda_2 =$ 390 nm, which are characteristic for hexacoordinated Ni(II).[39] The visible absorption band λ_1 attributed to the $^3A_{2g} \rightarrow {}^3T_{1g}(F)$ transition is clearly resolved, while λ_2, which is attributed to the $^3A_{2g} \rightarrow {}^3T_{1g}(P)$ transition, is present only as a shoulder due to superposition of several high intensity CT and intraligand bands in the domain <420 nm. As previously shown, these bands are characteristic for the $[Ni(NTA)(H_2O)_2]^-$ complex[40] and therefore indicate that the metal indeed binds to the NTA group of the copolymers. The electronic spectra of Cu(II) modified polymers were similar for both NTA-functionalized copolymers, and the large d−d band at 745 nm is indicating a pyramidal symmetry around the metal. It is known that this band is characteristic for $[Cu(NTA)H_2O^-]$,[41] although it appears in our experiment at a slightly lower wavelength due to the polymer environment.

We examined the complex formation of $Cu(TFA)_2$ with polymers **8a**, **11a**, and **13a**, respectively, by EPR. Different coordinations of Cu(II) are directly reflected in the EPR spectra, since the spin Hamiltonian parameters of copper ions are very sensitive to changes in the coordination sphere around the metal.[42] This makes Cu(II) ideally suited as a probe to investigate the interactions with the corresponding polymers.

As shown in Figure 2A-a, the shape of the EPR spectrum indicates the presence of two paramagnetic Cu(II) species (see the low-field region, the so-called parallel region of the spectrum: * and + signals) for polymer **8a**. Therefore, we simulated the frozen solution spectrum taking into account two paramagnetic species, **A** and **B**. (Figure 2A-b) These species are formed in a 3:2 ratio, as obtained from the best fit with axial gyromagnetic and hyperfine tensors (see Table 2).

The overall shape of the EPR spectrum does not change for polymer **11a** but decreases significantly in intensity. Obviously Cu(II) forms the same paramagnetic species as before, but with significantly lower concentration. Finally, in the presence of the polymer **13a**, with a free NTA end group, a different EPR spectrum was obtained (Figure 2A-c).

We simulated the spectrum by taking into account axial gyromagnetic and hyperfine tensors (Figure 2A-d). EPR parameters (Table 2) and the presence of a superhyperfine pattern in the perpendicular region of the EPR spectrum (3200 −3400 G) clearly indicate that a new type of paramagnetic Cu(II) species is formed. In order to improve the resolution, we measured the

(39) Triest, M.; Bussiere, G.; Belisle, H.; Reber, C. *J. Chem. Educ.* **2000**, *77*, 670.

(40) Medici, L.; Prins, R. *J. Catal.* **1996**, *163*, 28–37.

(41) Dembowski, J. S.; Kurtz, D. C.; Nakon, R. *Inorg. Chim. Acta* **1988**, *152*, 209–210.

(42) Hathaway, B. J. *Comprehensive Coordination Chemistry*; Wilkinson, G., Ed.; Pergamon Press: New York, 1987; Vol. *5*, pp 134−145.

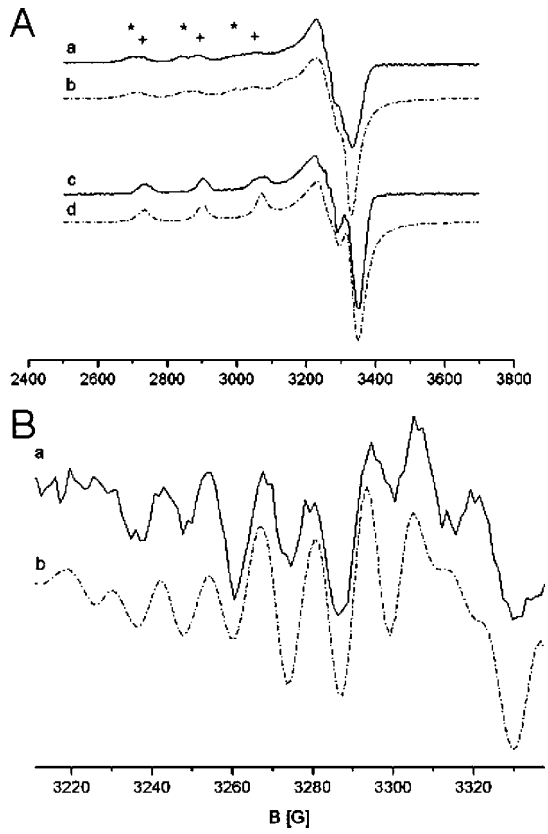

Figure 2. (A) EPR spectra of the Cu(II) paramagnetic species formed by addition of $Cu(TFA)_2$ to (a) PB_{39}-PEO_{36}-SA-OH (**8a**) and (c) PB_{39}-PEO_{36}-SA-NTA.d (**11a**), together with their simulations (b and d, respectively). "*" signals belong to the species A, while "+" signals belong to species B. (B) High-field region of the D_2-EPR spectrum of the Cu(II) paramagnetic species formed by addition of $Cu(TFA)_2$ to (a) PB_{39}-PEO_{36}-SA-TrisNTA.d (**11a**), together with its simulation (b). All the spectra were recorded at 77 K.

second derivative of the absorption spectrum (D_2-EPR spectrum) (Figure 2B-a). The presence of superhyperfine structure provides information about the nitrogen nuclei present in the first coordination sphere around the metal.[43] By simulation we found out that in our system copper has only one nitrogen atom in its coordination sphere, as obtained by simulation of the D_2-EPR spectrum (Figure 2B-b), with a hyperfine coupling constant of $a_N = 1.1$ mT, similar to the values of the hyperfine coupling constants found in other 1N3O Cu(II) complexes.[44] The presence of nitrogen in the coordination sphere of the metal clearly proves that it is exclusively bound to the NTA moiety of the block copolymer.

A similar EPR spectrum was obtained for PB_{60}-PEO_{34}-SA-TrisNTA.d after addition of $Cu(TFA)_2$, with, however, more intense signals. This is not surprising, since each metal coordinates to one NTA group of the TrisNTA moiety. The samples containing Ni(II) together with polymers **8a**, **11a**, and **13a** were EPR-silent, from room temperature until 77 K, as expected.

Formation of the Metal-Functionalized Vesicles. To test the accessibility of the Ni^{2+}−NTA groups at the surface of self-assembled block copolymer membranes, we prepared vesicles both from polymer **8a** and from a mixture of 10 mol % of polymer **13a** in polymer **8a** (metal-doped vesicles), using the film rehydration method.[45] The pure polymer **8a**, the metal-free PB_{39}-PEO_{36}-SA-NTA.d, and the polymer mixture formed vesicular structures; i.e., the presence of the metal-functionalized polymer did not affect the self-assembly behavior (see Supporting Information). Similar behavior has been reported for other end-group functionalized block copolymers.[23−25]

As typical for the film rehydration method, the samples show a broad size distribution with vesicle sizes ranging from several micrometers down to ca. 100 nm (Figure 3). It should be noted that also vesicles modified with Cu−NTA groups showed identical size distributions. The average size and size distribution were reduced by repeated extrusion through filters of defined pore width.

After extrusion the vesicles were characterized by static and dynamic light scattering (SLS and DLS, respectively). DLS clearly shows that the extrusion leads to a monodisperse population of vesicular structures with a hydrodynamic radius of 118 ± 7 nm (see Supporting Information). To get additional information about the molar mass and the shell thickness of the aggregates, we analyzed the PB_{60}-PEO_{34}-SA-NTA.d−Cu^{2+}-containing vesicles by SLS. Both quantities can be obtained through a careful form factor analysis, since they are directly related to the concentration and angle-dependent scattered light intensity via[32]

$$\frac{KC}{R_\theta} = \left(\frac{1}{M_w} + 2A_2C\right)/P(q) \qquad (1)$$

where R_θ is the solute Rayleigh ratio (m^{-1}), K is the contrast factor (mol m^2 g^{-2}) and $q = (4\pi n/\lambda)\sin(\theta/2)$ is the momentum transfer (m^{-1}). Usually the form factor $P(q)$ used is the one for random coils, which gives a linear Zimm plot. In our case, due to the size of the vesicles and the contrast induced by the presence of the metal (refractive index increment of 0.35 mL/g, instead of 0.1 mL/g usually found for polymers), we use a different form factor, that for monodisperse vesicles. The dimensionless form factor $P(q)$ is given for large monodisperse vesicles by[33]

$$P(q) = \left\{\frac{3}{U^3 - u^3}[\sin(U) - U\cos(U)] - \sin(u) + u\cos(u)\right\}^2 \qquad (2)$$

where $U = qR$ and $u = qr$ (R is the outer radius of vesicle and r the inner one, respectively). Figure 5 shows a Zimm plot for the Cu^{2+}−NTA modified vesicles. Here we fitted the normalized inverse scattering ratio (KC/R_θ, mol/g) as a function of angle (θ) and mass concentration (C) with four parameters: the outer and the inner radii (R, r) of the vesicles (and with that, the membrane thicknesses $R - r$), the weight-average molecular mass (M_w), and the second virial coefficient (A_2) (Figure 4). It should be noticed that a slight deviation between the curvature of the fitting curves and the experimental data appears, as expected due to the polydispersity of the vesicles radii and in agreement with DLS (see Supporting Information, Figure S2).

Our analysis yields $M_w = 21 \times 10^6 \pm 2 \times 10^6$ mol/g and $A_2 \approx 0$ within experimental error (i.e., no long-range interactions between the vesicles in the concentration range investigated). The membrane thickness ($R - r$) was calculated to be 8 ± 2 nm. A similar membrane thickness was observed by cryo-TEM on polymer vesicles formed by a nonfunctionalized PB-PEO block copolymer with similar molar mass and block length ratio.[46] The outer radius of the vesicles was determined to be $R = 107 \pm 10$ nm, in good agreement with the hydrodynamic radius r_h obtained

(43) Palivan, C. G.; Goodman, B. A. *Recent Res. Dev. Inorg. Organomet. Chem.* **2001**, *1*, 141–159.
(44) Palivan, C. G.; Palivan, H. M. N.; Goodman, B. A.; Cristescu, C. *Appl. Magn. Reson.* **1998**, *15*, 477–488.
(45) Bermudez, H.; Brannan, A. K.; Hammer, D. A.; Bates, F. S.; Discher, D. E. *Macromolecules* **2002**, *35*, 8203–8208.
(46) Lee, J. C. M.; Bermudez, H.; Discher, B. M.; Sheehan, M. A.; Won, Y.-Y.; Bates, F. S.; Discher, D. E. *Biotechnol. Bioeng.* **2001**, *73*, 135–145.

Table 2. Spin Hamiltonian Parameters of the Cu(II) Paramagnetic Species Formed by Addition of $Cu(TFA)_2$ to Differently Functionalized Copolymer Systems

polymer system	g			A (mT)		
	g_{xx}	g_{yy}	g_{zz}	A_{xx}	A_{yy}	A_{zz}
PB_{39}-PEO_{36}-SA-OH (**8a**) (**A**)	2.047	2.053	2.309	2.0	2.0	14.6
PB_{39}-PEO_{36}-SA-OH (**8a**) (**B**)	2.053	2.053	2.272	1.5	1.5	16.0
PB_{39}-PEO_{36}-SA-TrisNTA.d (**11a**) (**C**)	2.052	2.052	2.253	3.3	3.1	16.4

by DLS. These data clearly show that within experimental error the presence of the metal−NTA groups did not affect the morphology of the polymer vesicles.

His-Tagged Protein Binding to the Surface of the Copolymer Vesicles. To test binding of His-tagged proteins to the surface of the metal−NTA functionalized vesicles, we used maltose binding protein labeled with fluoresceine (His_{10}-MBP-FITC) and His-tagged enhanced green fluorescent protein (His_6-EGFP) as model systems. The binding affinity was quantified by fluorescence correlation spectroscopy (FCS). In FCS, a special fluctuation correlation approach is applied, in which the laser-induced fluorescence of the excited fluorescent molecules that pass through a very small probe volume is autocorrelated in time to give information about the diffusion times of the molecules. The diffusion time is related to the hydrodynamic radius of a particle via the Stokes−Einstein relation, and its change provides information about the coupling of the fluorescent molecule to a larger target molecule.[47] In our experiment, the size difference between a free protein (His_{10}-MBP-FITC or His_6-EGFP) and the protein-bound to the surface of a metal-doped vesicle with dimensions >100 nm should allow us to differentiate between these two states.[18] Figure 5 presents the results when His_{10}-MBP-FITC is added to a solution of PB_{60}-PEO_{34}-SA-OH/PB_{60}-PEO_{34}-SA-NTA−Ni^{II} (10:1) vesicles, with a concentration of Ni^{2+} of 2 μM; the autocorrelation amplitudes are normalized to 2, to compare the curves for their shapes and diffusion times. Multiphasic curve shapes manifest the presence of more than one diffusing species in a sample for diffusion coefficients being sufficiently different.[48] The diffusion time of the free protein His_{10}-MBP-FITC is τ_d = 64 μs (Figure 5, curve a), which corresponds to a hydrodynamic radius of 2.1 nm. This is in good agreement with the calculated radius of 2.4 nm, on the basis of the molecular mass of labeled MBP of 43.6 kDa. When His_{10}-MBP-FITC (30 nM) was added to a solution of PB_{60}-PEO_{34}-SA-OH/PB_{60}-PEO_{34}-SA-NTA−Ni^{II} (10:1) vesicles, with a concentration of Ni^{2+} of 2 μM, a different autocorrelation function was obtained (Figure 5, curve b).

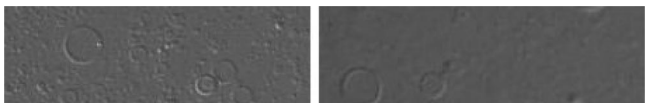

Figure 3. Giant vesicles obtained via film rehydration of (a) PB_{39}-PEO_{36}-SA-OH and (b) PB_{39}-PEO_{36}-SA-OH/PB_{39}-PEO_{36}-SA-TrisNTA.d−Ni^{II} (10:1). (Optical microscope Leica DMIRE2, with magnification 20 × 10; media, bidistilled H_2O; bar, 40 μm.)

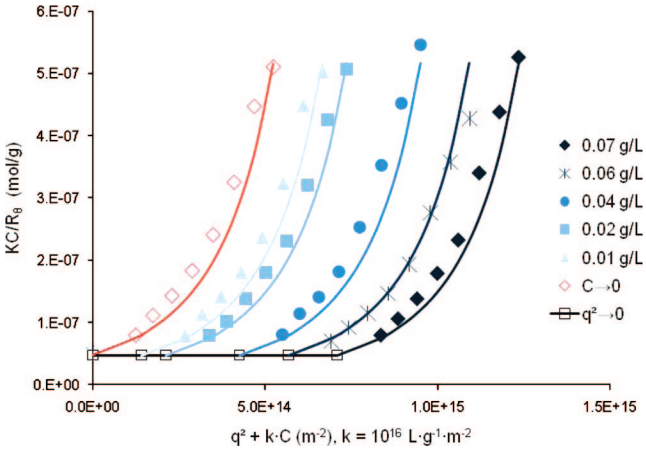

Figure 4. Zimm plot for PB-PEO block copolymer vesicles containing 10 mol% of Cu^{2+}−NTA-modified polymer. Data were fitted using the vesicle form factor.

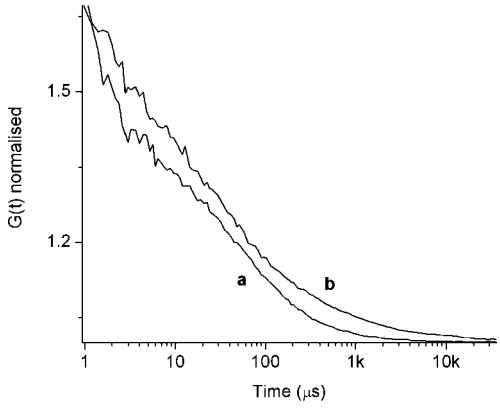

Figure 5. Fluorescence autocorrelation function $G(t)$ of (a) free His_{10}-MBP-FITC protein (30 nM) and (b) when His_{10}-MBP-FITC is added to a solution of PB_{39}-PEO_{36}-SA-OH/PB_{39}-PEO_{36}-SA-TrisNTA−Ni^{2+} (10:1) vesicles [2 μM of Ni(II)].

When His_6-EGFP was used together with M−NTA vesicles and Ni(II) or Cu(II) in similar conditions [30 nM protein and a 2 μM M(II)], the fit of the autocorrelation function in situ at equilibrium indicated that the second particle population has a similar value with a diffusion time of τ_d = 4.8 ± 0.5 ms.

To determine the dissociation constant, K_D, of the His-tag/Ni^{2+}−NTA interaction at the vesicle surface, we titrated His_{10}-MBP-FITC and His_6-EGFP, respectively, with increasing concentrations of Ni^{2+}-doped-vesicles (PB_{39}-PEO_{36}-SA-OH/PB_{39}-

(47) Eigen, M.; Rigler, R. *Proc. Natl. Acad. Sci. U.S.A.* **1994**, *91*, 5740–5747.
(48) Korlach, J.; Schwille, P.; Webb, W. W.; Feigenson, G. W. *Proc. Natl. Acad. Sci. U.S.A.* **1999**, *96*, 8461–8466.

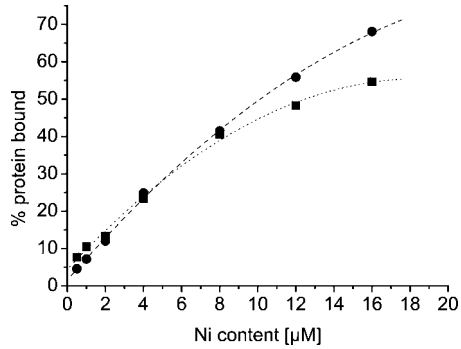

Figure 6. Fraction of bound protein versus the Ni(II) content at the outer vesicles surface [PB_{39}-PEO_{36}-SA-OH/PB_{39}-PEO_{36}-SA-NTA−Ni^{2+} (10:1) vesicles]: black squares, His_{10}-MBP-FITC (30 nM) in PBS; black circles, His_6-EGFP (20 nM), in PBS.

PEO_{36}-SA-TrisNTA−Ni^{2+} (10:1) vesicles), the content of Ni^{2+} varying from 0.5 to 16 μM. To avoid errors due to the loss of the modified polymers during the preparation procedure (e.g., adsorption to the filter in the extrusion step), we determined the concentration of the Ni^{2+}−NTA groups in the vesicle dispersions by inductive coupled plasma (ICP) atom emission spectroscopy. Due to the statistical character of the self-assembly process of vesicles formation, we assumed for our calculations that 50% of the overall Ni^{2+}−NTA groups are exposed on the outer surface of the vesicles and, hence, accessible to the His-tagged proteins. The fluorescence autocorrelation functions were normalized to an equal number of molecules in the confocal volume. For each metal concentration, the fraction of the protein bound to the surface of the vesicles was calculated by a two-component fit of the autocorrelation function of the time-dependent fluorescence signal, $G(t)$. This takes into account that at equilibrium there are two molecule populations: the free protein and a second population, with a big diffusion time, which represents the protein-vesicle population (see Figure 5, curve b, for the case when the content of Ni(II) at the outer vesicles surface is 2 μM). The fraction of protein-bound vesicles has to be corrected for differences in the fluorescence quantum yield of bound and free protein using eq 3:[18]

$$c = \frac{F}{F + \alpha^2 - F\alpha^2} \tag{3}$$

where c corresponds to the corrected fraction of vesicle-bound protein, F stands for the measured fraction of vesicle-bound protein, and α is the ratio of counts per molecules (cpm) in the free and bound state, respectively (in this experiment the calculated α is 0.64 for Ni(II)-doped vesicles and 0.68 for Cu-doped vesicles, respectively).

By increasing the amount of metal-functionalized vesicles in the presence of a constant amount of protein, the fraction of protein-bound vesicles at equilibrium increased substantially. This fraction was plotted against the metal content (Figure 6), and the data were fitted by a Langmuir isotherm, as previously used for Ni^{2+}−NTA functionalized liposomes.[18]

For His_{10}-MBP-FITC we determined the dissociation constant K_D to be $K_D = 7.0 \pm 1.2$ μM, while for His_6-EGFP we obtained $K_D = 12.3 \pm 1.2$ μM. These values are the same order of magnitude as that obtained with Ni^{2+}−NTA-functionalized liposomes ($K_D = 4.3$ μM).[18] The slightly higher dissociation constants of the block copolymer vesicles are presumably a result of steric hindrance due to the PEO brushes at the vesicle surface that surround the individual binding sites. This will be investigated in future experiments by mixing the Ni^{2+}−NTA-modified polymers with nonfunctionalized PB-PEO block copolymers having different PEO chain lengths. It should be noted that control measurements with vesicles without Ni^{2+}−NTA groups showed less than 3% of protein binding. This clearly shows that under our experimental conditions nonspecific protein adsorption to the PEO brushes at the vesicle surface is negligible.

The effect of different buffers on the binding efficiency of the proteins has been established by comparing the fraction of protein−vesicle conjugates in PBS and TRIS buffers. For both metal-doped polymer vesicles, the fraction of protein−vesicle conjugates was significantly higher in PBS buffer compared to the TRIS buffer (see Supporting Information). Even if this effect was more pronounced for copper-doped vesicles than for nickel-doped ones, in a given buffer the binding of both types of metal-functionalized vesicles was comparable. We consider that in the case of TRIS buffer there is a competition between the protein and the buffer molecules to access the metal site. This is not the case in PBS buffer, where only the protein is accessing the metal sites.

Conclusions

In this paper, we described for the first time the synthesis and the characterization of poly(butadiene)-*block*-poly(ethylene oxide) copolymers with terminal M(II)−NTA groups (copper or nickel). Moreover, we successfully used a convenient "one-pot" procedure that allows control over the end-group functionalization. The presence of the metal−polymer complex has been established by EPR and UV−vis spectroscopy.

Mixing of the Ni^{2+}−NTA polymers with the corresponding nonfunctionalized block copolymers at a concentration of 10 mol% does not affect the self-assembly behavior of the mixtures, i.e., in dilute aqueous solutions the polymer mixtures aggregate to vesicular structures (metal-doped vesicles) with identical size distribution as the nonfunctionalized block copolymer vesicles. The accessibility of the metal sites at the surface of such vesicles has been tested using fluorescence correlation spectroscopy. Our model proteins His_{10}-MBP-FITC and His_6-EGFP bind selectively to the M^{2+}−NTA groups exposed at the surface of the vesicles. While the choice of the buffer significantly influenced the fractions of protein−vesicle conjugates, the interactions of Cu^{2+}− and Ni^{2+}−NTA groups with both His-tagged proteins showed similar values. It should be noted that the experimentally determined dissociation constants of the M^{2+}-His-Tag complexes were found to be in good agreement with literature data on Ni−NTA functionalized liposomes, indicating that the polymer brushes at the polymer vesicle surface only slightly interfere with the binding of the proteins.

We believe that these metal-functionalized polymeric membranes have a large potential for the selective immobilization and alignment of proteins at vesicle/planar membrane surfaces. In particular, the high flexibility and compressibility of block copolymer membranes and monolayers could open new possibilities for inducing a 2D protein crystallization. The high cohesion and robustness of block copolymer membranes makes them rather insensitive toward mechanical shear or the presence of detergents, increasing their potential utility. In this context, it should also be noted that the pendant double bonds of the poly(butadiene) blocks can be covalently cross-linked, thus freezing in the self-assembled structures and providing additional stabilization.

Acknowledgment. Financial support was provided by the National Center of Competence in Nanoscale Science, the Swiss National Science Foundation, MRTN-CT-2004-005516 and

NEST029084. The authors thank Prof. Robert Tampé, (University of Frankfurt/Main) for providing protected NTAs and Tris−NTAs. C.P. thanks the EPR group at ETH Zurich for providing EPR facilities. The authors thank Dr. Violeta Malinova and David W. Hughes (University of Basel) for reading the manuscript.

Supporting Information Available: Synthesis of polybutadiene (PB_{39}-H) (**3**); synthesis of polybutadiene-*block*-poly(ethylene oxide) ($PB_{39}-PEO_{36}$) (**6**); intermediate/final products in the synthesis of Ni^{2+}−TrisNTA-modified polybutadiene-*block*-poly(ethylene oxide) (PB_{39}-PEO_{36}-SA-TrisNTA.d−Ni^{2+}) (**9a**, **10a**, **11a**, and **13a**); room temperature electronic spectra of PB_{60}-PEO_{34}-SA-NTA.d−Cu^{II} and PB_{60}-PEO_{34}-SA-OH, in chloroform (Figure S1-a); room temperature electronic spectra of PB_{60}-PEO_{34}-SA-NTA.d−Ni^{II} and PB_{60}-PEO_{34}-SA-OH, in chloroform (Figure S1-b); film rehydration of different diblock copolymers in bidistilled water (Table S1); FCS, protein-bound to vesicles fraction (Graph S1); light scattering, vesicles purification (Figure S2); DLS study (Figure S3). This material is available free of charge via Internet at http://pubs.acs.org.

LA8027308

D. Materials and methods

GPC. Gel permeation chromatography was performed using THF as the mobile phase at 35°C at a flow rate of 1.0 mL/min. The stationary phase was an 8×300 mm analytical column containing a PSS GRAL linear gel (particle size: 10 µm). A differential refractive index (RI) device was used as a detector. Calibration was done with pullulan standards (Polymer Standards Service, Mainz, Germany).

LS. Dynamic and static light scattering (DLS, SLS) experiments were done with a commercial goniometer (ALV) with a He:Ne laser (JDS Uniphase, wavelength λ = 632.8 nm). Scattering angles ranged from 30° to 150° and the photon intensity autocorrelation function $g_2(t)$ was determined with an ALV-5000E correlator. The experiments were performed at T = 293 ± 0.02 K. The refractive index increment dn/dC was obtained at 293 K and 632.8 nm with an ALV-DR1 differential refractometer. SLS data were analyzed via Zimm plot and DLS data by regularized CONTIN algorithm (250 grid points) and non-linear decay-time analysis.

SEM. Scanning electron microscopy was performed on a Philips XL30 FEG ESEM operated at 10 kV. Samples were sputtered with Ag or Pt prior to imaging.

TEM. Samples were dissolved in water under mild overnight stirring, deposited on carbon/parlodion-coated TEM copper grids, and allowed to dry at room temperature. Samples were stained for 30 s with 6% uranyl acetate and TEM images were taken on an FEI Morgagni 268D operated at 80 kV.

XRD. Powder X-ray diffraction patterns were measured at room temperature on a Stoe Stadi P diffractometer equipped with a curved germanium monochromator using Cu$K\alpha$ radiation.

IR spectroscopy. Infrared spectra were obtained on a Shimadzu FTIR 8300 with a Golden Gate ATR unit. Spectra were recorded from 300 to 4500 cm^{-1} with a resolution of 4 cm^{-1}.

PEO-PMOXA synthesis. Polymers were prepared by cationic ring-opening polymerization from tosyl-functionalized PEO macroinitiators (Scheme 5), as described previously.[78,112,116,139] All chemicals were obtained from Aldrich.

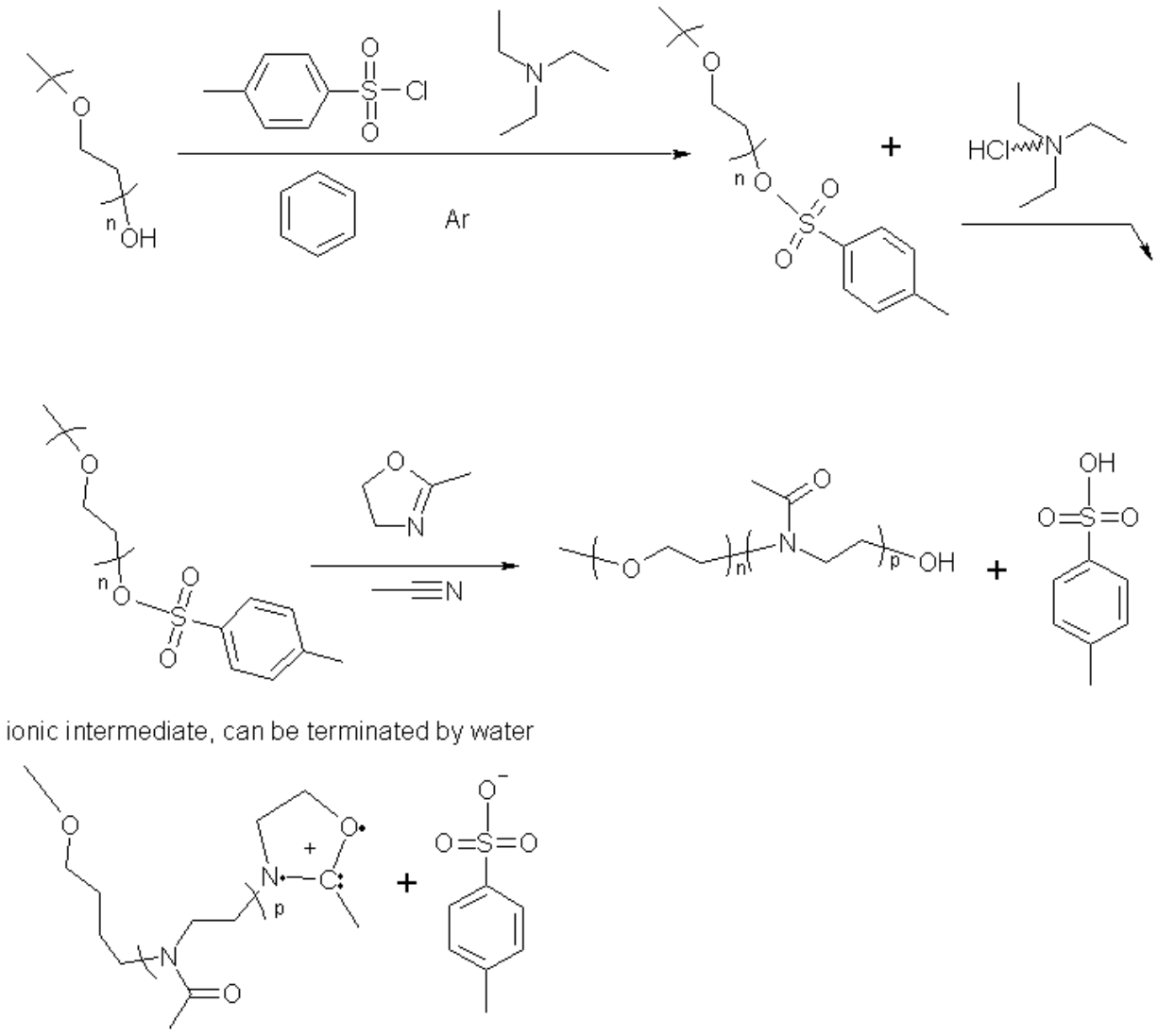

Scheme 5. Synthesis of PEO-PMOXA diblock copolymers.

Table 9. Molecular characteristics of the polymers used in the current study.

Sample	x_{MOXA} [a]	M_n [b] kg/mol	$(M_w/M_n)^{app}$ [c]	M_w^{app} [d] kg/mol
PEO_{113}-$PMOXA_{118}$	0.51	15.1	1.55	23.4
PEO_{113}-$PMOXA_{60}$	0.35	10.1	1.69	17.1

a) mole fraction of PMOXA.

b) Determined by NMR.

c) Determined by GPC.

d) $M_w^{app} = M_n \cdot (M_w/M_n)^{app}$.

NMR. All NMR experiments were performed at 25°C on a Bruker DRX-600 NMR spectrometer, equipped with a *z*-axis pulsed field gradient dual broadband inverse probe-head. Chemical shifts were referenced to residual solvent peaks and the temperature was calibrated using a methanol sample.

2D NMR – NOESY. NOESY experiments were performed with 2048 time points in F2 and 1024 time increments in the indirect dimension F1, which corresponds to acquisition times of 170 ms in F2 and 85 ms in F1. Mixing times were between 1.0 and 1.2 seconds. The total experiment time was 6 to 24 hours.

2D NMR – DOSY. Diffusion experiments were performed at 298 K and the temperature was calibrated using a methanol standard showing accuracy within ± 0.2 K. The gradient strength was calibrated using a Shigemi tube filled with H_2O to a height of 4.0 mm.[137] The resulting gradient calibration was validated by determining the diffusion coefficient of water at 298 K and reproduced the literature value within 2%. The diffusion experiments were performed by varying the gradient strength between 2% and 95% of the maximum strength in 32 single experiments while keeping the diffusion times and gradient lengths constant. The entire experiment was then repeated with a different diffusion time (100 – 500 ms). The intensity decrease of the signal of interest was determined and fitted with a Bruker *t1*/*t2* software package suitable for DOSY experiments, which is included in the XWINNMR software.[138]

Analytical ultracentrifugation. Analytical Ultracentrifugation (AUC) was performed on a Beckman-Coulter XL-I ultracentrifuge equipped with UV/Vis Absorption and Raleigh Interference optics. All experiments were carried out at 25°C in self made titanium double sector centerpieces using interference detection. Sedimentation-velocity experiments were carried out at 60K rpm, sedimentation-equilibrium experiments at 30 K – 45 K rpm on a concentration series from 0.1 – 5 g/L. Molar masses and diffusion-corrected sedimentation coefficient distributions c(s) were evaluated using the programs MSTAR[140] and SEDFIT,[141] respectively. The partial specific volume of the polymer (ρ = 0.809 mL/g) was determined with a DMA 5000 density oscillation tube (Anton Paar, Graz, Austria).

Viscosimetry. Viscosimetry experiments were done at 25°C using a thermostated Ubbelohde viscosimeter. The polymers were dissolved in water and stirred until a clear solution of 40 g/L was obtained. Dilutions were made from this stock solution using volumetric flasks. Calibration was made with poly(ethylene oxide) standards of 3, 5, 6, 35, and 600 kg/mol.

Water uptake experiments. The water uptake experiments were carried out in a desiccator at constant humidity (84%) over saturated potassium nitrate solution at 18 and 25°C. Samples were removed from the desiccator for gravimetric analyses.

Surface tension measurements. Surface tension experiments were performed on tensiometer from Data Physics DCAT 11 at 25°C using the Wilhelmy plate method.

PEO-PVL synthesis. PEO-PVL block copolymers were synthesized by living cationic polymerization as described in e.g. **[145].**

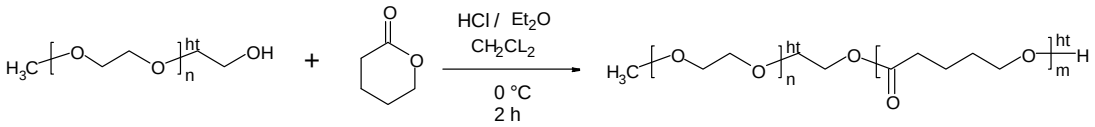

Scheme 6. Synthesis of the PEO-PVL block copolymers

Table 10 summarizes the molecular characteristics of the polymers used in this study.

Table 10. **PEO-b-PVL block copolymers used in this study.**

Polymer	MW (calc.)	MW (GPC)	PD	MW (NMR)
PEO5000-b-PVL3000	8000	6060	1.10	7000
PEO5000-b-PVL5000	10000	13400	1.34	9500

E. Table of illustrations

1. Figures

2. Tables

3. Equations

4. Schemes

VII. Acknowledgement

Prof. Wolfgang Meier and Dr. Andreas Taubert, for their guidance, advice and the freedom they gave me;

Dr. Daniel Haüssinger, for guiding me through and performing the 2D-NMR experiments;

Prof. Edwin Constable, for being my defence chairman ;

Dr. Katarzyna Kita, for her support on the Langmuir-Blodgett system and all the useful discussion;

Dr. Corinne Vebert, for introducing me to light scattering and involving her group into vivid frisbee-luncheons;

M. Düggelin and D. Mathys, for tireless support on SEM measurements;

Dr. Markus Neuburger, for his kind help with the XRD measurements;

Alexander Senti, for providing with the PEO-PVLs;

Prof. Katharina Fromm, for giving us access to her TGA apparatus;

Dr. Muhammad Chadi, for performing cryo-TEM;

Sven Kasper, for support in the lab whenever needed;

The Swiss National Science Foundation and the NCCR Nanosciences for financial support.

VIII. References

1 H. Colfen, S. Mann, *Angew. Chem. Int. Ed. Engl.* 2003, *42*, 2350.

2 S. Mann, Biomineralization: Principles and concepts in bioinorganic materials chemistry, Vol. 5, Oxford University Press, Oxford New York, 2001.

3 Long, J.R., Dindot, J.L., Zebroski, H., Kihne, S., Clark R.H., Campell, A.A., Stayton, P.S., and Drobny G.P. (1998) *Proc. Natl Acad Sci. 95*, 12083-12087.

4 H. Furedi-Milhofer, S. Sarig, *Prog. Cryst. Growth Charact.* 1996, *32*, 45.

5 H. Furedi-Milhofer, J. Moradian-Oldak, S. Weiner, A. Veis, K. P. Mintz, L. Addadi, *Conn. Tissue Res.* 1994, *30*, 551.

6 N. L. Huq, K. J. Cross, E. C. Reynolds, *J. Mol. Model.* 2000, *6*, 35.

7 E. Bauerlein, Biomineralization—Progress in Biology, Molecular Biology and Application, Wiley-VCH, Weinheim, 2004.

8 T.R. Arnett, Bone structure and bone remodeling.

9 G. Goobes, R. Goobes, O. Schueler-Furman, D. Baker, P. S. Stayton, G. P. Drobny, *Magn. Reson. Chem.* 2007; 45: S32–S47

10 S. Schweizer, A. Taubert, Macromol. Biosci. 2007, 7, 1085.

11 M. Bohner, U. Gbureck and J. E. Barralet, Biomaterials, 2005, 26, 6423.

12 M. Bohner, Injury, 2000, 31, 37.

13 I. W. Hamley, The Physics of Block Copolymers, Oxford University Press, Oxford, 1998.

14 J. M. G. Cowie and V. Arrighi, Polymers: Chemistry and Physics of Modern Materials, CRC Press, 2007.

15 G. Riess, Prog. Polym. Sci., 2003, 28, 1107.

16 S. Förster, V. Abetz and A. H. E. Mü ller, Adv. Polym. Sci., 2004, 166, 173.

17 *M. Sauer, T. Haefele, A. Graff, C. Nardin and W. Meier, Chem. Commun., 2001, 2452.*

18 *C. Nardin and W. Meier, Rev. Mol. Biotechnol., 2002, 90, 17.*

19 *A. Graff, M. Sauer, P. Van Gelder and W. Meier, Proc. Natl. Acad. Sci. U. S. A., 2002, 99, 5064.*

20 *R. Stoenescu and W. Meier, Mol. Cryst. Liq. Cryst., 2004, 417, 185.*

21 *E. G. Bellomo, M. D. Wyrsta, L. Pakstis, D. Pochan and T. J. Deming, Nat. Mater., 2004, 3, 244.*

22 H. Schlaad, H. Kukula, J. Rudloff and I. Below, Macromolecules, 2001, 34, 4302.

23 H. Kukula, H. Schlaad, M. Antonietti and S. Fo¨ rster, J. Am. Chem. Soc., 2002, 124, 1658.

24 F. Checot, S. Lecommandoux, Y. Gnanou and H. A. Klok, Angew. Chem., Int. Ed., 2002, 41, 1339.

25 B. Rippner, K. Boschkova, P. M. Claesson and T. Arnebrant, Langmuir, 2002, 18, 5213.

26 A. Wesemann, H. Ahrens, R. Steitz, S. Foerster and C. A. Helm, Langmuir, 2003, 19, 709.

27 R. B. Cheyne and M. G. Moffitt, Langmuir, 2006, 22, 8387.

28 T. J. Joncheray, K. M. Denoncourt, M. A. R. Meier, U. S. Schubert and R. S. Duran, Langmuir, 2007, 23, 2423.

29 G. L. Gaines Jr, Langmuir, 1991, 7, 834.

30 M. Oner, J. Norwig, W. H. Meyer and G. Wegner, Chem. Mater., 1998, 10, 460.

31 H. Colfen and M. Antonietti, Langmuir, 1998, 14, 582.

32 M. Sedlak, H. Cölfen, Macromol. Chem. Phys. 2001, 202, 587.

33 H. Cölfen, Macromol. Rapid. Commun. 2001, 22, 587.

34 H. Cölfen, L. Qi, Chem. Eur. J. 2000, 7, 106.

35 A. Taubert, G. Wegner, J. Mater. Chem. 2002, 12, 805.

36 K. Gorna, R. Munoz-Espi, F. Grohn, G. Wegner, Macromol. Biosci. 2007, 7, 163.

37 G. Wegner, P. Baum, M. Muller, J. Norwig, K. Landfester, *Macromol. Symp.* 2001, *175*, 349.

38 A. Taubert, C. Kübel, D. C. Martin, *J. Phys. Chem B* 2003, *107*, 2660.

39 A. Taubert, D. Palms, Ö. Weiss, M.-T. Piccini, D. N. Batchelder, *Chem. Mater.* 2002, *14*, 2594.

40 A. Taubert, D. Palms, G. Glasser, *Langmuir* 2002, *18*, 4488.

41 S.-H. Yu, H. Colfen, *J. Mater. Chem.* 2004, *14*, 2124.

42 M. Oner, J. Norwig, W. H. Meyer, G. Wegner, *Chem. Mater.* 1998, *10*, 460.

43 A. Taubert, C. Kübel, D. C. Martin, *J. Phys. Chem B* 2003, *107*, 2660.

44 A. Taubert, D. Palms, Ö. Weiss, M.-T. Piccini, D. N. Batchelder, *Chem. Mater.* 2002, *14*, 2594.

45 A. Taubert, D. Palms, G. Glasser, *Langmuir* 2002, *18*, 4488.

46 J. M. Marentette, J. Norwig, E. Stöckelmann, W. H. Meyer, G. Wegner, *Adv. Mater.* 1997, *9*, 647.

47 M. Antonietti, M. Breulmann, C. G. Göltner, H. Cölfen, K. K. W. Wong, D. Walsh, S. Mann, *Chem. Eur. J.* 1998, *4*, 2493.

48 J. V. Garcia-Ramos, P. Carmona, *J. Cryst. Growth* 1982, *57*, 336.

49 Z. Amjad, *Langmuir* 1989, *5*, 1222.

50 Y. Yokogawa, F. Nagata, M. Toriyama, K. Nishizawa, T. Kameyama, *J. Mater. Sci. Lett.* 1999, *18*, 367.

51 E. Bertoni, A. Bigi, G. Falini, S. Panzavolta, N. Roveri, *J. Mater. Chem.* 1999, *9*, 779.

52 A. Bigi, E. Boanini, G. Falini, S. Panzavolta, N. Roveri, *J. Inorg. Biochem.* 2000, *78*, 227.

53 P. A. Ngankam, P. Lavalle, J. C. Voegel, L. Szyk, G. Decher, P. Schaaf, F. J. G. Cuisinier, *J. Am. Chem. Soc.* 2000, *122*, 8998.

54 A. Bigi, E. Boanini, G. Cojazzi, G. Falini, S. Panzavolta, *Crystal Growth & Design* 2001, *1*, 239.

55 A. Bigi, E. Boanini, D. Walsh, S. Mann, *Angew. Chem. Int. Ed. Engl.* 2002, *41*, 2163.

56 Z. Amjad, R. W. Zuhl, *Phosphorus Res. Bull.* 2002, *13*, 51.

57 A. Bigi, E. Boanini, B. Bracci, G. Falini, K. Rubini, *J. Inorg. Biochem.* 2003, *95*, 291.

58 H. Imai, S. Tatara, K. Furuichi, Y. Oaki, *Chem. Commun.* 2003, 1952.

59 K. K. Perkin, J. L. Turner, K. L. Wooley, S. Mann, *Nano Lett.* 2005, *5*, 1457.

60 Z. Amjad, *Phosphorus Res. Bull.* 2005, *18*, 1.

61 V. Ball, M. Michel, F. Boulmedais, J. Hemmerle, Y. Haikel, P. Schaaf, J. C. Voegel, *Crystal Growth & Design* 2006, *6*, 327.

62 Y. Kakizawa, K. Kataoka, *Langmuir* 2002, *18*, 4539.

63 Y. Kakizawa, K. Miyata, S. Furukawa, K. Kataoka, *Adv. Mater.* 2004, *16*, 699.

64 W. Tjandra, P. Ravi, K. C. Tam, J. Yao, *Int. J. Nanosci.* 2005, *4*, 731.

65 W. Tjandra, J. Yao, P. Ravi, K. C. Tam, A. Alamsjah, *Chem. Mater.* 2005, *17*, 4865.

66 A. Taubert, C. Kübel, D. C. Martin, *J. Phys. Chem B* 2003, *107*, 2660.

67 A. Taubert, D. Palms, Ö. Weiss, M.-T. Piccini, D. N. Batchelder, *Chem. Mater.* 2002, *14*, 2594.

68 A. Taubert, D. Palms, G. Glasser, *Langmuir* 2002, *18*, 4488.

69 S.-H. Yu, H. Colfen, *J. Mater. Chem.* 2004, *14*, 2124.

70 Z. Amjad, *Phosphorus Res. Bull.* 1997, *7*, 45.

71 Z. Amjad, *Phosphorus Res. Bull.* 1999, *9*, 41.

72 A. Peytcheva, H. Cölfen, H. Schnablegger, M. Antonietti, *Coll. Polym. Sci.* 2002, *280*, 218.

73 J. Rudloff, M. Antonietti, H. Cölfen, J. Pretula, K. Kaluzynski, S. Penczek, *Macromol. Chem. Phys.* 2002, *203*, 627.

74 A. Tsortos, G. H. Nancollas, *J. Colloid Interface Sci.* 2002, *250*, 159.

75 J. Song, E. Saiz, C. R. Bertozzi, *J. Am. Chem. Soc.* 2003, *125*, 1236.

76 Z. Amjad, *Phosphorus Res. Bull.* 2005, *18*, 7.

77 J. Song, V. Malathong, C. R. Bertozzi, *J. Am. Chem. Soc.* 2005, *127*, 3366.

78 A. Sugawara, S. Yamane, K. Akiyoshi, *Macromol. Rapid. Commun.* 2006, *27*, 441.

79 S. Busch, H. Dolhaine, A. DuChesne, S. Heinz, O. Hochrein, F. Laeri, O. Podebrad, U. Vietze, T. Weiland, R. Kniep, *Eur. J. Inorg. Chem.* 1999, *10*, 1643.

80 S. Busch, U. Schwarz, R. Kniep, *Chem. Mater.* 2001, *13*, 3260.

81 S. Busch, U. Schwarz, R. Kniep, *Adv. Funct. Mater.* 2003, *13*, 189.

82 K. Gobel, P. Simon, J. Buder, H. Tlatlik, R. Kniep, *J. Mater. Chem.* 2004, *14*.

83 R. Kniep, S. Busch, *Angew. Chem. Int. Ed. Engl.* 1996, *35*, 2624.

84 M. Iijima, K. Iijima, Y. Moriwaki, Y. Kuboki, *J. Cryst. Growth* 1994, *140*, 91.

85 M. Iijima, J. Moradian-Oldak, *J. Mater. Chem.* 2004, *14*, 2189.

86 M. Iijima, Y. Moriwaki, *J. Cryst. Growth* 1989, *96*, 59.

87 M. Iijima, Y. Moriwaki, *Calcif. Tissue Int.* 1990, *47*, 237.

88 M. Iijima, Y. Moriwaki, *J. Cryst. Growth* 1991, *112*, 571.

89 M. Iijima, Y. Moriwaki, *J. Cryst. Growth* 1998, *194*, 125.

90 M. Iijima, Y. Moriwaki, Y. Kuboki, *Curr. Topics Cryst. Growth Res.* 1995, *2*, 1.

91 M. Iijima, Y. Moriwaki, Y. Kuboki, *Connective Tissue Res.* 1997, *36*, 51.

92 M. Iijima, Y. Moriwaki, Y. Kuboki, *Connective Tissue Res.* 1998, *38*, 171.

93 M. Iijima, Y. Moriwaki, R. Yamaguchi, Y. Kuboki, *Connective Tissue Res.* 1997, *36*, 73.

94 M. Iijima, H. Takita, Y. Moriwaki, Y. Kuboki, *Comparative Biochemistry and Physiology, Part A: Molecular & Integrative Physiology* 1991, *98A*, 379.

95 P. Simon, W. Carrillo-Cabrera, P. Formanek, C. Gobel, D. Geiger, R. Ramlau, H. Tlatlik, J. Buder, R. Kniep, *J. Mater. Chem.* 2004, *14*, 2218.

96 P. Simon, U. Schwarz, R. Kniep, *J. Mater. Chem.* 2005, *15*, 4992.

97 H. Tlatlik, P. Simon, A. Kawska, D. Zahn, R. Kniep, *Angew. Chem. Int. Ed.* 2006, *45*, 1905.

98 T. Iwatsubo, K. Sumaru, T. Kanamori, T. Shinbo, T. Yamaguchi, *Biomacromolecules* 2006, *7*, 95.

99 C. T. Laurencin, Y. Khan, in *Scaffolding in Tissue Engineering* (Eds.: P. X. Ma, J. Ellisseeff), CRC Taylor & Francis Group, Boca Raton-New York-Abingdon, 2006, p. 253.

100 G. Wei, P. X. Ma, in *Scaffolding In Tissue Engineering* (Eds.: P. X. Ma, J. Ellisseeff), CRC Taylor & Francis Group, Boca Raton-New York-Abingdon, 2006, p. 241.

101 X. Liu, B. Liu, Z. Wang, B. Zhang, Z. Zhang, The Journal of Physical Chemistry C 2008 112 (26), 9632-9636.

102 J. H. Fendler, Supramol. Chem., 1995, 6, 209. J. H. Fendler, Curr. Opin. Solid State Mater. Sci., 1997, 2, 365.

103 F. C. Meldrum, N. A. Kotov and J. H. Fendler, Chem. Mater., 1995, 7, 1112.

104 E. DiMasi, V. M. Patel, M. Sivakumar, M. J. Olszta, Y. P. Yang and L. B. Gower, Langmuir, 2002, 18, 8902.

105 D. Volkmer, M. Fricke, T. Huber and N. Sewald, Chem. Commun., 2004, 1872.

106 D. Volkmer, M. Harms, L. Gower and A. Ziegler, Angew. Chem., Int. Ed., 2005, 44, 639.

107 D. Volkmer, M. Fricke, C. Agena and J. Mattay, J. Mater. Chem., 2004, 14, 2249.

108 S. Cavalli, D. C. Popescu, E. E. Tellers, M. R. J. Vos, B. Pichon, M. Overhand, H. Rappaport, N. A. J. Sommerdijk and A. Kros, Angew. Chem., Int. Ed., 2006, 45, 739.

109 L.-J. Zhang, H.-G. Liu, X.-S. Feng, R.-J. Zhang, L. Zhang, Y.-D. Mu, J.-C. Hao, D.-J. Qian and Y.-F. Lou, Langmuir, 2004, 20, 2243.

110 E. D. Spoerke, S. I. Stupp, *Biomaterials* 2005, *26*, 5120.

111 M. Michel, Y. Arntz, G. Fleith, J. Toquant, Y. Haikel, J.-C. Voegel, P. Schaaf and V. Ball, Langmuir, 2006, 22, 2358.

112 A. Taubert, E. Furrer, W. Meier, *Chem. Commun.* 2004, 2170.

113 *Calcium Phosphates in Biological and Industrial Systems, Kluwer Academic Publishers, Norwell-Dordrecht, 1998.*

114 S. Mann, J. Webb and R. J. P. Williams, Biomineralization: Chemical and Biochemical Perspectives, VCH Publishers, Weinheim, 1989.

115 E. Bauerlein, Biomineralization—Progress in Biology, Molecular Biology and Application, Wiley-VCH, Weinheim, 2004.

116 A. Thunemann, S. General, Macromolecules 2001, 34, 6978.

117 I. Ikeda, N. Hiorie, K. Suzuki, *J. Appl. Polym. Sci.* 1994, *54*, 1123.

118 X. Lou, C. Detrembleur, R. Jerome, *Macromolecules* 2002, *35*, 1190.

119 M. S. Kim, K. S. Seo, G. Khang, S. H. Cho, H. B. Lee, *J. Polym. Sci. A: Polym. Chem.* 2004, *42*, 5784.

120 B. Parrish, T. Emrick, *Macromolecules* 2004, *37*, 5863.

121 J. Yang, L. Jia, L. Yin, J. Yu, Z. Shi, Q. Fang, A. Cao, *Macromol. Biosci.* 2004, *4*, 1092.

122 B. Parrish, R. B. Breitenkamp, T. Emrick, *J. Am. Chem. Soc.* 2005, *127*, 7404.

123 F. Zeng, H. Lee, M. Chidiac, C. Allen, *Biomacromolecules* 2005, *6*, 2140.

124 F. Zeng, H. Lee, C. Allen, *Bioconjugate Chem.* 2006, *17*, 399.

125 W.-J. Lin, C.-L. Wang, L.-W. Juang, *J. Appl. Polym. Sci.* 2006, *100*, 1836.

126 O. Colombani, M. Ruppel, M. Burkhardt, M. Drechsler, M. Schumacher, M. Gradzielski, R. Schweins and A. H. E. Mueller, Macromolecules, 2007, 30, 4351.

127 O. Colombani, M. Ruppel, F. Schubert, H. Zettl, D. V. Pergushov and A. H. E. Mueller, Macromolecules, 2007, 40, 4338.

128 E. Eghbali, O. Colombani, M. Drechsler, A. H. E. Mueller and H. Hoffmann, Langmuir, 2006, 22, 4766.

129 B.Brissault, Eur. Polym. J. 38 (2002), 219-228.

130 W. Burchard, G. D. Patterson, Light Scattering from Polymers, Vol. 48, Springer, Berlin, 1983.

131 B. H. Zimm, J. Chem. Phys. 1948, 16, 1093.

132 B. H. Zimm, J. Chem. Phys. 1948, 16, 1099.

133 P. J. Wyatt, Anal. Chim. Acta 1993, 272, 1.

134 Shun-Cheng Wang, Chieh-Kuang Wang, Feng-Ming Chang, and, Heng-Kwong Tsao, *Macromolecules* 2002 *35* (25), 9551-9555.

135 J. Cai, R. Cheng, S. Bo, Polymer, Volume 46, 23, 2005, 10457-10465

136 J.Bandrup, E.H.Immergut, eds. Polymer Handbook, 3d ed. Wiiley-Interscience, New-York, 1989.

137 M. Holz, H. Weingärtner, J. Magn. Reson. 1991, 92, 115.

138, Bruker Biospin GmbH, Software Dept., Rheinstetten, Germany.

139 R. Stoenescu, W. Meier, Mol. Cryst. Liq. Cryst. 2004, 417, 185.

140 H. Cölfen, S. E. Harding, Eur. Biophys. J. Biophys. Lett. 1997, 25, 333.

141 P. Schuck, Biophys. J. 2000, 78, 1606.

142 A. Taubert, C. Palivan, O. Casse, F. Gozzo, B. Schmitt, The Journal of Physical Chemistry C 2007 111 (11), 4077-4082.

143 F. Axthelm, O. Casse, W. H. Koppenol, T. Nauser, W. Meier, C. G. Palivan *The Journal of Physical Chemistry B* 2008 *112* (28), 8211-8217.

144 R. Nehring, C. G. P., O. Casse, P. Tanner, J. Tüxen, W. Meier, *Langmuir* 2009 *25* (2), 1122-1130.

145 L. Helen, Z. Faquan, D. Mike, A. Christine, Biomacromolecules (2005), 6(6), 3119-3128.